CERN/LHCC/93-16
LHCC/I 4
1 March 1993

Letter of Intent

for

A Large Ion Collider Experiment

CERN/LHCC/93-16
LHCC/I 4
1 March 1993

Letter of Intent
for
A Large Ion Collider Experiment
at the
CERN Large Hadron Collider

ABSTRACT

The ALICE Collaboration proposes to build a dedicated heavy-ion detector to exploit the unique physics potential of nucleus–nucleus interactions at LHC energies. Our aim is to study the physics of strongly interacting matter at extreme energy densities, where the formation of a new phase of matter, the quark–gluon plasma, is expected. The existence of such a phase and its properties are a key issue in QCD for the understanding of confinement and of chiral-symmetry restoration. For this purpose, we intend to carry out a comprehensive study of hadrons, electrons and photons produced in the collision of heavy nuclei.

ALICE has emerged as a common design by the heavy-ion community presently engaged in the CERN heavy-ion programme, and a number of groups new to this field from both nuclear and high-energy physics. The central part of the proposed detector, which covers $(90 \pm 45)^\circ$ ($|\eta| < 0.9$) over the full azimuth, is embedded in a large magnet with a weak solenoidal field. The baseline design consists (from inside out) of a high-resolution inner tracking system, a cylindrical TPC, a particle identification array (TOF or RICH detectors), and a single-arm electromagnetic calorimeter. We will trigger on central collisions with a Zero Degree Calorimeter and measure multiplicity distributions over a large fraction of the available phase space.

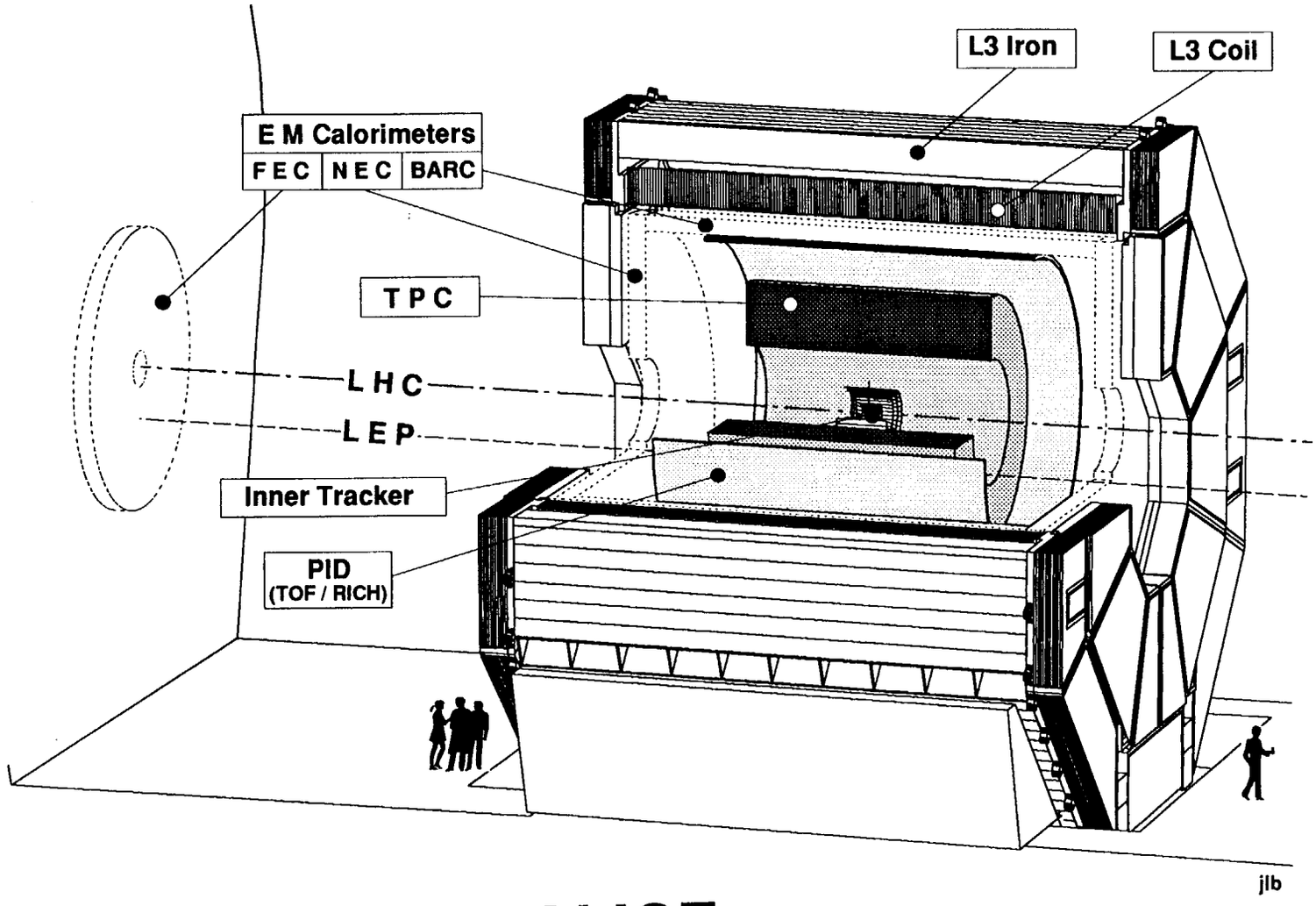
L3 Iron
L3 Coil
E M Calorimeters
F E C
N E C
BARC
T P C
L H C
L E P
Inner Tracker
PID
(TOF / RICH)
jlb

ALICE

Members of the ALICE Collaboration

Athens, Greece, Nuclear and Particle Physics Division, University of Athens:
N. Antoniou, G. Daskalakis and A.D. Panagiotou.

Bari, Italy, Dipartimento di Elettronica ed Elettrotecnica del Politecnico and Sezione INFN:
F. Corsi, C. Marzocca and G. Portacci.

Bari, Italy, Dipartimento di Fisica dell'Università and Sezione INFN:
D. Di Bari, A. Di Mauro, B. Ghidini, A. Jachołkowski, V. Manzari, E. Nappi, F. Navach and T. Scognetti.

Beijing, China, China Institute of Atomic Energy:
X. Bai, K. Jing, X. Liu, Z. Liu, Y. Mao, B. Sa, Z. Sun, Y. Wan, Z. Wang, J. Xu, X. Zhang, Y. Zheng and S. Zhou.

Bergen, Norway, Department of Physics, University of Bergen:
E. Andersen, H. Helstrup, A.K. Holme, G. Lovhoiden and T.F. Thorsteinsen.

Birmingham, United Kingdom, School of Physics and Space Research,
University of Birmingham:
I.J. Bloodworth, J.N. Carney, P. Jovanovich, J.B. Kinson, O. Villalobos Baillie and M.F. Votruba.

Calcutta, India, Variable Energy Cyclotron Centre:
S. Chattopadhyay, G.S.N. Murthy, B. Sinha and Y.P. Viyogi.

Catania, Italy, Dipartimento di Fisica dell'Università and Sezione INFN:
S. Albergo, Z. Caccia, P. Castorina, S. Costa, G. Immé, A. Insolia, L. Lo Monaco,
R. Potenza, G. Raciti, J. Romanski, G.V. Russo and C. Tuvé.

CERN, European Organization for Nuclear Research:
F. Antinori, D. Evans, F. Piuz, E. Quercigh, J. Schukraft and P. Sonderegger.

Cracow, Poland, High Energy Department, Institute of Nuclear Physics:
J. Bartke, E. Gładysz, M. Kowalski and P. Stefański.

Darmstadt, Germany, GSI:
R. Bock, R. Brockmann, H. Gutbrod, B. Kolb, A. Sandoval and H.R. Schmidt.

Dubna, Russia, Joint Institute for Nuclear Research:
V. Arefiev , G. Agakishiev, V. Astakhov, A. Baldin, B. Batyunya, Z. Borisovskaya, O. Gavrishchuk, B. Guskov, I. Kosarev, A. Maksimov, A. Malakhov, P. Nomokonov , Y. Panebrattsev, A. Senner, I. Shelaev, Y. Shishov, S. Shimansky, N. Slavin, A. Vodopianov and Y. Zanevsky.

Frankfurt, Germany, Institut fur Kernphysik der Universität:
D. Ferenc[1], M. Gaździcki, R. Renfordt, D. Röhrich, R. Stock, H. Ströbele and S. Wenig.

Geneva, Switzerland, Universitè de Geneve:
A. Angelis, M. Izycki, M. Martin and L. Rosselet.

Heidelberg, Germany, Max Plank Institut:
P. Wurm.

[1] also from Zagreb

Heidelberg, Germany, Physikalisches Institut, University of Heidelberg:
A. Drees and P. Glassel.

Košice, Slovakia, Institute of Experimental Physics and P.J. Šafárik University:
B. Pastirčák, J. Urbán and S. Vokál

Legnaro, Italy, Laboratori Nazionali:
R.A. Ricci.

Lund, Sweden, Division of Cosmic and Subatomic Physics, University of Lund:
S. Garpman, H.-A. Gustafsson, A. Oskarsson, I. Otterlund, K. Soderstrom and E. Stenlund.

Marburg, Germany, Fachbereich Physik der Universität:
A. Piper and F. Pühlhofer.

Minsk, Bielorussia, Institute for Nuclear Problems:
V.G. Baryshevsky, M.V. Korzhik and A.A. Fyodorov.

Messina, Italy, Dipartimento di Fisica dell'Università:
A. D'Arrigo, G. Giardina, M. Herman and A. Taccone

Moscow, Russia, Institute for Nuclear Research:
A.A. Baldin, S.N. Filippov, Yu.K. Gavrilov, A.B. Kurepin, V. Laptev, V. Matveev and
A.Yu. Nikitskiy.

Moscow, Russia, Institute for Theoretical and Experimental Physics:
V. Akimov, S.V. Boyarinov, J.G. Grishuk, S.M. Kiselev, Yu.T. Kiselev, S.V. Kuleshov,
A.N. Martemianov, K.R. Mikhailov, N.A. Pivnyuk, P.A. Polozov, S.A. Pozdnyakov, V.S. Serov,
A.V. Smirnitsky, V.P. Surin, L.S. Vorobyov and B.V. Zagreev.

Moscow, Russia, Kurchatov Institut:
S. Fokin, M. Ippolitov, A. Lebedev, V. Manko, O. Patarakin and R. Stcherbachev.

Münster, Germany, Institut fuer Kernphysik, Westfälische Wilhelms Universität
K.-H. Kampert, T. Peitzmann and R. Santo.

Novosibirsk, Russia, Budker Institute of Nuclear Physics:
Y. Pestov

Oak Ridge, U.S.A., Oak Ridge National Laboratory:
F. Plasil.

Orsay, France, Institut de Physique Nucléaire:
D. Jouan.

Padua, Italy, Dipartimento di Fisica dell'Università and Sezione INFN:
M. Morando and G. Segato.

Paris, France, Collège de France :
M. Benayoun, Ph. Leruste, J.-L. Narjoux and K. Šafařík

Prague, Czech Republic, Physics Institute and Charles University:
J. Dolejší and P. Závada.

Protvino, Russia, Institute for High Energy Physics:
V. Katchanov, V. Polyakov, Yu. Prokoshkin, S. Sadovsky, A. Shtannikov and A. Singovsky.

Rehovot, Israel, Weizmann Institute of Science:
I. Ravinovich and I. Tserruya.

Řež u Prahy, Czech Republic, Nuclear Physics Institute:
A. Kugler, L. Nosek, M. Pachr, M. Šumbera, P. Tlustý and V. Wagner.

Rome, Italy, Dipartimento di Fisica dell'Università "La Sapienza" and Sezione INFN:
H. Beker, S. Di Liberto, M.A. Mazzoni, F. Meddi and G. Rosa.

St Petersburg, Russia, University of St Petersburg and Meson Association:
V.A. Andrianov , M.A. Braun , P. Danilov , G.A. Feofilov , A.A. Kolozvary, V. Semenov, T.A. Tulina, F.F. Valiev, V.V. Vechernin, L.I. Vinogradov and M.I. Yudkin.

Utrecht, The Netherlands, NIKHEF and Subatomic Physics Department of the Utrecht University:
E. Agterhuis, J. Blom, A. van den Brink, N. van Eijndhoven, A. de Haas, R. Kamermans, P. Kuijer, C. de Laat, W. Lourens, A. Taal and M. Voerman.

Turin, Italy, Dipartimento di Fisica Sperimentale dell'Università and Sezione INFN:
E. Chiavassa, G. Dellacasa, M. Gallio, P. Giubellino, P. Guaita, A. Marzari-Chiesa, M. Masera, M. Monteno, A. Musso, L. Ramello[2] L. Riccati, E. Scomparin and E. Vercellin.

Warsaw, Poland, Institute for Nuclear Studies:
A. Bakłarz, T. Siemarczuk and G. Stefanek.

Wuhan, China, Institute of Particle Physics, Huazhong Normal University:
L. Feng, L. Lianshou and C. Xu.

Zagreb, Croatia, Rudjer Boskovic Institute:
D. Jadrijević, A. Ljubičić Jr, G. Paić and D. Vranić.

Spokesperson: **J. Schukraft,** E-mail=SKS@CERNVM.CERN.CH
Deputy: **H. Gutbrod,** E-mail=GUTBROD@VXWA80.CERN.CH

Acknowledgements

It is a pleasure to acknowledge the important contributions given by G. Baur, J. Bohm, W. Dąbrowski, V. Eckardt, Ph. Farthouat, H.G. Fisher, W. Flegel, L. Leistam, S. Mironov, G. Rai, A. Samarin, P. Seyboth, A. Shabunov, G.R. Stevenson, W. Richter, W. von Rueden, H. Satz, A. Vacchi, F. Wittgenstein and W. Witzeling to the preparation of this Letter of Intent.

We also thank S. Leech O'Neale and M. Rabbinowitz for their professional help and suggestions for the editing, and R. Audria, I. Canon and B. Dockhorn for their valuable contribution to the final typing.

[2]also Politecnico di Milano

Contents

1 - Introduction and Overview

2 - Detector Sub-systems

3 - Trigger and Data Acquisition

4 - Physics Performance

5 - Implementation

1 Introduction and Overview

The aim of high-energy heavy-ion physics is the study of strongly interacting matter at extreme energy densities (QCD thermodynamics).

Statistical QCD predicts that, at sufficiently high density, there will be a transition from hadronic matter to a plasma of deconfined quarks and gluons — a transition which in the early universe took place in the inverse direction some 10^{-5} s after the Big Bang and which might play a role still today in the core of collapsing neutron stars (see, for example, Refs. [1, 2]). The study of the phase diagram of nuclear matter, utilizing methods and concepts from both nuclear and high-energy physics, constitutes a new and interdisciplinary approach in investigating matter and its interactions. It is of interest to explore and test QCD on its natural scale (Λ_{QCD}) and to address the fundamental questions of confinement and chiral-symmetry breaking. Moreover, it is of general relevance in understanding the dynamical nature of phase transitions involving elementary quantum fields, as the QCD phase transition is the only one accessible to laboratory experiments.

The present exploratory programme with light ions at CERN and Brookhaven has established the feasibility of high-energy ion–ion experiments with their abundant particle production. It has shown that high energy densities can indeed be obtained in these reactions and produced first hints for the onset of new, collective phenomena [1]. The upcoming experiments with really heavy ions, both at BNL and CERN, should determine to what extent we can actually get into a regime of thermodynamic behaviour. They should lead to baryon densities close to or even exceeding the ones in the core of neutron stars, and — if present estimates are correct — should have a chance to obtain more conclusive evidence for quark deconfinement.

The LHC, at a center-of-mass energy of 6.1 TeV/nucleon [3], will bring us into the true high-energy heavy-ion regime; it is the only machine which will reach and even extend the energy range probed by cosmic ray nucleus–nucleus collisions. Extrapolating from present results, all parameters relevant to the formation of the Quark–Gluon Plasma (QGP) will be more favourable: the energy density, the size and lifetime of the system, and the relaxation times should all improve by a large factor, typically by an order of magnitude, compared to Pb collisions at the SPS [4, 5]. We should now get *average* energy densities well above the deconfinement threshold, and probe the QGP in its asymptotically free 'ideal gas' form. Unlike at lower energies, the central rapidity region will have nearly vanishing baryon number density, similar to the state of the early universe. It is possibly dominated in the early pre-equilibrium stage by a very dense system of semi-hard partons ('mini-jets'), which would lead to rapid thermalization and even higher initial temperatures than in the conventional scenario.

Heavy-ion collisions at the LHC are therefore expected to provide a very different, and significantly better, environment for the study of strongly interacting matter than existing accelerators.

We wish to explore this physics potential by searching in a comprehensive way for qualitative and quantitative changes in composition and structure of the final states as a function of energy density.

The heavy-ion community at CERN has explored a number of strategies towards an experimental programme [6, 7, 8]. The dedicated pp detectors at the LHC are optimized for physics differing by several orders of magnitude in event rate, multiplicity and p_t. Consequently, in heavy-ion physics they aim at a small subset of high-mass, high-p_t phenomena, in particular high-mass dimuons (Υ production) [9, 10]. Even allowing for substantial upgrades, the use of an existing LEP detector such as DELPHI was found to be impossible given the constraint of alternative operation both at LEP (e^+e^-) and LHC (heavy ions). However, reusing major parts of the L3 detector to build a specialized heavy-ion experiment seems feasible and indeed very attractive; it will be discussed further below.

The ALICE Collaboration therefore proposes to build a dedicated, general-purpose detector which will be operational at the start-up of the LHC. Its design is based on the experience gained with the existing programmes at CERN and BNL, and on several workshops on heavy-ion colliders [2, 11]. It will address a majority of the known sensitive observables including hadrons, di-leptons, and photons. It has to measure the flavour content and phase-space distribution event by event for a large number of particles whose momenta and masses are of the order of the typical energy scale involved (temperature $\approx \Lambda_{QCD} \approx 200$ MeV). The experiment will be designed to cope with the highest particle multiplicities anticipated ($dN_{ch}/dy = 8000$) for Pb-Pb reactions. Collisions of lower mass ions are a means of varying the energy density [12]. Running with protons is foreseen as part of the experimental programme to provide reference data.

In addition to the main physics programme, we are investigating the potential of this detector for the study of a number of large cross-section processes not accessible to the dedicated pp experiments, and its

use to exploit the large flux of high-energy photons associated with the strong electromagnetic fields of the colliding ions (e.g. non-perturbative QED lepton-pair production, photon–photon collisions).

1.1 Signals and Observables

In order to establish and analyse the existence of QCD bulk matter and the QGP, a number of observables have to be studied in a systematic and comprehensive way [13]. Some observables are needed to characterize the global features of the state created during the collision in order to constrain theoretical models (e.g. relevant degrees of freedom, size, lifetime, density, dynamical evolution). These observables yield information about the initial conditions and space–time evolution, necessary in order to interpret a specific signal as a QGP signature, or as an indication of new physics. Our strategy is to study a number of these *specific signals* in the same experiment together with *global information* about the events. The signals accessible to our detector are described in detail in the following sections. They are listed below according to the aspect of the collision on which they have a bearing (see [1, 2, 11, 14] for original references):

- INITIAL CONDITIONS: *global event features* measure the number of colliding nucleons and give information on the energy density obtained.

- QUARK-GLUON PLASMA: *prompt photons* can reveal the characteristic thermal radiation from the plasma; the cross-section of *high-p_t hadrons* is sensitive to the energy loss of the partons in the plasma; *J/Ψ production* probes deconfinement.

- PHASE TRANSITION: *Strangeness production* is sensitive to the large s quark density expected from (partial) chiral symmetry restoration in the plasma; *multiplicity fluctuations* are a signature for the critical phenomena at the onset of a phase transition; *particle interferometry* measures the expansion time in the mixed phase, which is expected to be long in the case of a first-order phase transition.

- HADRONIC MATTER: *Particle ratios, transverse-momentum distributions* and *resonance line-shape parameters* are all sensitive to the dynamical evolution of the hadronic phase; *interferometry* allows the measurement of the freeze-out radius of the hadronic fireball.

1.1.1 Global Event Features

Global event features (particle and transverse-energy flow) are primarily a means to determine and trigger on the geometry of nuclear reactions, i.e. impact parameter, overlap volume, and number of constituents (nucleons, quarks) participating in the interaction. In addition, they indirectly reflect some of the underlying dynamics in nuclear collisions (nuclear stopping, primary particle production mechanism, rescattering), and specify the initial conditions (e.g. energy and entropy density). The observable most directly related to the *collision geometry* is the energy carried away by the non-interacting beam nucleons (spectators), which will be measured in a forward zero-degree calorimeter (see 4.6). The shape of the *pseudorapidity distribution* $\mathrm{d}N/\mathrm{d}\eta$ will distinguish different longitudinal expansion scenarios. *Structures* in rapidity or azimuth, caused, for example, by non-statistical fluctuations or collective phenomena, will be investigated event by event with a large acceptance multiplicity detector ($|\eta| < 5$) (see 4.6).

1.1.2 Transverse Momentum Spectra

The transverse-momentum spectra can be divided roughly into three distinct regions — low (< 0.2 GeV/c), intermediate (0.2–2 GeV/c), and high (> 2 *GeV*/c) — where different processes are expected to be relevant.

a) Low Momentum Region

By the uncertainty principle, collective effects which occur over distances (or times) of 1–10 fm are associated in general with small momenta (200–20 MeV/c). One particular example is an excess of low-p_t pions produced coherently in the decay of a disoriented chiral condensate or a classical pion field. All these pions would have similar soft momenta and non-statistical fluctuations in the charged-to-neutral ratio. A modification of the pion dispersion relation in matter (quasi-pions) or a non-zero chemical potential (pion condensate) would lead to an enhancement of all pion species at low p_t. In order to have access to physics at *long distance scales*, the inner tracking system has a stand-alone capability as a spectrometer with momentum measurement and particle identification for soft particles ($p_t < 120$ MeV/c) which do not reach the outer layers (see 4.1, 4.2).

b) Intermediate Momentum Region

The intermediate momentum region, which includes the majority of all produced particles, will give information on the nature and dynamical evolution of the system. With up to 12,000 charged par-

ticles in the central rapidity acceptance, the *shape of the p_t distribution* can be measured for pions, kaons ($\approx$ 2000), and even protons (several hundred) on a single-event basis (see 4.2). The *average* p_t will be measured with high accuracy ($\approx$ 1% for pions) and therefore individual events can be assigned a 'temperature' per particle type which can be correlated with other observables. Thermodynamical instabilities during the phase transition resulting in 'explosive' deflagration of the matter could lead to large event-by-event *fluctuations and extremely high temperatures*. Inclusive, high-statistics measurements of different particle types will allow the investigation of *expansion dynamics* and *collective flow phenomena*.

c) High Momentum Region

The propagation of high-p_t partons arising from an initial-state hard scattering is sensitive to the properties of the surrounding medium. In particular, the *energy loss of fast quarks and gluons* could be different in a dense hadronic system and a QGP (*'jet quenching'*). Experimentally, jets in nuclear collisions at the LHC cannot be well measured for p_t below 20–50 GeV/c because of statistical fluctuations in the soft energy of the underlying event. However, hadrons at high p_t provide an alternative means to measure this effect. Similarly to the jets themselves, single-particle spectra at high p_t ($>$ 2–5 GeV/c), reflect the energy loss of partons (before fragmentation) and this results in striking differences in the shape of the spectra predicted for nucleus–nucleus and pp collisions.

1.1.3 Flavour Composition

The abundance of particle species (hadrons/quarks) in chemical equilibrium is determined completely by a few thermodynamical quantities, i.e. temperature, mass, and chemical potential. The presence of (at least partial and local) equilibrium is crucial if we want to describe heavy-ion collisions in terms of QCD thermodynamics. Therefore this has to be verified by measuring the densities of a sufficient number of different particle species. Strange quarks are of particular importance because their production is favoured in a QGP, since their mass will be reduced from the constituent ($\approx$ 500 MeV) to the current value ($\approx$ 150 MeV) (partial chiral symmetry restoration). During the dynamical evolution, the particle composition will change, but each particle species provides a unique 'clock' which characterizes the system on a different time scale. Reactions with large cross-sections at thermal energies (small relaxation times), such as K production, will stay in equilibrium until freeze-out. Heavier particles, in particular Ξ and Ω, are difficult to produce in thermal collisions (long relaxation time) and their abundance might not change significantly during the short lifetime of the hadron gas ($<$ 10 fm/c). Multi-strange hyperons are therefore potentially very good signatures for the large strangeness density expected in the QGP. Their detection requires a vertex detector close to the beam pipe.

We will measure simultaneously a large number of stable particles and resonances (π, η, ω, ϕ, p, K, Λ, Ξ, Ω) as a function of charged-particle density and p_t (see chapter 4). This will allow us to test the *thermalization*, constrain *dynamical evolution scenarios*, and should also yield information about the *phase transition* itself. Some particle ratios can be accurately measured on an event-by-event basis to look for fluctuations or to correlate them with other observables.

A direct measurement of open charm would be of great interest. An enhanced charm production has been predicted at the extremely dense systems created at the LHC. The capability of identifying secondary vertices from charm decays is currently being investigated.

1.1.4 Correlations and Fluctuations

One of the unique features of heavy-ion collisions at the LHC is the possibility to measure a large number of observables on an *event-by-event* basis: impact parameter (via ZDC), dN/dy, $\pi, \gamma, K, p, \Lambda$ ratios and p_t spectra, and, of particular importance, size and lifetime from interferometry. To make full use of this opportunity is one of the important design considerations for our detector, because it will allow the study of correlations and non-statistical fluctuations which would be washed out when averaging over many events. Such fluctuations are, in general, associated with *critical phenomena* in the vicinity of a phase transition, and lead to local or global differences in the events, even for similar initial conditions.

Structures in dN/dη, which can be measured over $\approx$ 10 units of rapidity in our detector, have been predicted to arise from the hadronization of the QGP (see 4.6). *Multiparticle correlations* are a sensitive tool to study correlations over many length scales and will be done in three dimensions (p_t, y, ϕ) in the central region [15]. A large imbalance between hadronic and electromagnetic energy, as observed in the still unexplained CENTAURO events in cosmic-ray exposures, will be observable, if present at midrapidity, by the single-arm e.m. calorimeter.

Bose–Einstein correlations between identical particles should give access to the space-time history of the particle-emitting source. High-statistics data will be available at the LHC to do a differential Hanbury-

Brown and Twiss (HBT) analysis (R_l, R_{tside}, R_{tout}, see 4.3) as a function of dN/dy and p_t. The correlation for a number of particle types can be investigated ($\pi^{\pm}, K^{\pm}, p, \bar{p}$ and possibly K^0_s), which will yield different radii if they freeze out at different times. This comprehensive analysis will provide detailed information on the *freeze-out geometry*, the *expansion dynamics* in the hadronic phase, and possibly the existence and nature of the *phase transition*. In particular, if the transition is of first order, the long lifetime in the mixed phase will lead to large values of R_l.

The large radii of the order of 20 fm and the long lifetimes ($\geq$ 10 fm/c) expected at the LHC pose severe requirements on the detector in terms of momentum and two-track resolution. We will be able to measure on an event-by-event basis radii up to 15 fm, and inclusively up to 30–40 fm (see 4.3).

No primary nuclear fragments are expected at midrapidity at the LHC. Anti-deuterons and heavier nuclei result from the *coalescence* of baryons; their abundance is governed by density and lifetime of the hadronic phase. The d/p ratio will therefore give information complementary to the HBT analysis.

1.1.5 Prompt Photons

Electromagnetic probes are a unique tool to study the early and hot phases of nuclear collisions, because the produced photons and lepton pairs escape from the finite system without re-interaction. The *thermal radiation* from the QGP and mixed phase could be observable in the medium-p_t range (around 1–3 GeV/c). Direct photons from the *pre-equilibrium* phase (3–6 GeV/c) contain information on the parton dynamics at very early stages, about equilibration times, and about the transition from perturbative to non-perturbative phenomena. At still higher momenta, direct photons originate mainly from *initial hard processes* and can be used to extract structure functions in nuclei (together with the Drell–Yan process).

Because of the large background arising from hadronic decays (mainly π^0 and η), a precise measurement of the rates and p_t spectra of these mesons is vital in order to extract the prompt photon component. The predicted signal of thermal photons is of the order of a few to a few ten per cent of the total inclusive photon yield, depending on initial conditions and the shape of the meson p_t spectra. It will, in general, be more favourable at high initial-energy density and might indeed only be observable at the large densities predicted for LHC. We aim at a sensitivity, limited by systematic errors, of $\approx$ 5% for the measurement of prompt photons in the energy range 1–10 GeV (see 4.5).

1.1.6 Lepton Pairs

The physics interest in continuum lepton pairs is identical to the one mentioned above for photons, i.e. thermal radiation at small masses, pre-equilibrium and hard processes (Drell–Yan) at high masses. In addition, the *vector mesons* ($\rho, \omega, \phi, J/\Psi, \Upsilon$) can be observed in their leptonic decay modes. The lighter mesons, with lifetimes of the order of the expansion time scale, will partially decay during the evolution of the system. Their properties (mass, width, branching ratios), observable in the leptonic decay, should *change in dense matter* owing, for example, to 'collision broadening', 'induced radiation' and other in-medium effects. In the vicinity of the phase transition, partial restoration of chiral symmetry will lead to additional shifts of the mass. The ϕ meson, only 30 MeV above the KK threshold, is expected to be extremely sensitive. A few MeV shift of the in-medium kaon mass would drastically alter the relative branching fractions of $\phi \rightarrow$ KK and $\phi \rightarrow$ ee. The width of the ω might reach 50–60 MeV, i.e. more then five times the normal value. The magnitude and even the sign of these effects are difficult to predict by current theories (mainly chiral perturbation theory), but experimentally unambiguous if a change of *resonance line shapes* should be observed.

The *suppression of heavy quarkonium resonances* via Debye screening is an important tool to diagnose the early stages of the QGP. A full 'spectral analysis' of the J/Ψ and Υ families as a function of energy density and transverse momentum should distinguish QGP from hadronic suppression scenarios.

Because of the large combinatorial physics background from Dalitz decays, continuum lepton pairs will not be easily accessible at high multiplicities. However, we will measure ω and ϕ production via their e^+e^- decays with a mass resolution of $\Delta m/m \approx$ 1% (see 4.4). The rates will also be sufficient to measure inclusive J/Ψ production at low p_t. At higher momenta, J/Ψ's are dominantly originating from b decays far outside the plasma region.

1.1.7 Non-QGP Physics: $\gamma\gamma$ Collisions

The large flux of virtual photons associated with the Coulomb fields of coherently interacting Pb nuclei will lead to γ–γ luminosities which exceed by orders of magnitude those achieved at present or future e^+e^- colliders [16, 17]. The physics interest in $\gamma\gamma$ collisions includes a large number of QED and QCD processes, from lepton pairs to hadrons, hadron pairs and jet pairs [18]. Whilst the production of high-mass objects such as a light Higgs ($m \approx$ 100 GeV) is out of reach, even a short run of 10^6 s will produce co-

pious amounts of mesons in the mass range below a few tens of GeV/c^2 (e.g. a hundred $\eta_b(9366)$, the yet undiscovered pseudoscalar bottonium, and half a million $\eta_c(2981)$) [17, 19].

The two-photon process, being a probe of the quark content of the final state, is of particular interest for meson spectroscopy. Among the 'exotic' states predicted in this mass range are *hybrid mesons* ($q\bar{q}g$) which contain one valence gluon; *multiquark mesons* ($qq\bar{q}\bar{q}$), predicted by the MIT model, with first candidates found in $\gamma\gamma$ reactions [20]; and *high spin states*, produced preferentially in $J = 2\,\gamma\gamma$ collisions. *Glueballs* are a fundamental and unresolved QCD issue. Their constituents are all neutral, and hence do not directly couple to photons. Their near absence in $\gamma\gamma$ interactions provides therefore a decisive test. It requires, however, a much higher luminosity than available at e^+e^- colliders [20]; the LHC with Pb beams will be adequate.

A heavy-ion experiment, equipped with charged-particle and photon detectors may well provide a very attractive tool for photon–photon collisions. While we clearly recognize this possibility, we feel that before integrating $\gamma\gamma$ collisions into the present project, further studies should be carried out in areas of concern such as the trigger veto against peripheral hadronic interactions, a positive trigger for low invariant mass, and the integration into the present detector.

1.2 Design Considerations

The following list summarizes the main design criteria for the dedicated heavy-ion detector. The individual points will be addressed in more detail in the subsequent sections.

- VERSATILITY: Instead of selecting particular signals which might look most promising today, we will search in an unbiased way for qualitative and quantitative changes in a number of final states (hadrons, electrons, photons).
- ACCEPTANCE: The detector will concentrate on physics at mid-rapidity, i.e. on the regions of minimum baryon and maximum energy density, which are the unique features of LHC compared to the lower energy machines RHIC and SPS.
- ROBUSTNESS: One single dedicated heavy-ion detector is foreseen at the initial stage at LHC. Its design has to be conservative and robust.
- FLEXIBILITY: An open geometry will ease future modifications and upgrades if first physics results should suggest focusing on specific signals, selective triggers, or larger acceptance.

1.2.1 Experimental Conditions

The average event rate for Pb–Pb collisions at the LHC will only be about 2000–4000 minimum-bias collisions per second (see 3.1). Of these, approximately 2–3% (< 100 events/s) correspond to the most interesting central collisions with maximum particle production. The low interaction rates lead naturally to an approach which combines large geometrical acceptance with simple central collision triggers and a high data-taking rate.

These rates are matched with the dead-time of our slowest detector and the capabilities of our DAQ system (see chapter 3). A large collected sample of central collisions will allow an unbiased search for signals including 'surprises' not predicted by current theories, a feature of particular importance in the rapidly evolving field of relativistic heavy-ion physics. In the initial phase, running times comparable with the ones for the present SPS ion programme will be adequate to collect sufficient statistics. In the following, we will base our rate estimates on 10% heavy-ion running (10^6 s/year, e.g. a few 10^7 central events collected for off-line analysis).

The main emphasis will be on data taking at the highest possible energy density, i.e. with Pb beams. In addition, running with one or two intermediate-mass ion species will provide the necessary means to vary the energy density [12]. Running with protons will be required initially to commission the detector and to provide reference data for the nuclear programme. Schemes are under investigation that would allow parasitic pp running at luminosities adapted to the rate capability of the detector without having an adverse influence on the high-luminosity interaction regions.

1.2.2 Acceptance

The rapidity acceptance has to be large enough to allow the study of some variables on an event-by-event basis (particle ratios, p_t spectra, HBT radii), meaning typically several thousand reconstructed particles per event (see chapter 4). Good efficiency for detecting the decay of particles at $p_t < m$ requires about 2 units in rapidity (for masses above 1–2 GeV) and corresponding coverage in azimuth. In particular, efficient rejection of low-mass Dalitz decays, which is needed for the lepton-pair measurements, can only be approached with full azimuthal coverage (see 4.4). The rapidity coverage of our central detector ($|\eta| < 0.9$) has been chosen as a compromise between acceptance and cost.

In order to have some sensitivity to the global event structure and long-range correlations on scales

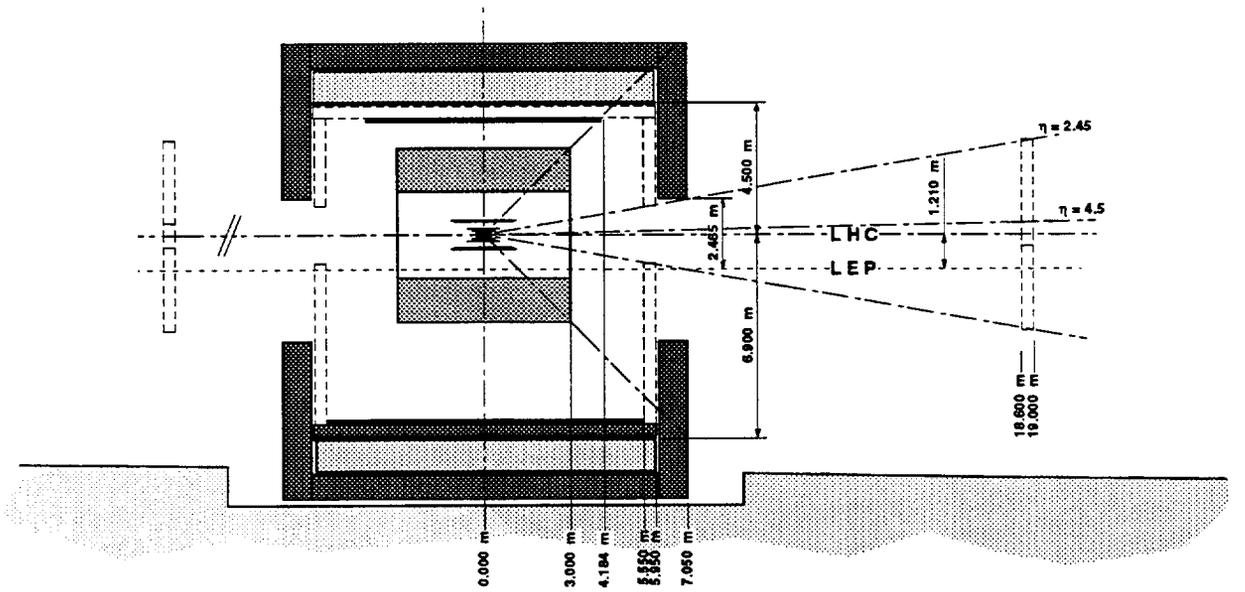

Figure 1.1: Longitudinal view of the ALICE detector

$\Delta y \gg 1$ (e.g. 'bubbles' of QGP, critical phenomena associated with a first-order phase transition), we will measure $dN_{ch}/d\eta$ with multiplicity detectors in a large rapidity window ($|\eta| < 5$) outside the central acceptance.

1.2.3 Tracking and Momentum Resolution

Pattern recognition in the environment of heavy-ion collisions at LHC presents one of the most challenging problems for the detector. The design of our tracking system has therefore primarily been driven by the requirement for safe and robust pattern recognition. It uses mostly three-dimensional hit information and dense tracking with many points and a weak magnetic field.

The momentum cut-off should be as low as possible (< 100 MeV/c), in order to study collective effects associated with large length scales. A low-p_t cut-off is also mandatory to reject the soft conversion and Dalitz background in the lepton-pair spectrum (see 4.4). The most stringent limit on momentum resolution in the low-p_t region is posed by identical particle interferometry owing to the large source radii and the corresponding narrow correlation enhancement (see 4.3). In the intermediate energy regime, the mass resolution should be of the order of the natural width of the ω and ϕ in order to maximize the signal-to-background ratio and, more important, to study mass and width of these mesons in the dense medium (see 4.4). At high momenta, the resolution has to be sufficient to measure the spectrum of jets via leading particles. Our tracking system together with a weak (0.2 T) solenoidal field fulfils the above requirements (see chapter 4).

1.2.4 Particle Identification

The momentum range for particle identification can be limited for the bulk of the hadronic signals to a few times the average p_t (>97% of all charged particles are below $p_t = 2$ GeV/c, less than 0.02% above $p_t = 5$ GeV/c). Good π/K/p separation (better than 3–4σ) is needed on a track-by-track basis for the abundant soft hadrons below 2 GeV/c in order to study HBT with identified particles, decays (hyperons, $\phi \rightarrow$K K), and event-by-event particle ratios. A statistical analysis (separation better than 2–3σ) will be sufficient to measure inclusive particle ratios and p_t spectra in the minijet region. The e/π rejection has to be sufficient to reduce the additional combinatorial background by misidentification to below the level remaining from unrejected Dalitz pairs (see 4.4).

1.2.5 Photon Detection

The accuracy of the single inclusive photon spectra will be determined in the range of interest ($p_t < 10$ *GeV*/c) by systematic errors on photon-reconstruction efficiency and the knowledge of the decay background. A 5% sensitivity requires a knowledge of the reconstruction efficiency as well as the π^0 cross-section to $\leq 3\%$ and the η cross-section to

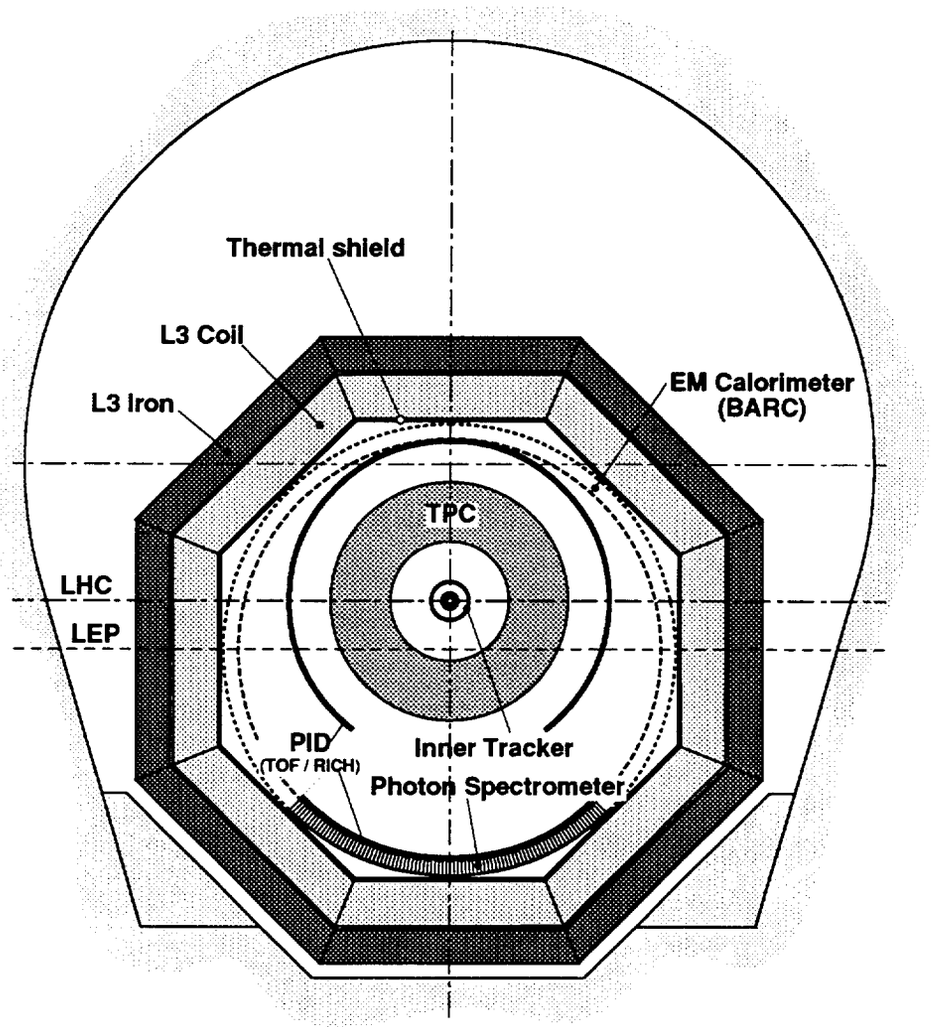

Figure 1.2: Transverse view of the ALICE detector

$\leq$ 10%. An acceptable systematic error can be obtained only at low channel occupancy and therefore requires a calorimeter with small Molière radius at a large distance from the vertex ($d \geq 6$ m, see 2.6). The minimum size is determined by the acceptance for the 2γ decays of π^0 and η at low p_t (≥ 1 GeV/c). The signal-to-background ratio in the two-photon invariant mass spectra improves proportionally to the energy resolution of the calorimeter.

1.3 Detector Overview

The overall detector layout of the ALICE experiment is shown in figs. 1.1 and 1.2. The central part, which covers $\pm$ 45° ($|\eta| < 0.9$) over the full azimuth, is embedded in a large magnet with a weak solenoidal field. It consists (from inside out) of an inner tracking system with five layers of high-resolution tracking detectors, a cylindrical TPC, a particle identification array (TOF or RICH detectors), and a single-arm electromagnetic calorimeter. A number of smaller trigger detectors (zero-degree calorimeters and multiplicity counters array) are not shown. The dashed areas (labelled FEC, NEC, and BARC) show the place that could be occupied by large-acceptance electromagnetic calorimeters, whose feasibility is currently under investigation.

1.3.1 Magnet

The optimal choice for our experiment is a large solenoid with a weak field. The choice of a weak and uniform solenoidal field with zero radial component together with continuous tracking in a TPC eases considerably the task of pattern recognition. The field strength — a compromise between momentum

resolution, low momentum acceptance, and tracking efficiency — will be 0.2 T, allowing full tracking and particle identification down to $\approx$ 120 MeV/c in p_t. Lower momenta are covered by the inner tracking system. The inner radius of the magnet has to be sufficiently large to accommodate a single-arm electromagnetic calorimeter for prompt photon detection, which must be placed at a distance of $\approx$ 6 m from the vertex, because of the particle density.

The magnet of the L3 experiment would fulfil all these requirements. It could be left at its present position centred 1.2 m below the LHC beam height. If it should not be available, we consider building a solenoid with somewhat smaller dimensions, which would fit into any of the standard LEP intersection regions. However, this would restrict our physics programme.

An earlier option, a small and extremely thin superconducting solenoid surrounding a silicon tracker [6], has been abandoned because we are confident that the proposed configuration can handle the expected particle multiplicities better.

1.3.2 Inner Tracking System

The basic functions of the inner tracker — secondary vertex reconstruction of hyperon decays, particle identification and tracking of low-momentum particles, and improvement of the momentum resolution — are achieved with five barrels of high-resolution detectors. The number of planes and their position has been optimized for efficient pattern recognition. Because of the high particle density, the innermost three layers ($r \leq 22$ cm) need to be truly two-dimensional devices, e.g. silicon pixel or silicon drift detectors. For the second superlayer at $r \approx 50$ cm, at least one and possibly both layers could be equipped with micro-strip detectors. Both silicon and gas micro-strips are being studied; the final choice will be made depending on tracking efficiency and cost. Three to four layers will have analog readout for independent particle identification via $\mathrm{d}E/\mathrm{d}x$ in the non-relativistic region, which will give the inner tracking system a stand-alone capability as a low-p_t particle spectrometer.

1.3.3 Time Projection Chamber

The need for efficient and robust tracking has led to the choice of a TPC as the main tracking system. In spite of its drawbacks concerning speed and data volume, we have concluded that only a conservative and redundant tracking device can guarantee reliable performance at up to 8000 charged particles per unit of rapidity. The inner radius of the TPC (r = 100 cm) is given by the maximum acceptable hit density (0.1 cm^{-2}), the outer radius of 250 cm by the length required for a $\mathrm{d}E/\mathrm{d}x$ resolution of $< 7\%$. With this resolution the TPC can serve, in addition to tracking, as a detector for electron identification up to momenta of $\approx$ 3 GeV/c. The design of the readout and of the end plates, based on ongoing developments for other heavy-ion TPCs, as well as the choice of the operating gas are optimized for good double-track resolution.

1.3.4 Particle Identification System

A number of technologies are under study for the hadron identification as alternatives to a straightforward and proven system based on scintillators and single photomultipliers, which is beyond the financial scope of this experiment.

For the first alternative, based on time of flight, a number of different options are currently under test: Pestov spark counters, parallel plate chambers and a scintillator grid with position-sensitive photo multiplier (PM) readout. Of these, the Pestov counter will be the preferred choice if it can be shown that large area systems can be reliably manufactured and operated.

The second alternative, which is undergoing an R&D project, is a proximity-focusing RICH detector with liquid Freon radiator, solid photocathode, and pad readout.

Depending on the final choice of technology and performance, the particle identification system will be placed at radii between 3 m and 4.5 m. A second small acceptance system in front of the e.m. calorimeter will extend the accessible momentum range and, in addition, serve as a charged-particle veto.

1.3.5 Photon Spectrometer

Prompt photons, π^0's and η's will be measured in a single-arm, high-resolution electromagnetic calorimeter. It is located 6 m from the vertex and covers 25 m^2 with $\approx$ 50k channels. It has to be built from a material with small Molière radius, to reduce the occupancy, and high light-output, to reduce the readout noise for the low energy of interest (normal PMs are excluded in the magnetic field). A number of dense detection materials are considered, of which $PbWO_4$, a scintillating crystal, seems best suited for our application. For most of these materials, a readout with silicon photo diodes would be feasible.

1.3.6 Large Rapidity Detectors

A multiplicity counter array close to the interaction region will measure the pseudorapidity distribution of charged particles over a large fraction of the phase space ($|\eta| < 5$). A number of options are under study, including a set of micro-channel plates inside the vacuum of an enlarged beam pipe, and silicon pad detectors or micro-strip gas chambers outside the beam pipe.

A set of small calorimeters (13×13 and 22×22 cm^2 wide, 100 cm deep) will be used to measure and trigger on the impact parameter of the collisions. They are made of tungsten with embedded quartz fibres, read out by PMs, and located on both sides of the interaction region $\approx$ 90 m downstream in the machine tunnel.

1.4 Future Options

The present detector, with its modular design and open geometry, is flexible enough to allow, at some later stage, modifications or upgrades if these should be desired. In particular, the free space available in the L3 cave, both in the radial and in the longitudinal directions, could be equipped with additional detectors, if the physics should justify a larger acceptance or suggest focusing on specific signals (e.g. physics outside mid-rapidity, continuum lepton pairs with m > 1–3 GeV). If the experiment should be housed in the L3 magnet, the outer two layers of muon chambers could be left in place. By exchanging the inner tracker with a passive absorber, a measurement of high-mass dimuons along the lines of Ref. [10, 21] could be feasible with only minor modifications already in the first years of operation.

References

[1] Proc. of the 9th Int. Conf. on Ultra-Relativistic Nucleus–Nucleus Collisions, Gatlinburg, USA, Nucl. Phys. A544 (1992).

[2] Large Hadron Collider Workshop, Aachen, FRG, 1990, CERN 90–10, Vol. I, p. 188–217, and Vol. III, p. 1057–1235.

[3] Design Study of the LHC, CERN 91–03 (1991).

[4] H. Satz, Nucl. Phys. A544 (1992) 371c.

[5] U. Heinz, Proc. Gen. Meeting on LHC Physics & Detectors, Evian, France, March 1992, p. 95.

[6] J. Schukraft, in ref.[5] p. 479.

[7] G. Jarlskog, in ref.[5] p. 511.

[8] L. Ramello, in ref.[5] p. 527.

[9] M. Markytan et al., CMS Letter of Intent, CERN/LHCC 92–3.

[10] A. Aziz et al., L3P Letter of Intent, CERN/LHCC 92–5, and CERN/LHCC 92–14.

[11] Workshops on Experiments and Detectors for a Relativistic Heavy Ion Collider, Brookhaven (1985) BNL–51921, Berkeley (1987) LBL–24604, Brookhaven (1988) BNL-52185 and (1990) BNL–52262.

[12] F. Karsch and H. Satz, Z. Phys. C51 (1991) 209.

[13] L. Van Hove, Nucl. Phys. A461 (1987) 3c.

[14] H.R. Schmidt and J. Schukraft, preprint CERN/PPE 92–42, to be published in J. Phys. G (1993).

[15] J. Bartke et al., Internal Note ALICE/PHYS 93–12

[16] C. Berger and W. Wagner, Phys. Rep. 146 (1987) 1.

[17] S. Sadovsky, Internal Note ALICE/PHYS 93–7.

[18] G. Baur, Z. Phys. C54 (1992) 419.

[19] G. Baur and L.G. Ferreira Filho, Nucl. Phys. A518 (1990) 786.

[20] J. K. Bienlein, Crystal Ball, DESY 92–083 (1992).

[21] M. Chen, L3H - CERN/LHCC 93–15

2 Detector Sub-systems

2.1 The Magnet

The choice of the magnet is a key issue of the experiment and has been the subject of an extensive study [1, 2]. We have opted for a large-volume solenoid with uniform magnetic field along the beam direction.

Such a solenoid will have to be large enough to contain:

a) all the tracking devices in the uniform-field region, thus easing the track-finding and reconstruction, a crucial issue in the high-multiplicity environment of heavy-ion interactions.

b) the particle identification devices and the electromagnetic calorimeter, thus minimizing the amount of matter between them and the interaction point, a crucial issue for the study of prompt photons.

For this purpose, an inner diameter of about 10 m is found to be necessary (see chapter 4). A weak magnetic field of ≈ 0.2 T will then be sufficient to provide the required momentum resolution while still letting the low-momentum particles reach the farthest detectors.

2.1.1 Using the L3 Magnet

Amongst the solenoids of the four LEP experiments, only the L3 one has a coil with the inner diameter large enough to fulfil the above requirements. Its field homogeneity would suffice for the operation of the TPC, although care would be required in the TPC calibration near the end caps in order to correct for the non-zero radial component of the magnetic field. The present LEP position of the L3 magnet is perfectly suited for our physics programme since, being asymmetric with respect to the beam axis of LHC, it allows the photon spectrometer to be placed at the required distance from the interaction point.

In addition, we could benefit from the higher design field of the L3 magnet to improve the momentum resolution for a part of the physics programme where this might be desirable (HBT, high-p_t phenomena). Another possibility, which, however, has not been studied in detail, could include the L3 high-precision muon chambers. After some operation time, the inner silicon tracker could be replaced by a passive or active hadron absorber in order to measure di-muons in the TPC and in the outer two layers of the muon chambers — possibly left in place — along similar lines as mentioned in Refs. [3, 4].

The geometry of the L3 pit is, moreover, well-suited for future upgrades of the experiment aimed to extend its particle detection capabilities and/or its phase-space coverage (see e.g. 2.8).

2.1.2 Designing a New Magnet

If the L3 magnet and its pit were not available to our experiment, a similar magnet of somewhat smaller size could be built, fitting into a standard LEP hall. However, this option would curtail the possible physics programme and the choice of detector arrangements because of the reduced space available both in the transverse and in the longitudinal directions. The PHOS spectrometer would have to be placed somewhat closer, the occupancy in the RICH would be increased by about a factor of two, and most of the options mentioned in chapters 1.4 and 2.8 would be excluded.

The outer diameter of such a solenoid is limited to less than 10 m by the dimension of the standard LEP access shaft. For reasons of cost a very simple arrangement of iron slabs is considered for the flux return yoke and for the end caps. The same argument leads to a non-welded Al solenoid, subdivided into 10 equal coils [5] This layout is based on a similar study made for the ATLAS Collaboration [6].

The overall dimensions of this design and, owing to the low field of 0.2 T, the weight of $\approx$ 3000 tons are similar to the standard LEP detectors.

2.2 The Inner Tracking System

The Inner Tracking System (ITS) will measure charged particles at radii up to 50 cm. Its main purpose is the detection of secondary vertices and the momentum measurement of of low-p_t particles, down to a p_t of $\sim$ 20 MeV/c for electrons. It will also improve the momentum resolution at large momenta (see 4.1.3). In addition, it will perform the identification of the low-momentum particles which do not reach the outer particle identification devices, via dE/dx in the $1/\beta^2$ region.

The system will consist of five cylindrical layers, covering the central rapidity region ($|\eta| \leq 0.9$) for vertices located within the length of the interaction region (2σ), i.e. 10.6 cm along the beam direction (z). A half-section of the system is shown in Fig. 2.1, while the nominal dimensions are summarized in Table 2.1.

The criteria which led to the definition of the number and location of layers are discussed in section 4.1, together with the simulated performance of the system.

The granularity required for the innermost planes can be achieved only with silicon micropattern detectors with two-dimensional readout, such as Silicon Pixel Detectors (SPDs) and Silicon Drift Detectors

Layer	r (cm)	$\pm z$ (cm)	Area (m^2)
(1)	7.5	12.8	0.12
(2)	14	19.3	0.34
(3)	22	27.3	0.75
(4)	46	51.3	2.97
(5)	50	55.3	3.47
Total Area = 7.65 m^2			

Table 2.1: Dimensions for the inner tracking system

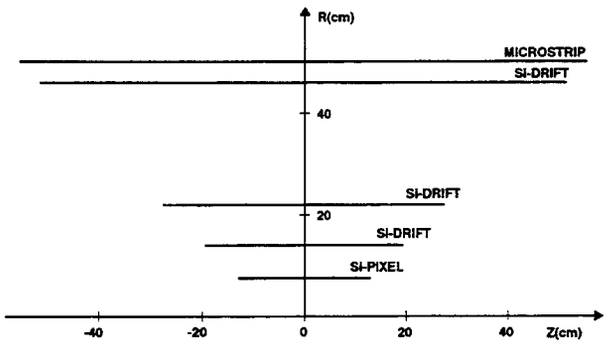

Figure 2.1: Transverse half-section of the inner tracker

(SDDs). Another technology which provides excellent granularity, namely CCDs, cannot be applied because the readout speed is at least an order of magnitude too low.

No large system using either of these detector technologies has ever been operated, and an important R&D effort will be necessary to finalize the design. Yet, on the basis of the ongoing development programmes, both within and outside our collaboration, we believe that the essential issues can be solved within two years, i.e. in time to start mass production of the detector components. In particular, the STAR [7] experiment at RHIC plans to build a large-area vertex tracker using SDDs, and several p-p experiments at the LHC and SSC plan to use SPDs for their innermost tracking plane(s). It must be stressed that the lower radiation and event rate in this experiment compared with the p-p ones should make the implementation of pixel detectors easier.

As a baseline design, we consider using SPDs for the innermost plane, the most demanding one in terms of granularity and resolution, and SDDs for the following two. A configuration in which only one of these technologies would be applied might still be considered, if it could be proven to satisfy all the requirements at all radii, and to provide a system which would be simpler to construct and operate.

At larger radii, the requirements in terms of granularity are less stringent, so that for at least one or possibly both planes we foresee the use of a more standard, well-proven and cheaper technique, like double-sided silicon strip detectors [8] or MicroStrip Gas Counters (MSGCs) [9]. The outer layers have large areas, and involve the use of a large number of detectors, so that reliability, ease of operation, and established capability of industrial production become major points in favour of a conservative choice. The MSGCs are cheaper than Si–strips, but have a lower two-track resolution for inclined tracks; also, double-sided silicon microstrips offer the possibility of matching the signals read out from the two sides, to help resolve ambiguities. A final choice will have to wait for more-detailed simulations and the optimization of the track finding algorithms.

The main parameters of each of the four detector types considered are indicated in Table 2.2: spatial precision, two-track resolution, pixel size, size and number of channels of an individual detector and number of output lines from a detector module.

In Table 2.3 the main parameters of the various layers are summarized, including the number of detecting elements, the number of electronic channels, and the power dissipated. The different detector technologies require specific front–ends, and we foresee the unification of electronic standards (type of links, protocols) at the level of optical links, i.e. at the front-end outputs.

The detectors and their front-end electronics will produce a large amount of heat (see Table 2.3) which has to be removed while keeping a very high degree of stability. In particular, the SDDs demand temperature stability and monitoring in the 0.1 °C range. For these reasons, particular care is being taken in the design of the cooling system, and several schemes are being considered. We favour an ambient-temperature evaporative cooling scheme, which should allow a uniform and stable temperature, with minimal stresses at turn-on and switch-off. To minimize the amount of material, we will also pursue the study of gas cooling, hoping to apply it to the innermost plane(s).

To ensure a flexible system, we are developing a structure that is mechanically independent from the outer detectors, and can be preassembled and measured accurately before final installation in the experiment.

Since for the bulk of the interesting tracks the momentum resolution will be limited essentially by multiple scattering, the minimization of the material thickness is an absolute priority. To this purpose, we are studying a support structure in which the material is concentrated in the conical endplates, covering a minimum solid angle, and the detectors are orga-

Type	Spatial precision (μm)		Two-track resolution (μm)		Cell size (μm)	Module size (mm)	Channels per module	Output lines
	$r\phi$	z	$r\phi$	z				
Pixel	22	78	150	540	75x270	4.8x69	16384	32
Drift	25	25	500[a]	200[a]	-	57x70	448	448
Si Strip[c]	30[b]	1000	200	7000	100x50000	75x50	2x750	24
MSGC[c]	60	1000	800	12000	200x25000	100x50	2x1000	32

[a] Can be improved with waveform analysis
[b] Can be improved with centroid finding
[c] Layer at $r = 50$ cm

Table 2.2: Parameters of the various detector types

Layer	Type	Detector modules	Electronic channels (k)	Barrel dissipated power (W)	Endplates dissipated power (W)
(1)	Pixel	400	6550	160	
(2)	Drift	96	45	75	430
(3)	Drift	192	90	150	860
(4a)	Drift	765	350	600	3400
(4b)	Si Strip	900	1440	1850	
(5a)	Si Strip	924	1400	1800	
(5b)	MSGC	700	1400	1800	
			~8500 to ~9600	~2800 to~4000	~4700

Table 2.3: Physical parameters of layers

nized in ladders, parallel to the beam direction and held by ribs that are also used as flow channels for the cooling fluid and possibly as substrate for power distribution. With this design, we plan to keep the total average thickness, including detectors, below 0.6% of X_0 per layer.

2.2.1 The Silicon Pixel Plane

Silicon pixel detectors couple excellent spatial precision with optimum two-track resolution; thanks to the very small capacitance of the detector, they have an excellent signal-to-noise ratio. In addition, they feature simple calibration and alignment. Given the small area of the first layer, their main drawback, which is the cost per unit area, does not play a significant role.

We plan to adopt a pixel size of the order of 75×270 μm^2: this gives a resolution of 22 μm in the bending plane and of 78 μm in z. These values match what is obtainable with present technology, i.e. a width of the pixel of 75 μm and an area of 20000 μ m^2. The occupancy figure is excellent even in this high-track-density environment: 0.4% at $\eta = 0$, including primary particles only.

Our pixel development is based on the CERN-LAA programme [10], now continuing as RD19 [11]: the detector consists of a two-dimensional array of detecting elements with a granularity, at present, of 75×500 μm^2 with in situ signal processing and a digital output. An analog output with peak detector is also being studied. Two different approaches can be followed: either the monolithic or the hybrid one [12]. The efforts in RD19 are in both directions, but the hybrid approach seems to be more flexible allowing the separate development of the detector and of the electronics chip. The connection between the two parts is done via indium bump bonding.

Several of detectors and readout chips have to be grouped on a ladder structure. Ladder modules will be used for the first time in the OMEGA-ION (WA97) experiment at CERN, in order to construct a 50×50 mm^2 array, which will provide the proof of principle for the proposed assembly. The technical aspects of this implementation are currently under study in the framework of RD19.

The basic unit for the hybrid pixel detector will be a matrix of 64×32 elements of 75×270 μm^2 area corresponding to 4.8×8.64 mm^2 for each detector chip. Eight readout chips will be mounted contiguously on a silicon-base detector module to cover a sensitive area of 4.8×69 mm^2 per ladder, corresponding to about 16400 sensitive cells. This size is compatible both with 4-inch silicon wafers, which are the industry standard, and with the practical limit of about 1 cm^2 for the readout chip.

The area of the readout chip is larger than that of the detector chip, consequently a 'turbo detector assembly' [12] has to be adopted. The required cylinder length at $r = 7.5$ cm is obtained with four ladders in line (276 mm). To cover the lateral surface of the cylinder, 400 ladders distributed on 100 tiles for a total of about 6.5×10^6 sensors are needed. We believe that the thickness of the detectors, currently 300 μm, can be decreased somewhat, perhaps to $\sim$ 200 or even 150 μm, and the electronics can be thinned safely down to 100 or even 50 μm. Finally, the bump bonding introduces few μm of silicon-equivalent thickness, if averaged over the whole area.

The block diagram of a possible readout chip is shown in Fig. 2.2, inspired by the chip which was successfully tested in the OMEGA-ION (WA94) experiment by the RD19 group [13, 14, 15]. For this test each plane had a sensitive area of 8×4.725 mm^2 and a 16×63 pixel matrix with a pixel size of 75×500 μm^2 (using the 3 μm mask technique). The signal from the pixel is corrected for leakage current by an external current (IFN) and brought to a charge sensitive amplifier with an externally controllable gain (IDIS1). Then follows the discrimination stage with adjustable threshold(IDIS2); the discriminated signal passes an adjustable delay (up to 1.5 μs) and sets a flip flop in coincidence with an external strobe derived from the trigger which can be as narrow as 150 ns excluding almost totally event pile-up and allowing a relatively long trigger decision time at almost no detector dead time. The delayed signal also resets the discriminator (self clearing mode). The flip flops of one column of 63 pixels are organised in a shift register which is clocked out to one of the 16 (32 in our new design) outputs. A sixtyfourth row is present on the electronics chips for electrical testing and for checking the continuity of the shift register. Using the existing chip [15], the total readout time of all the 63 16-bit words is $\sim$ 12 μs, at 5 MHz clock frequency. A 10 MHz micropower front-end circuit for direct readout of pixel detectors has already been made in the framework of the CERN-LAA project [10].

The whole layer corresponds to about 6.5×10^6 channels. We aim to have 320 leads leaving the detector from each side, i.e. 10 data buses, each grouping 20 ladders. Assuming a conservative multiplexing rate of 10 MHz, the readout time is 1 ms.

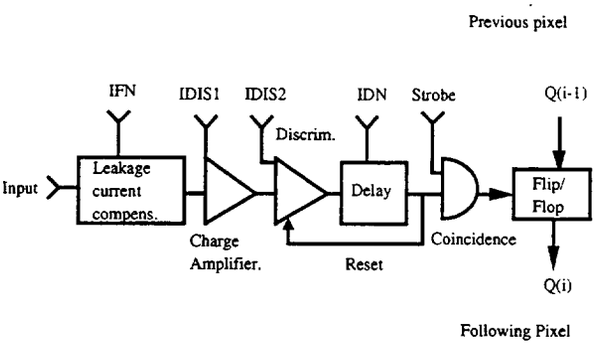

Figure 2.2: Block diagram of the digital pixel element readout circuit

The total heat produced by the readout electronics is about 160 W, i.e. 25 μW/channel, using the present 3 μm technology. We foresee to obtain the required reduction of size, compared with the existing chip, by going to 1.2 μm technology, now an industry standard. This would also reduce the power consumption of the chip, while allowing a further increase in speed.

2.2.2 The Silicon Drift Planes

Like gaseous drift detectors, SDDs [16, 17] exploit the measurement of the transport time of the charge deposited by a traversing particle to the collection electrodes to localize the impact point in one of the dimensions, thus enhancing resolution and multitrack capability at the expense of speed. They are ideally suited to this experiment in which very high particle multiplicities are coupled with relatively low event rates. Although SDDs are not yet commonplace in HEP experiments, they have been successfully employed in the NA45 experiment with ion beams at the CERN SPS [18], and several groups in the Collaboration are currently gaining experience with them [1]. The main item for the current R&D effort is the establishment of production of SDDs in industry, which we plan to accomplish within a year.

In NA45, a cylindrical SDD has operated with an average track density of 13 particles cm^{-2} over the whole detector, and up to 0.66 mm^{-2} in the central region, values which are much larger than the ones foreseen here. The overall efficiency, including detector and electronics, was 96%, and the homogeneity, again including the effect of both charge collection

[1] In the NA45 and WA93/WA98 experiments and in a dedicated R&D effort.

and electronics gain, was better than 6.5%.

A linear SDD has on both surfaces of the high-resistivity n-type silicon wafer a series of parallel, implanted p^+ field strips, which are connected to a voltage divider. They provide the bias to fully deplete the volume of the detector and an electrostatic field parallel to the wafer surface, thus creating a drift region. Electron-hole pairs are created by charged particles crossing the detector. The holes are collected by the nearest p^+ electrode, while the electrons are focused into the middle plane of the detector. The superimposed drift field forces the electrons to drift parallel to the wafer surface towards the edge of the detector where they are collected by an array of anodes composed of n^+ pads. The small size of the anode, and hence its small capacitance ($\sim$ 50 fF), makes very low noise levels attainable.

Owing to the diffusion and mutual repulsion during the drift, the electrons reach the anode region with a Gaussian distribution. The coordinate perpendicular to the drift direction is measured by the position of the centroid of the collected charge. A space precision of better than 25 μm in both coordinates can be obtained for most of the detector surface. The local precision has been measured with a laser to be better than 10 μm, while $\sim$25 μm includes the inhomogeneities in the drift velocity, which can in principle be corrected for. Only very close to the anode array is the second coordinate measured with less accuracy since the charge is collected on one pad only. A two-track resolution of 150 μm is feasible by performing a detailed waveform analysis [19, 20], while 500 μm can be considered a worst-case figure. In NA45 a two-track resolution of 180 μm has been obtained, in the drift direction, by applying a double-pulse fit.

The drift time depends on the drift velocity of the electrons and therefore on the electron mobility ($v_{drift} = \mu \cdot E$). The mobility of the electrons is temperature dependent, being $\mu \sim T^{-2.4}$, so that a temperature variation of about 0.1°C, corresponds, on average, to a $\sim$ 10 μm change of the position of the reconstructed points. This requires a very accurate stabilization of the temperature and continuous and accurate calibration of the drift velocity.

A possible calibration method is by injecting electrons at a well-defined position of the detector and measuring the corresponding drift time. For this purpose a MOS injector can be integrated on the detector near the central electrode. Another option would be to inject charge by means of an infrared laser, e.g. Nd:YAG, for which the absorption length in silicon is about 1 mm. In addition, this method could be used to monitor the position of the detectors in space.

We are developing a detector design suitable for production by industry, but in the following we will refer to an SDD design which has been developed for the STAR experiment at RHIC, shown in Fig. 2.3.

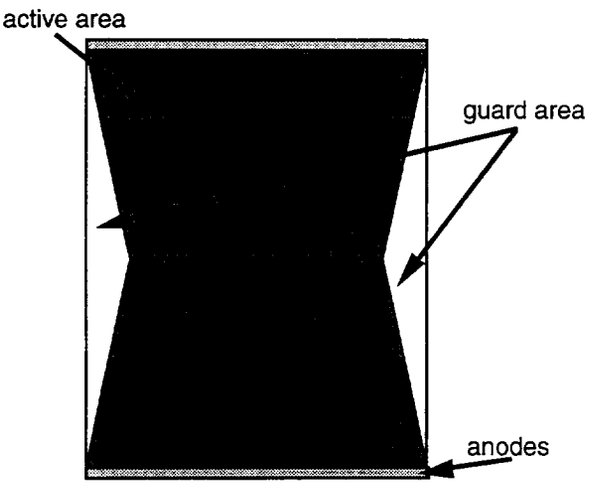

Figure 2.3: Sketch of the STAR2 design for the STAR experiment at RHIC

The sensitive area is split in two parts so that electrons drift in opposite directions in the two halves of the detector. The central electrode is the p^+ strip at the highest, negative, potential. In this way the maximum drift length and the required drift field are reduced by a factor of two with respect to an SDD having the anode pad array on one side only. Moreover the two half-chambers share part of the guard region, limiting dead zones. A similar detector has been built and tested [21] for the UA6 experiment at CERN.

The detector will be fabricated from a 4-inch high-resistivity NTD silicon wafer, of 300 μm thickness, so for optimum use of the silicon we assume that each SDD is 7 cm in length and 5.7 cm in width. The anode pitch is 250 μm, so each detector has 224 anode pads on each end. Typical drift velocities in SDDs are $\sim$ 6 μm/ns, which would imply a total drift time of $\sim$ 6 μs. The charge cloud will reach the collecting anode with a r.m.s. radius of $\sim$ 200 μm for the maximum drift length.

The detectors will be organized in ladders, with the detectors mounted end to end. In this way, the dead area corresponding to the voltage divider (12% of the area for STAR2) is along the side of the ladder, so that it can be covered by tiling the adjacent ladders. Tiling of course increases the amount of material, so the design of the voltage divider and of the guard areas will be subject to careful optimization.

In our baseline design, we assume that the SDDs will be positioned so that the electrons drift parallel

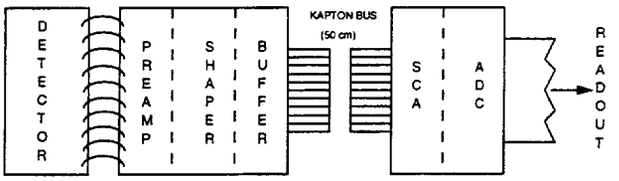

Figure 2.4: Scheme of a possible readout chain for the SDDs

to the beam axis and therefore to the magnetic field. We are also studying the possibility of aligning them with the drift perpendicular to the magnetic field, a solution which would simplify the cooling of the electronics. The low magnetic field would have no adverse effect on resolution.

Front-end Electronics

Some of the key parameters of the readout, like the optimum shaping time and the sampling frequency, will depend on the details of the final design of the detector, which will determine the total drift time and pulse width, but a concept of the readout chain has been developed on the basis of relatively general assumptions, which are still subject to optimization.

Each anode pad is wire-bonded to a low-noise preamplifier-shaper with a peaking time of <40 ns and a Gaussian shaping. The latter is dictated by the need to maximize two-track resolution. The noise level is essentially determined by the capacitance of the connection elements, which is at the level of 0.5 pF. With these constraints, we have developed a design in bipolar technology which can achieve an Equivalent Noise Charge (ENC) of less than 400 electrons, and has a differential output capable of driving a short cable connection to the next stage. This noise level is more than adequate to reach our design goal of a spatial resolution better than 25 μm. For this design the power consumption is contained below 1 mW per channel.

Although it would provide a somewhat better noise performance, we do not intend to pursue the integration of the first stage of the preamplifier on the detector itself. This would involve additional complexity, which might increase significantly the cost of its industrial production, and introduce an extra source of heat on the detector itself, which might be difficult to cool efficiently. On the contrary, we believe that the integration of the voltage divider is important to avoid handling a large number of high-voltage lines in the system.

The short cables, which we plan to make on a very thin kapton ribbon with dense traces of $\sim$ 100 μm pitch, will carry the signals to an analog memory mounted on the detector end-plates. This could be a Switched Capacitor Array (SCA); such an ASIC exists [22] and has been tested with an acquisition rate of 40 MHz. In this case we would require a storage depth of 256 cells. The readout of the TPC requires an analog storage unit with similar characteristics, so we foresee a common development of this element of the readout and of the downstream circuitry for zero-suppression and transmission. When the full event has been stored on the SCA, data are clocked out to an 8 to 10 bit ADC (one per channel) to be digitized. The resolution for the ADC is dictated by the need of a large dynamic range to accommodate the large energy deposition of slow particles while maintaining good resolution for low charge deposits, as needed by the centroid finding algorithm. Digital data are then transmitted to the readout electronics where zero suppression is performed before transmission on fibre optic links. The scheme of the chain is shown in Fig. 2.4.

In this configuration, the power dissipated locally will consist of approximately 100 mW per detector for the voltage divider and $\leq$1.5 mW per channel for the front end. An additional $\sim$ 10 mW per channel will be dissipated by the SCA+ADC, which are located on the endplates, where cooling is not a problem.

2.2.3 The Strip Detector Planes

The Silicon Microstrips

Double-sided silicon strip detectors, i.e. silicon detectors with segmented readout electrodes implanted on both surfaces, can be considered well-understood, since a large system of more than 50000 channels is in operation in the ALEPH [23] experiment and more are under construction for other LEP experiments [24]. The excellent reliability and spatial resolution, down to the few μm level, of silicon strip detectors have been successfully exploited in large-scale systems by many experiments [25]. Double-sided silicon strip detectors are currently produced with good yield by several companies in Europe and in Japan.

The detectors will be used with the strips oriented along the beam direction. In this way, the resolution in the bending plane is essentially fixed by the pitch of the strips, although one can improve this value to better than 20 μm using a centroid-finding algorithm. The z coordinate, along the beam direction, is measured in each detector by using a small stereo angle between strips on the two sides. The z resolution obtained this way is modest for small stereo angles, but sufficient for pattern recognition. We assume 100 μm as pitch, which can be well matched with the pitch of the front-end electronics for direct bonding, and gives a resolution of 30 μm. At R = 50 cm, requiring 2%

occupancy for a single strip, and 1 mm z-resolution, the required strip length is 5 cm and the stereo angle 30 mrad. In a cell defined by the area within which the presence of more than one track creates ghost hits (i.e. the width of a strip times the number of stereo strips crossing it), the occupancy would be 30%. Shorter strips could be used to reduce the ghost probability, while increasing the number of electronic channels and the cost of the device.

We are currently studying the efficiency of matching the signals from both sides of the detector in order to correctly associate the hits when two or more tracks cross the same cell. First results look encouraging for the expected signal to noise ratio.

The detectors will be fabricated out of 4-inch wafers, not using the outer half centimetre, and will have a size of 75 mm by 50 mm. The layer would have a polygonal section with 42 sides, or ladders, of 75 mm by 110 cm; the total number of detectors would be 924. The number of channels, taking into account that each detector is double-sided, would be ~1 400 000. The dimensions of a strip layer at $r = 46$ cm would be slightly different, adapted to the particle density [26].

We foresee an assembly of the detector and the electronics inspired by the one proposed for the SDC silicon tracking system [27]. The front-end electronics will be mounted directly on the detectors, and bonded to the strips, as shown in Fig. 2.5.

The electronics dies could be made as thin as 150 or even 100 μm to reduce the amount of material, and would cover, on average, about 10% of the detector area on each side. This assembly might require the addition of a thin layer of Be shielding under the electronics chips, to limit the pickup from the detector: the thickness of such a layer could be kept between 200 and 300 μm, i.e. about 25% of the thickness of the silicon itself in terms of radiation lengths, on about 20% of the detector area. This layer would also be used to transfer heat to the cooling pipes. The readout and control lines will be integrated with the support structure and the insulation layer. We therefore foresee a total thickness for the detector module of ~0.33% of X_0, not including cabling and cooling/support structures. We will study the possibility of installing connection lines to the strips on the detector itself across its width, using a double-metal technique, in order to place the electronics along the supporting ribs for easier cooling.

The dead area on the detector is defined by the need for a guard ring and a bias line to polarize the detector, for a total of approximately 500 μm from the edge of the detector, including a safety region next to the edge itself. In the proposed geometry, this

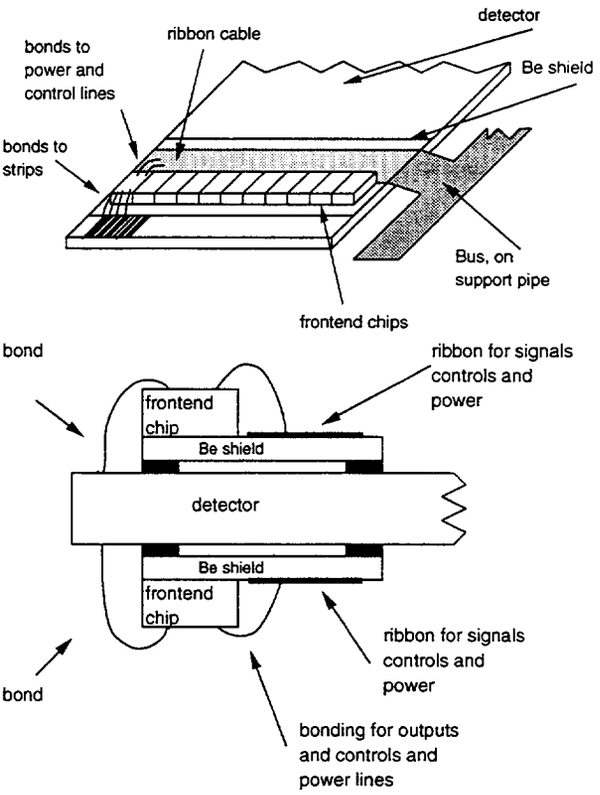

Figure 2.5: Global (top) and side (bottom) view of the module assembly

should introduce a maximum of 3% dead area, which, if desired, could be reduced by tiling the detectors. The bonding pads could be avoided, bonding directly to the metal on the strips, since they are sufficiently wide.

Front-end Electronics

We have examined different front-end options [28], concluding that a single preamplifier-analog pipeline-multiplexer chip should be built, using BICMOS technology. This allows an improvement of the performance of the bipolar frontend by eliminating the feedback resistor and replacing it by a CMOS switch, and arranging the front-end as a gated integrator. Since most other detectors foreseen in the tracking system of the experiment will have slow response, the integration time will be defined by the optimization of the signal-to-noise ratio. This is obtained at 60 ns shaping time with an ENC of $\sim$ 600 electrons for a detector capacitance $\leq$ 6 pF. In this scheme, it would be possible to design the first stage with a very low power, i.e. 100 μW. Since the rest of the electronics (multiplexer and ADC) has to be built in CMOS technology, it seems that BICMOS is the

best choice for the system, allowing the integration of the whole front-end in one chip. BICMOS processes are available now for full custom VLSI designs, and a preamplifier for silicon detectors has been successfully designed and produced [29].

The block diagram of the front-end electronics, which will be built as a single VLSI chip, is shown in Fig. 2.6. It includes the preamplifier/shaper, a sample-and-hold (S/H), an analog storage cell, the multiplexer, the ADC and the output buffer. It seems feasible to implement this design in a die of size acceptable for production with a good yield, i.e. around 6 mm by 5 mm for 64 channels. The interaction trigger would transfer data from the sample-and-hold to the storage cell, where it will wait for the trigger or the fast clear. The S/H could be made self-resetting to avoid integrating spurious hits. Given the slow event rate overlapping events during the decision time can be vetoed with a negligible loss. This way a pipeline is avoided, using a simple analog storage cell instead. In this scheme, the number of communication lines to the outside world is kept to a minimum. The output buffer, with the power consumption as discussed below, should be able to drive the connection lines up to the endplates, which are less than one metre away. A further element, driving the long cables or fibre-optic links to the readout buffers in the counting room and operating further multiplexing and/or data compression, will sit on the endplates.

The power consumption of the detectors will be relatively low, given the expected level of radiation. Even with pessimistic assumptions, the leakage current will remain in the tens of nA per strip range, giving a few μW of power consumption per channel. The dominant component will be the consumption due to the electronics, which includes at least 100 μW per channel for the first stage, 200 μW per channel for the rest of the preamplifier and, depending on the details of the architecture, about 1 mW per channel for the storage+multiplexer+ADC. The total power dissipation would be ~1.3 mW/channel, i.e. ~1.8 kW for the complete outermost layer.

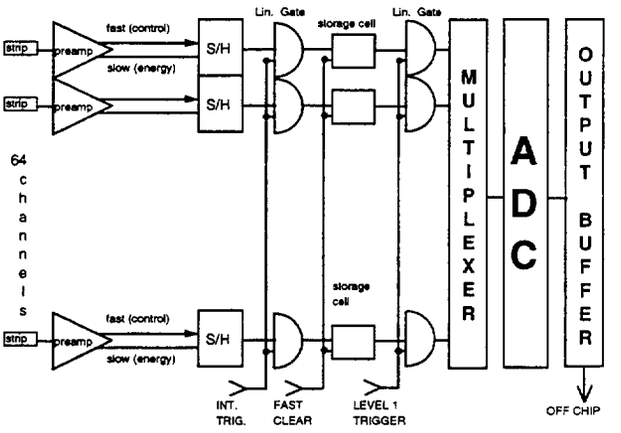

Figure 2.6: Block diagram of front-end chip for Si strips

The Microstrip Gas Counters

As an alternative to silicon strip detectors, we consider the use of MicroStrip Gas Counters (MSGCs). As mentioned above, a choice between these two option will be based on the impact on track finding and cost.

An MSGC consists of an insulating substrate, covered by metal anodes and cathodes (Fig. 2.7). The metal structure is put on the substrate with high precision by lithographic methods. The substrate is placed in a gas volume. Particle detection takes place in the same way as in conventional wire chambers. Since the substrate provides mechanical stability, the anodes and cathodes can be very close together and the anodes can be very thin. This results in fast detectors with high gas amplification factors and excellent spatial resolution [30], [31].

Research and development for the MSGCs as well as the digitizing electronics are being carried out within the CERN R&D project RD28 [32].

The glass substrates have moderate heat conducting properties, so the use of ceramic substrates will be investigated, since it would allow the transport of the heat generated by the electronics to a heat exchanger in the support system. One of the design goals is to lower the power dissipation enough to make forced-air cooling possible.

For the interconnection between the substrates we propose the use of strip-line techniques printed on foils. For connection to higher-level readout modules fibre-optic links are foreseen. We are currently working on the design of such a system.

When thin MSGC detectors are used to detect minimum-ionizing particles, their efficiency is mainly determined by the statistics of the primary electron-cluster production in the gas by the passing particle. Each anode collects only the charge released in the region directly above it (Fig. 2.7).

Therefore, the efficiency of MSGCs depends on the angle between the track and the normal to the anodes, which, for particles produced at the primary vertex, is determined by the strength of the magnetic field and the momentum of the particle. We have done simulations for various types of gases and magnetic fields and studied the efficiencies as a function of momentum. The efficiency of an MSGC at 50 cm from the interaction point is shown in Fig. 2.8

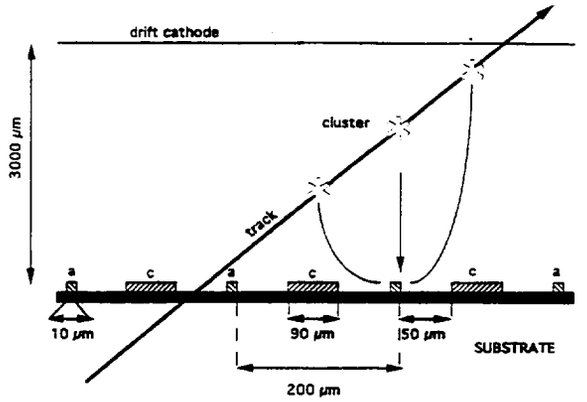

Figure 2.7: Electron production in a microstrip gas counter

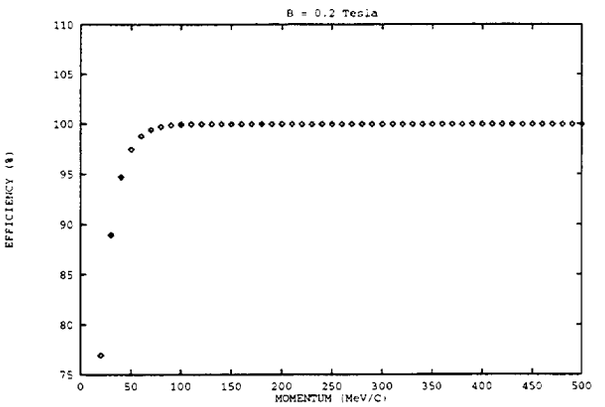

Figure 2.8: Microstrip gas counter efficiency versus transverse momentum in a weak field

as a function of the particle momentum, for a magnetic field of 0.2 T. The intrinsic detector efficiency is above 95% for track angles corresponding to momenta above 50 MeV/c.

The MSGC layer will consist of a cylinder, covered by MSGC detectors, in a stereo angle pair configuration. Each detector consists of two microstrip gas counters back to back, with the strips on the inside and two drift cathode planes on the outside. The microstrip structures are created on both sides of a 300 μm thick, 5×10 cm^2 glass substrate. The drift cathodes are two thin aluminized plastic foils. Thus the detector itself represents 0.3% X_0. The number of channels per stereo pair plane is chosen to give an average occupancy of 2%, i.e. ~1 400 000. A layer would consist of approximately 700 substrates of 5×10 cm^2.

The spatial resolution of MSGCs is mainly determined by the anode spacing and the anode length, although the drift gap width also has to be chosen carefully. In order to obtain 60 μm resolution in the bending plane an anode spacing of 200 μm is sufficient. In combination with a small gap width, to limit transverse diffusion of the electrons, this allows digital readout of the counters. Resolution significantly better than 60 μm require larger gap widths, analog readout and centroid-finding methods. With the required occupancy per anode of $\approx$ 2% the anode length will be 25 mm. The required resolution in the z direction of 1 mm is achieved with a stereo angle of 60 mrad. Since low-momentum tracks may generate signals in up to three anodes, the two-track separation is 800 μm in the bending plane and 12 mm in the z direction. However, when two tracks are in a single cell, ghost hits result, and the occupancy of these cells is 15%.

Front-end Electronics

As the MSGC detector is not intended to perform particle identification by means of $\mathrm{d}E/\mathrm{d}x$ measurement, and no charge matching between the two sides of a stereo pair is possible, an analog output is not necessary and a digital output consisting of hit patterns is preferred, since it reduces the volume of data.

If the readout is organized with one line per ladder exiting on each side, i.e. with about $2{\cdot}10^4$ channels readout on a line, a speed of ~40 MHz will be sufficient to keep the readout time well below 1 ms.

Several options with a custom-designed chip with low power consumption are currently under investigation. One possible option would be to use the same chip described for the silicon microstrips, but replacing the ADC with a simple comparator. Another one would be the use of sub-micron CMOS technology combined with low supply voltage (1.2-3 V); such circuits, running at 100 MHz clock rate, have recently become commercially available. The delay before a trigger decision is generated can be implemented on-chip either storing the analog information, e.g. using switched-capacitor techniques, or using a digital buffer. Of major concern is the amount of noise fed back into the analog front-end and into the microstrip anodes themselves. Data reduction by zero-suppression could be considered, although it is not a major advantage at these occupancies, since only one bit per channel will be recorded.

As a model of a possible chip configuration, one can consider the FASTPLEX chip which is being developed by CERN. This is a 32-channel design which uses a comparator directly behind the pre-amplifier with a digital delay line (shift register) and a zero-suppressed serial readout of three consecutive 32-bit 'hit-patterns' data frames. The maximum readout speed is 20 MHz and the power consumption is ap-

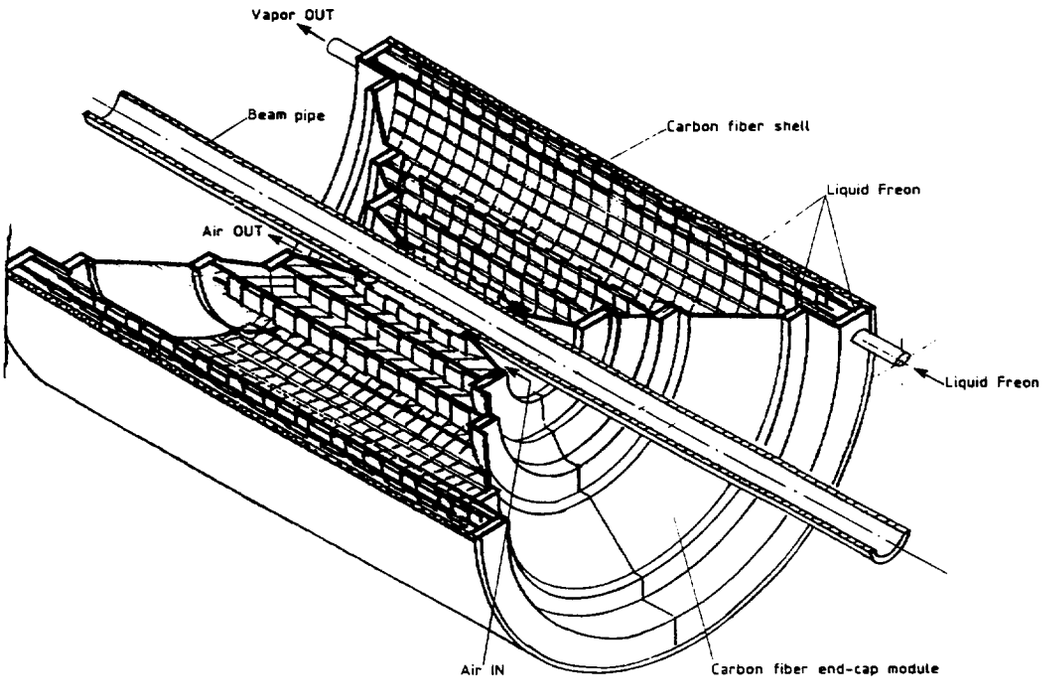

Figure 2.9: General view of one half of the vertex tracker

proximately 3 mW/channel.

2.2.4 Support and Cooling

The design of such a complex detector, involving the use of several different detection techniques, and with very demanding requirements for the temperature stability, the positioning precision and the total material thickness in the sensitive volume, is a task that requires a unified approach.

The cooling scheme ($\approx 3-4$ kW heat drain in the tracking volume) determines the overall mechanical construction. Preliminary studies of different cooling schemes have been done [33] for a higher heat load (10 kW) and two options were selected for future development:

– localized, evaporative cooling in a closed system under atmospheric pressure for the Si-drift, Si-strip (or MSGCs) detectors, that is expected to provide uniform temperature fields (within 3–4 °C in the detector volume) and a thermostabilization of the whole Inner Tracking System (ITS) of the order of 0.1 °C at ambient temperature.

– uniform gas-cooling of the first layer of pixel detectors with reasonable flow.

General Layout

The general layout of the Inner Tracking System is shown in Fig. 2.9.

It is composed of two cone carbon-fibre end-caps that integrate the pipes for the cooling fluid, data and power buses, connectors, optical transmission lines and the outer thin carbon-fibre honeycomb support shell. Part of the electronics will also be mounted on these plates, as mentioned above. The thin cone end-caps of the ITS limit showering and the interference with high rapidity detectors. The integration of the beam pipe into the mechanical structure is under study.

The main candidates among the lightweight materials for the mechanical support and cooling structure are Be (covered with a protective coating), BeO and carbon-fibre composites. We are also considering new materials, e.g. boron carbide foam, which is extremely light, has rather high mechanical properties and also has a coefficient of thermal expansion well matched to that of Si.

The detector modules are assembled in ladders supported by linear structures (ribs). Since the required thickness of the rib grows, for a given precision, as the fourth power of the length, we foresee for the outer layers two intermediate annular supporting membranes, made of thin carbon-fibre foil. The basic linear supporting structure, which is thermostabilized by the integrated cooling channels, schematically is shown in Fig. 2.10. It is formed by a carbon-fibre semicylindrical shell (diameter 5 mm, thickness 0.5 mm), which houses a Be pipe that serves as cooling channel and as power bus.

The thermoconductive Be will also provide a uniform temperature along the line, avoiding the formation of hot spots. If a solution is found to the problem of making a good joint between BeO and carbon fibre, so that a thin BeO layer could be used to hermetize

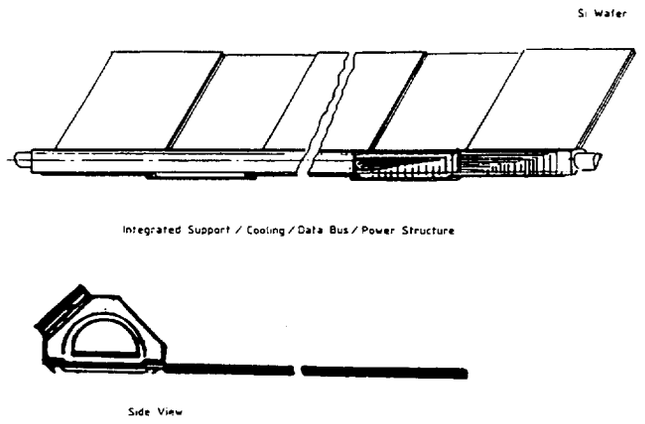

Figure 2.10: Scheme of the ladder, integrating cooling, power bus and data bus

the carbon-fibre channel, the system could work without the Be pipe, simply with the cooling fluid flowing in the channel, and the BeO providing the necessary uniformity. The multichannel data bus cables (Be or Al on kapton) are embedded into the body of the carbon-fibre support structure (Fig. 2.10).

The cooling channel contains the mixture of vapour and condensed liquid. The amount of condensed liquid is controlled by the pressure of saturated vapour in the channel and can be kept very low (1–2 mm thick).

Cooling of the First Layer

In the first layer, composed of pixel detectors overlaid with the readout electronics, the heat will be produced uniformly with a density of $\sim$0.13 W/cm^2. Since the working temperature gradients for pixels are limited only by the requirements of alignment and mechanical stability, we consider gas cooling of this layer possible.

The cylinder gap (1 cm) between the first layer and the beam pipe can be used as a natural channel for the gas flow.

The temperature difference between the heated surface and the gas must be about 10–35 °C if air is used and 5–15 °C if He is used (estimated for an acceptable gas flow of 6–8 m/s). The temperature difference for the gas between input and output will be kept at 4–8 °C. The temperature of the first layer would be 18–26 °C. To simplify the system and minimize the material, we prefer an open one; the gas transport may be done under fairly high pressure, i.e. 1.5–2 bar, to diminish the volume of gas wastes.

We also investigate [33] use of a partial heat transfer from the heated surface to the cooled surface of the beam pipe by a moderate air flow. In this scheme the central section of the beam pipe would be cooled down to 1–2 °C.

Evaporative Cooling System

The temperature stability of the Si drift detectors (of the order of 0.1 °C) is one of the major reasons for the evaporative cooling choice. In addition, it was shown [33] that the use of one of the ozone-safe Freons as a coolant can optimize the total amount of material compared to other options. C_3F_7I is the most suitable Freon for ambient temperatures under 1 bar pressure in the system (the boiling temperature is 20–25 °C).

The minimum total amount of condensed coolant in the volume of the ITS can be estimated from the total waste of coolant fluid (0.1 kg/s) to be roughly 0.5–1.0 kg. These values were obtained for saturated vapour pressure 1 bar and a total heat drain of 10 kW.

Estimate of the Total Amount of Material

In the proposed configuration, the material will be distributed non-uniformly in each layer, being concentrated along the ribs. The assembly will be done so that the ribs in the different layers will not be collinear when seen from the vertex point.

The exact amount of material in each layer will be fixed only after the finalization of the design, but we give here the estimate of material for a realistic case, which has been calculated to provide enough mechanical precision and satisfy the cooling requirements.

The values, in X_0, averaged over a whole layer, are:
0.03% for the carbon-fibre ribs
0.15% for the coolant fluid.
0.03% for the BeO foil.
0.03% for the Be power bus.
0.03% for the kapton data bus.

The material in the tracker is about 0.27% of X_0 per layer in addition to the detector modules, which are on average 0.33%, giving a total of 3% of X_0 for the ITS with five layers.

Assembly and Monitoring

In order to get reliable positioning at the level of 10 μm and to decrease the misalignment errors for the individual Si wafers in the whole, 1 metre-long volume of the Inner Tracking System, we consider the overall assembly to be done layer by layer at an optically controlled work station.

This station is based on a laser-controlled, automated, movable (photoelectric) microscope that can be adjusted in two coordinates to the prescribed position, with the required accuracy, by a microdrive. Thus the negative feedback from the laser-controlled

traditional device is expected to give a simple and cost-effective method of controllable motion along the 1-metre base. This system will be analog to the laser interferometric comparators of national metrology centres that are used for precision length measurements [34].

Several additional alignment and monitoring systems are being studied, including capacitive pickups, optical systems and high-momentum tracks.

The temperature at specific points is monitored by thin-film planar sensors, made of a 2–5 μm Pt meander, directly spread over the Si plate, on an area of 2 x 2 mm^2. They can provide a 0.02–0.03 °C precision. The necessary number of thermosensors and their positioning are now under study.

The same system of temperature measurements can be used for the temperature-field mapping and the temperature control of the work station for the precise alignment of the tracking system.

2.2.5 Radiation Effects

Because of the open geometry of the experiment, we expect the primary particles produced in the interaction to be the major source of radiation damage to the tracking elements, albedo neutrons giving only a minor contribution. We estimate a yearly dose of 160 Gy for the innermost layer, including proton running (see 5.2).

In recent years, in view of very-high luminosity experiments at both LHC and SSC, a wealth of data have been collected on the radiation tolerance of silicon detectors and electronics [27, 35]. From these, it is clear that the above-mentioned radiation levels would not degrade the performance of the detectors, while standard CMOS electronics would not be adequate for prolonged operation. Several manufacturers offer at present full-custom VLSI production in rad-hard versions, at a cost which is not significantly higher than standard electronics, and these processes show negligible degradation of performance for the radiation levels of concern here. Therefore, we do not foresee the need for any specific development on this subject.

On general grounds, there are no reasons to expect significantly higher radiation sensitivity for Silicon Drift Detectors than for Strip Detectors. However, since no data are available on these devices, we plan in the coming year to test their radiation tolerance.

Finally, the ageing of MSGCs under radiation is caused by chemical reactions in the detector gas components, which result in the deposition of an insulating layer on the detector. Although the mechanism is not yet fully understood, experimental results indicate that the lifetime of MSGCs would be significantly more than 10 years of operation for our detector [9].

2.3 The Time Projection Chamber

The TPC will follow the construction concept of existing TPCs (e.g. PEP4, ALEPH, DELPHI).

The field cage consists out of two coaxial cylinders of 500 cm length, the inner one with a radius of R_{inner} = 100 cm, the outer one R_{outer} = 250 cm. The sensitive volume between the two cylinders is terminated on both sides by endcaps which consist of multiwire proportional chambers. An optional design of the readout modules based on the MSGC technology is also considered [36]. The TPC is divided into two half-detectors by a membrane at the center plane. This membrane is held on a highly negative potential and the readout chambers are near to ground. The field cage carries ring electrodes which are on an appropriate potential to guarantee a constant electric drift field parallel to the axis of the cylinder.

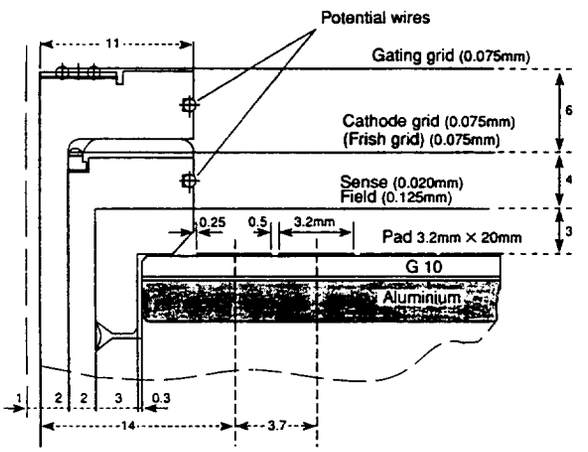

Figure 2.11: Cross-section of the LHC-TPC readout module

The readout modules consist in the usual way of different wire-planes: gating grid, Frisch grid (cathode), sense/field-wire plane and the pad-plane (Fig. 2.11). The dimensions are summarized in Table 2.4.

The pads will be arranged on circular rows, each pad with an approximate size of 3.2 mm in the azimuthal $r\varphi$ and 20 mm in the radial direction. The inter-pad distance in both direction is 0.5 mm. The final tune of the pad-size is still under study. It might well be that the pads will be shortened in size in the inner sectors and enlarged in the radial dimension in the outer sectors. We plan to use the pad read-

Inner radius (m)	1.0
Outer radius (m)	2.5
Drift length (m)	2 × 2.5
Gas volume (m^3)	48
Weight (kg)	5000
Inner sector size (mm^2)	≈750 × 680
Outer sector size (mm^2)	≈750 × 980
Number of sectors	≈66
Pad size (mm^2)	3.2 × 20
Pitch in $r \cdot \varphi$ (mm)	3.7
Number of pads	520 000
Pad-sense wire spacing (mm)	3
Sense wire spacing (mm)	4
Sense wire diameter (μm)	20
Field wire spacing (mm)	4
Field wire diameter (μm)	125
Diameter of other wires (μm)	75

Table 2.4: Dimensions of the TPC

out only as has been successfully done in the NA35-TPC [37].

2.3.1 Electronics

The high track density together with the requirement of good dE/dx and position resolution require a large number of electronic channels. The total number of pads is 520 000 if the padlength is taken as 2 cm and the pad plane is completely covered with pads. Given the extremely high channel density a VLSI electronics scheme with minimum power dissipation is mandatory. The distribution of on-chamber electronics and the repartition of analog and digital functions have to be carefully optimized in terms of mechanical and thermal loads on the TPC back planes and the minimization of secondary interactions at the endplates.

Based on the present development at LBL of a highly integrated front-end electronics chain for the NA49 and STAR experiments, the following configuration seems feasible: a 16-channel, low-noise, charge-sensitive preamplifier integrated with a shaping amplifier (shaping time around 180 ns) on the same chip. If extensive offline data correction or digital filtering procedures during data transfer are to be avoided, the high channel occupancy combined with the Landau fluctuations calls for very precise tail suppression in the shaper amplifier: in order to be compatible with the required dE/dx resolution, a suppression to 0.1% or better, referred to the maximum pulse height, is indeed required. In the same context, the high ionization load during the 80–100 μs open time (drift time) requires excellent baseline stability and insensitivity to load fluctuations. In an ongoing R&D project [36] analog front-end circuits that meet these requirements are under development.

In order to avoid space-charge limitations, the chamber gas gain should be kept at a few thousand (typically $5 \cdot 10^3$). This demands very low noise at the input stage, both in the high- and the low-frequency domain.

The preamp/shaper chip is followed by a 16-channel analog storage chip which is filled at a clock rate of 8–12 MHz. It is 1024 pixels per channel deep and has one analog-to-digital converter (ADC) per channel integrated on the same chip. An effective dynamic range of 10 bits is the preferred choice to cope with the large spread of input ionization as well as with the unfolding of close track topologies.

However, in order to facilitate the data reduction, 8-bit ADCs with bi-linear characteristic and high sensitivity in the first 4–5 bits and a smaller one for bits 6–8 are under consideration.

The digital information is then filtered, zero-suppressed and sent via an optical link to the data acquisition system. Owing to the high level of integration a layout of the TPC pad plane even with 1-cm-long pads in closely spaced pad rows may be feasible.

An integrated preamplifier chip and a 512 pixels per channel analog storage chip that is based on a switched capacity array (SCA) [22], developed at LBL, have been successfully tested on the NA35-TPC in the 1992 heavy-ion run.

In order to reduce the huge amount of data we will have to study more advanced data-reduction algorithms for the TPC, for instance the numeric filter MULAC by CNET [38]. Algorithms for data reduction are also discussed for the STAR-TPC at RHIC [7].

2.3.2 Choice of Gas

Nearly all existing TPCs use argon (Ar) with 9% or 10% methane (CH_4) as quenching gas. This gas mixture is relatively fast ($\geq$5 cm/μs) and the drift velocity has a flat maximum at a low drift field strength (120 V/cm). However, the electron diffusion for this mixture is large, which is a serious disadvantage. For the optimization of the proposed TPC the following gas properties are required:

- adjustable drift velocity of about 2.5–3 cm/μs as a compromise between the resolution in drift direction and drift time (i.e. readout time)
- low electron diffusion in longitudinal and transversal direction for good spatial and two-

track resolution

- low Z to reduce the space charge by primary ionization in the drift volume. In addition the drift velocity of ions is higher in low-Z gases. Preliminary measurements indicate a ratio of 1:2:4 for CH_4 mixed with Ar, Ne and He. This gives for example for Ne an integrated space charge which is smaller by a factor than in Ar.

In Fig. 2.12 we show the measurements of the drift velocity and electron diffusion for mixtures of Ar and Ne with CH_4 and CO_2. At the moment we propose to use a gas based on Ne, but further studies, concerning for example the sensitivity of the gas parameters to the temperature, are under way as part of the R&D project [36]. In this LoI we base our calculations on the properties of $Ne/CH_4/CO_2$ (88/10/2). In this case the amount of flammable gas (CH_4) in the detector is about 3 kg.

2.3.3 Expected Performance of the TPC

The estimates for the performances of the LHC-TPC are largely based on what has been measured at ALEPH and in the NA35-TPC. The LHC-TPC will have pad readout only and will be optimized for double-track resolution. Since the magnetic field is small, we neglect its influence. However, an appropriate calibration near the endcaps is necessary in order to correct for non-zero radial component in the L3 magnet.

In both the radial and the drift directions the single-electron diffusion of the gas, the pad crossing angle α, and in the drift direction the dip-angle λ of the tracks are the limiting factors. The pad crossing angle α depends on the particle momentum, while the distribution of $\tan\lambda$ is flat, which reflects the fact that a flat pseudorapidity distribution was assumed in the interval $0 < \eta < 1.0$.

Point Accuracy and Momentum Resolution

In our TPC simulation we have calculated the expected point accuracy and cluster width in transversal and longitudinal directions. For a track segment with the parameters given in Table 2.5 one obtains a point accuracy of $\sigma_{r\varphi} = 500$ μm, $\sigma_z = 900$ μm and a cluster width of $\sigma_{r\varphi} = 4$ mm and $\sigma_z = 5$ mm. It must be stressed that these numbers are dependent on the momentum and the position of the track in the TPC. They provide only an estimate for the average performance of the TPC. Given this accuracy the momentum resolution for a 500 MeV/c particle is expected to be $\Delta p/p = 1.3\%$.

In the existing TPCs only tracks more distant than 2–3 σ, where σ is the width of the cluster, can be

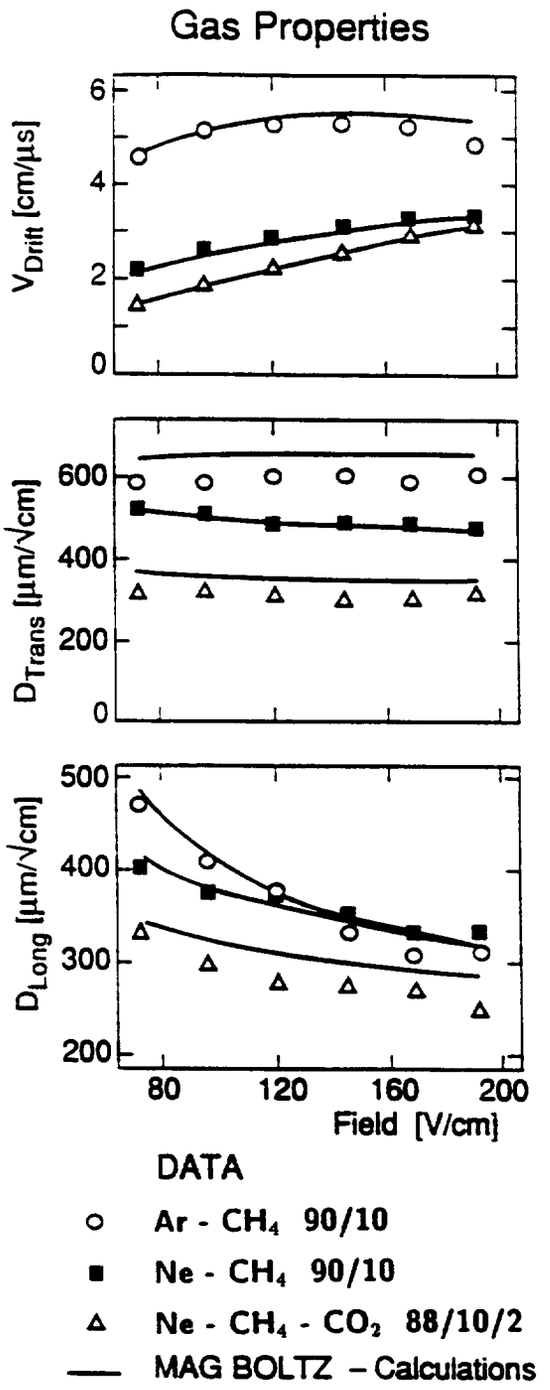

Figure 2.12: Drift velocity and electron diffusion for mixtures of Ar and Ne with CH_4 and CO_2

Drift length	125 cm
$\tan\alpha$	0.2
$\tan\lambda$	0.5
σ_{PRF}	2.6 mm
Gas	$Ne/CH_4/CO_2$
Diffusion, $\sigma_{trans} = \sigma_{long}$	300 $\mu m/\sqrt{cm}$
σ_{noise}	0.8 ADC counts

Table 2.5: Parameters used in the simulation to calculate the point accuracy of the TPC

resolved. Therefore for further calculations concerning track finding and fitting we assume 2.5 σ as the double-track resolution. However, NA35 is studying an unfolding algorithm which probably will allow to disentangle two tracks as close as one σ.

The error in determining the charge from the primary ionization per track by using this algorithm is at the 1% level, so, the dE/dx performance should not be strongly affected by this procedure.

dE/dx resolution

In the situation of almost straight tracks in the LHC-TPC the dE/dx performance can be judged from what has been observed in the NA35-TPC. In the NA35-TPC tracks were sampled in Ar/CH_4 (91/9) over a length of up to 2.40 m by a maximum of 60 samples, each sample 4 cm long (Fig. 2.13).

From these measurements we conclude that in the case of the LHC-TPC with 1.5 m-long-tracks and 75 samples, each sample 2 cm long, the resolution will be 5.5% for isolated tracks. For tracks in the densely populated region we estimate, based on NA35 experience, that the dE/dx resolution will be about 6.5%. For Ne mixtures [39] the same performance in dE/dx resolution has been measured as in Ar mixtures.

The main parameters and performance of the TPC are listed in Table 2.6.

2.3.4 Space-Charge Effects

The influence of ions from the primary ionization on the drift field has still to be carefully investigated. A first calculation has been done using a program developed for the STAR TPC at RHIC [40] after adjustment of the parameters for the LHC case, as shown in Table 2.7. The result is that a distortion of the tracks up to 1 mm can be expected (Fig. 2.14). Taking this into account only measurements starting at a radius of 120 cm were used for the momentum determination (see 4.1).

The distortions mentioned above are quite sizeable

Radiation lengths:	
Inner field cage	$0.012 \cdot X_0$
Outer field cage	$0.039 \cdot X_0$
Gas ($Ne/CH_4/CO_2$)	$0.005 \cdot X_0$
Gas properties:	
Drift velocity (cm/μs)	2.5
Longitudinal diffusion ($\mu m/\sqrt{cm}$)	300
Transversal diffusion ($\mu m/\sqrt{cm}$)	300
Drift field (V/cm·atm)	220
Pressure (atm)	1
Electronics:	
FWHM of shaped signal (ns)	180
Sampling of digitization (MHz)	8–12
Sampling depth (buckets)	min. 1024
Anode voltage (V)	1100–1200
Gas amplification	about 5000
Dynamic range (bit)	8–10
Performance:	
Pad response function (mm)	$\sigma_{PRF} = 2.6$
Space resolution:	
Azimuthal direction $r \cdot \varphi$ (μm)	500
Drift direction z (μm)	900
Cluster width:	
Azimuthal direction $r \cdot \varphi$ (mm)	4
Drift direction z (mm)	5
dE/dx resolution:	
Isolated tracks	5.5%
High density	6.5%

Table 2.6: Main parameters and performance of the TPC

R_{inner}	=	100 cm
R_{outer}	=	250 cm
L	=	250 cm
Gas	:	$Ne/CH_4/CO_2$
Drift velocity of ions	:	540 cm/s
Drift field	:	220 V/cm
$(dN/dy)_{ch}$ (central)	=	8000
Clearing time	:	0.4630 s
Event rate (minimum bias)	:	5.8 KHz
Solenoidal field	=	0.2 T

Table 2.7: Parameters for the calculation of distortions in the TPC

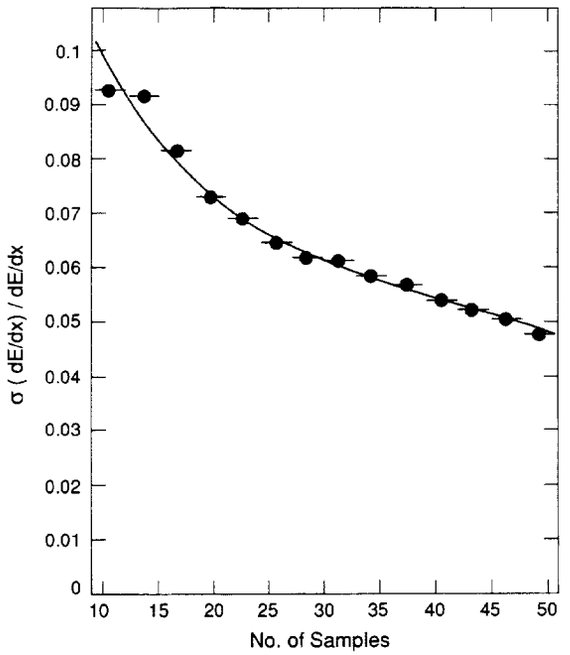

Figure 2.13: dE/dx resolution as a function of th number of samples in the NA35-TPC. Sample length 4 cm, gas Ar/CH_4 (91/9).

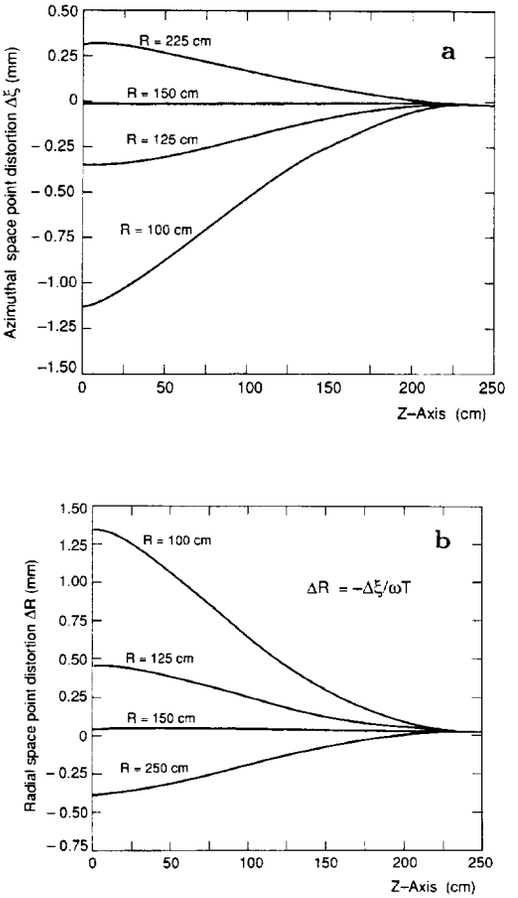

Figure 2.14: a) radial and b) azimuthal space point distortion due to positive-ion space-charge effect

and they limit the acceptable event rate for central events with $\langle dN/dy \rangle_{ch} = 8000$ to about 10 kHz. They can be reduced by the implementation of additional gating grids in the drift volume.

2.3.5 Laser System

For absolute position calibration and distortion corrections due to inhomogeneous electric and/or magnetic fields (or misalignment between them) a system based on a Nd:YAG laser with wavelength of 266 nm is foreseen.

The arrangement of the laser beams follows the design of the ALEPH experiment. It consists of six sets of laser beams at different φ angles with four beams per set at various Θ angles with an apparent origin at the interaction point. For each half of the chamber one such system is foreseen, 48 laser tracks altogether.

The laser system will also be used to monitor the drift velocity online.

2.4 Time of Flight

The preferred solution for the Time-of-Flight (TOF) measurement will be high-pressure parallel-plate spark counters (Pestov Detectors). Backup options are atmospheric-pressure parallel-plate chambers or scintillator counters in grid geometry with multi-anode photomultipliers.

2.4.1 Pestov Spark Counter

The Pestov Spark Counter (PSC) is a single-gap, gaseous detector working in the streamer mode. Prototype Pestov counters have been built and tested at Novosibirsk [41] and at SLAC [42]. A small-scale TOF system of Pestov Spark Counters has been used in an experiment at Novosibirsk [43]. A number of intrinsic properties [44, 45] of this counter make it an attractive choice for the LHC TOF system:

- an intrinsic time resolution up to 25 ps, dependent on operating conditions (voltage, gas mixture, gas pressure, etc.);
- an average discharge area of 0.5 mm^2 and a local recovery time of $\tau_{rec} \approx 10$ ms result in a counting rate capability better than 20 kHz/cm^2 (the typical minimum-bias count rate at LHC is ≈ 20 Hz/cm^2;
- a lifetime better than 10^9–10^{10} sparks/cm^2; i.e. more than 10^3–10^4 days of LHC running at 10^4 Hz minimum-bias interactions;

- the sensitive area of the counter is only 0.1 mm deep, i.e. no additional hits due to inclined tracks;
- the overall radiation length of a counter module is $\leq 8\%$ of X_0;
- the signal output is larger than 0.5 V, i.e. no preamplifier is necessary;
- the intrinsic efficiency is better than 96% (1.5% additional inefficiency comes from spacers between the plates);
- the material of the counter and its housing, (semiconductive) glass, aluminium and Plexiglas, is relatively inexpensive.

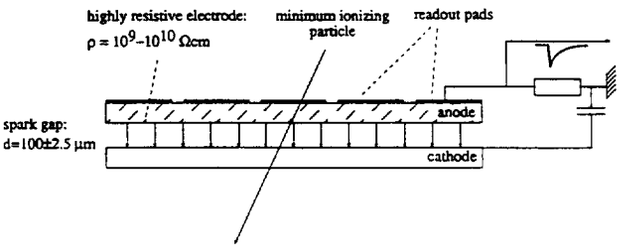

Figure 2.15: Schematic cross section of a parallel-plate spark counter showing the principle of operation

Working Principle

The essential feature of the Pestov Spark Counter is the use of a semiconductive anode which keeps the discharge local and enables a high count-rate capability. The spark, initiated in the gap after the passage of a charged particle, discharges a limited area of the semiconductive anode while the other area of the anode remains sensitive to other charged particles as sketched in Fig. 2.15.

The anode is made of resistive glass with $\rho = 6 \times 10^9\ \Omega$cm and the spark gap between the electrodes is 100 μm. The operating voltage is about 5 to 6 kV, i.e. an electric field of 50–60 kV/mm. The gap size chosen is a compromise between a few spark counter characteristics: the amplitude of the output signal, the efficiency and the time resolution. The counter operates at a pressure of 12 bars, which yields 4–5 primary electrons from a minimum-ionizing particle. The gas is argon with admixtures of 0.6% of divinyl, 2.5% of ethylene and 20% of isobutane for quenching. The mixture is non-explosive. The detectors are mounted in aluminium tubes with a wall thickness of $\approx$ 1 mm. The overall radiation length of one unit is less than 8%.

Barrel Structure

The geometrical layout presented here is based on a barrel with a radius of 3 m. At this distance, the particle density on the detector surface is $\approx$ 106 particle/m^2 (assuming dN/dy_{ch}=8000). The desired occupancy of less than 10% particles per cell defines a pixel size of less than 9.4 cm^2 at this distance. It is foreseen that a limited sector of the TOF barrel be moved out to a distance of 6 m, where it serves both as a high-resolution TOF system and as a charged-particle veto for the photon spectrometer. The area

	Pad readout
Time res. σ_t	40 ps $< \sigma_t <$ 100 ps
Position res. (σ)	$\approx$ 6 mm
Two-track res.	2.25 cm
Pixel size	4.0 × 2.25 cm^2
Occupancy	10%
Module size	4 × 100 cm^2
Modules	$\approx$ 4000
Channels	$\approx$ 169 000

Table 2.8: Main parameters of a Pestov counter based TOF system

of this TOF sector is about 25 m^2. The total number of modules and electronic channels including this extension is given in Table 2.8.

Figure 2.16 shows a detail of the arrangement of the Pestov counters in a TOF barrel. Both the modules and the tubes are staggered to have minimal dead space. Owing to the spatial extension of the pressure tube, the surface is not homogeneously closed for inclined tracks. The arrangement shown has a geometrical efficiency of $\approx$ 97% for track with momenta larger than 120 MeV/c ($\leq 45°$ inclination angle). It is, however, possible to reach to 100% geometrical efficiency on the expense of a larger number of detector modules [46]. Owing to the internal strength of the Al-tubes, the support structure itself can be relatively light; we estimate not more than 2 tons. Together with the weight of 5 tons of the detector, the total weight would be around 7 tons. The amount of inflammable gas (isobutane) in the detector depends on the barrel size and is, for a radius of 3 m, about

70 kg. The mixture with argon is non-explosive and can be premixed at the surface as required by CERN safety rules.

Readout

The discharge area is read out via pads evaporated onto the semiconductive electrode (see Fig. 2.15). The position resolution is given by the pad size. For the pad sizes under consideration (see Table 2.8), the time spread (σ_{spread}) due to geometry is below 40 ps, i.e. not a limiting factor with respect to the design value of $\leq$ 100 ps. Alternatively, the detector could be read out via strips. This option would yield, at the expense of a considerably higher number of readout channels (factor of 6), a better position and time resolution.

Table 2.8 gives the main parameters for the proposed readout scheme. For the calculation of the number of modules etc. a surplus of 20% of detector area is assumed due to staggering.

R&D Programme

As the tolerances of the detector are very subtle and the assembly requires clean-room conditions, a major part of the R&D effort specific to the Pestov Spark Counter is devoted to the development of design, production and assembly techniques that make the detector suited for mass production. Both the pad and strip readout will be investigated. As the number of electronic channels, $\leq$ 169 000 for the whole detector, is large, low-cost VLSI readout has to be developed.

2.4.2 Parallel-Plate Chambers

The Parallel-Plate Chamber (PPC) is a single-gap, gaseous detector with planar metal electrodes working in the avalanche mode [47]. The gap size between two planar metal electrodes is usually 1 mm and the uniform electric field is 5–6 kV/mm. This ensures avalanche multiplication at any point of the gas volume. The gas usually used is pure isobutane or a mixture based on isobutane at atmospheric pressure. The PPC consists of two optical-glass, ceramic or plastic plates covered with thin layers of metal to form the high- and low-voltage electrodes. The spacer has the shape of a frame glued to the plates to form a cell and to make it gas-tight. The high voltage is applied to the electrode through holes in the support surface, the preamplifier is connected in the same way to the opposite electrodes. The size of the working surface is 30× 30 mm^2 and the thickness about 3 mm. The properties of the counter are currently under investigation at CERN (RD5), at INFN (Florence) and by a group at ITEP (Moscow). First results show that the counter has:

- a time resolution of better than 250 ps;
- an efficiency $\geq$ 90%;
- high count-rate capability;
- stable operation;
- radiation length of a counter module 2–8% of X_0, depending on construction details.

A possible improvement both for efficiency and time resolution would be a double-gap PPC having a central electrode between two outer electrodes.

2.4.3 Scintillator Grid Counter

This option is based on long scintillator bars, arranged in a two-shell grid geometry (GRID counter) [48]. Each scintillator is connected through optical fibres or suitable light pipes from both ends to two channels of a multi-channel photomultiplier tube (MCPMT) with fine-mesh dynodes. The tube under consideration allows operation in a magnetic field, which is excluded with conventional tubes. This type of PMT is currently the subject of intensive R&D [49, 50].

The GRID counter offers:

- the good characteristics of plastic scintillation counters regarding count-rate capability, light yield, long lifetime and no delicate handling before and during measurements;
- time resolution better than 100 ps, depending on the primary light yield and the transmission properties of the optical coupling [50, 51, 52, 53]. In addition, 64% of all particles are detected independently in both planes yielding an additional gain in time resolution;
- position resolution better than 1 cm along the slats and two-track resolution better than 2 cm, due to the slat width.

This scintillator-based option allows more than one scintillator to be connected to the same channel of the MCPMTs by means of optical multiplexing made with light pipes or fibres of different lengths [54]. This possibility can, under certain circumstances, give substantial cost savings.

The requirement that not more than 10% of particles be lost defines the slat size to be length × width × depth = 18 ×2 × 0.5 cm^3 yielding altogether $\approx$ 63 000 slats read out at both ends,

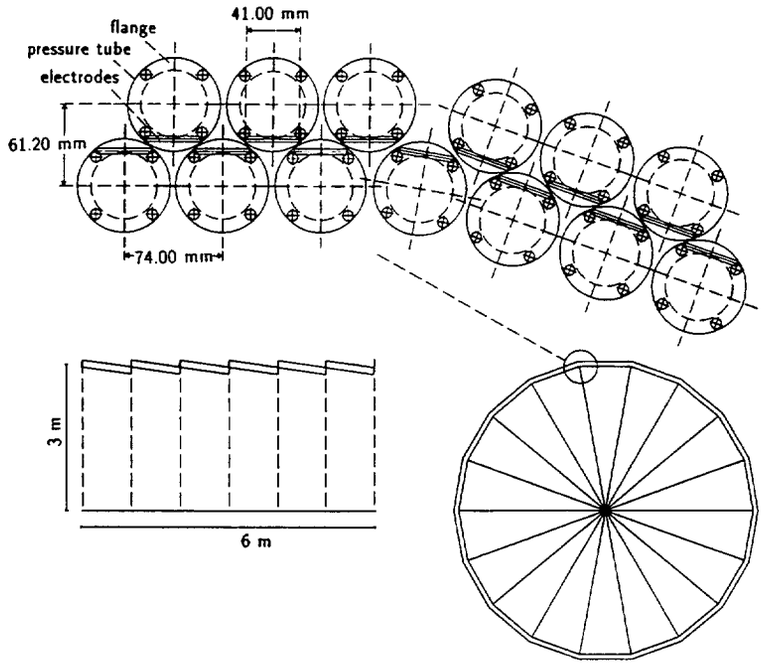

Figure 2.16: Enlarged view of a section of the TOF barrel showing the geometrical arrangement of several pressure tubes with Pestov counters inside

thus yielding 126 000 electronic channels[2]. The barrel is composed of blankets of 18×18 cm^2, consisting of two planes of orthogonally arranged slats. The major part of R&D for this option has to concentrate on the optimization of the optical coupling from the scintillator slats to the MCPMT pixels as well as on the readout electronics.

2.4.4 Readout Electronics

For the large number of readout channels conventional electronics (CAMAC, FastBus) is too expensive for the foreseen TOF systems. The development of front-end VLSI readout is thus mandatory to reduce the cost to an acceptable level. A per-channel price below 10 CHF is the target. As the pulse shape characteristics of all TOF detector systems are similar (fast risetime of below 0.5 ns, max. pulse below 1 V, pulse duration several ns) the VLSI development can and must be pursued independent of the final choice of detector system. The readout must be mounted directly on the detector. Analog cable delays are excluded due to cost, space and weight reasons. A possible solution could include the use of a high-precision ramp generator [55]. The arrival time of a particle is obtained by measuring the voltage reached by a ramp which is started by the particle and stopped by a pulse of a freely running clock. Alternatively, the digital TDC technique [56] could be employed. The time T_0 of the event is obtained in the same way from a T_0 counter or from the ensemble of the forward dN/dy counters (see 2.7.1). The requirements on the integrated electronics are:

- adjustable leading-edge discriminators;
- time reference from high-precision oscillator;
- internal time resolution $\approx$ 25 ps;
- a time range of $\approx$ 40 ns;
- time-to-voltage conversion with fast clear/reset;
- charge-to-voltage conversion with fast clear/reset;
- 10-bit analog-to-digital conversion;
- integration of at least four channels on a chip;
- crosstalk below 2%;
- local intelligence (e.g. zero-suppression);
- parallel-to-serial conversion;
- readout speed below 1 ms.

R&D Programme

We have started ad R&D programme to show the feasibility of the envisaged readout scheme and of the

[2] We can use 90 mm^2 channel MCPMTs, Hamamatsu mod. R4549-01.

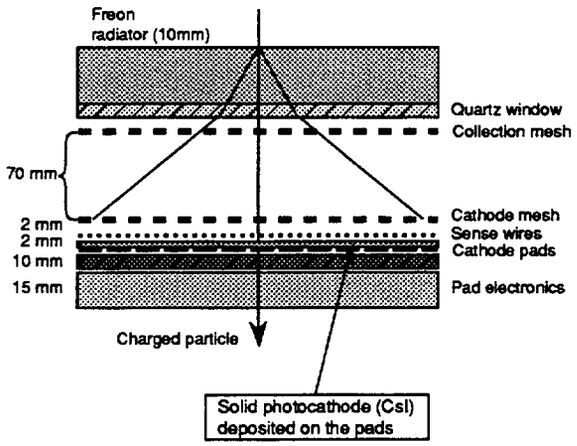

Figure 2.17: Schematic view of the CsI proximity-focusing RICH

integration of several channels. Crosstalk problems might be a serious problem due to the fast rise time of the signals. First prototypes of the TOF readout are being developed employing SMD technology. Digital TDCs are currently under study at the University of Paris. These devices have been used for the DELPHI experiment [56] for much lower time-resolution requirements.

2.5 The Ring Imaging Cherenkov Detector

The proposed Ring Imaging Cherenkov (RICH) detector will be of the proximity-focusing type with a liquid-Freon radiator and a UV detector based on the use of a low-gain Multiwire Proportional Chamber (MWPC) with a pad readout for two-dimensional determination of the coordinates of the positions of the ionizing particles and of the Cherenkov photons [57, 58]. The conversion of UV photons into electrons is achieved using a solid photocathode consisting of a thin layer of CsI evaporated onto the pad plane.The schematic of the proposed RICH is shown in Fig. 2.17

In the momentum range (0.8–2.5 GeV/c) covered energy loss and multiple-scattering effects in the preceeding detectors play a minor role.

2.5.1 The UV Detector

The operation of a RICH counter is dictated primarily by the performance of the UV detector. The present project uses the existing experience in the field of fast RICH detectors with MWPCs coupled to the R&D on solid photocathodes [57, 58].

The photoelectrons created by the Cherenkov photons are detected by a MWPC equipped with a pad readout. The MWPC consists of a cathode mesh, or wires (for larger photon transparency), a wire anode plane with 4-mm spacing, and of a pad readout cathode plane with pads 8 $\times$ 8 mm^2. The size of the pads relative to the chamber gap is chosen to allow sufficient coupling of the anode to the cathode, and thus a high single-electron detection efficiency with a satisfactory spatial precision. The total material thickness of the MWPC including the readout electronics is 0.03 X_0. Recent developments in pad readout electronics allow to conceive a reduction of that thickness by 50% [59]. The main features of the detector may be summarized as follows:

- the thickness of the MWPC ($\approx$ 4 mm) allows positive identification of charged-particle impact on the detector (a clear discrimination against photon clusters is possible), at the same time keeping it small enough so that the operation of the detector in a high-density environment with inclined tracks is possible without deterioration of the localization characteristics for the track impact point.

- the photoconversion is achieved in a single layer thus eliminating an important source of parallax error present in detectors where a photosensitive gas is used instead of a solid photocathode.

- the use of a solid photocathode allows for a substantial saving in terms of material thickness. The gap between the detector and the radiator may be filled with the same gas as the detector thus eliminating the need for a quartz window, considerably reducing the cost, and making operation easier than that of a RICH operating with photosensitive vapours at high temperature.

- the analog multiplexing readout electronics, and the intrinsic characteristics of a MWPC of the present design allow operation at interaction rates 10^4–10^5 Hz with acquisition speeds of 10^2 Hz.

2.5.2 Position Determination and Two-Track Resolution

The precision on the coordinates of the impact of the charged particles has been measured to be better than 600 μm in the present prototype (8 $\times$ 8 mm^2 and cathode-wire distance 2 mm) using centroid determination. The two-track resolution has been determined by simulations to be better than 2 mm.

This allows identification of strong rapidity fluctuations since the mean distance between two hits at 4.5 m distance is 50 times larger.

2.5.3 Radiator

We envisage the use of a liquid-Freon radiator. The liquid-Freon characteristics (chromatic aberation, index of refraction) are adequate for the range of energies under study. The only drawback is the necessity to contain it with a UV transparent window and to purify it. In our case the radiator will have a thickness of 10–16 mm contained by 4 mm of quartz. The quartz window will be reinforced every 20 cm by cylindrical spacers connected to the back wall of the radiator.

2.5.4 Performance of the Detector

The performance of the detector in a high-density environment depends essentially on two factors:

1. The number of photons recorded per event, which depends on the quantum efficiency of the photocathode, the beta value of the particle, and on the radiator thickness. The simulations presented here were done under the assumption that the mean number of detected photons at $\beta = 1$ is 15. This value has been achieved with a MWPC detector using TMAE vapour [60] for a 10-mm Freon radiator. The results with the CsI photocathode [58] would require a radiator of 15–16 mm but the best values reported in the literature for CsI would allow a 10 mm radiator.

2. The ability to distinguish the clusters from charged particles from those belonging to photons. In the present prototype a clear distinction between these two types of clusters is possible. The mean cluster size for a minimum-ionizing particle is four pads while the mean cluster size for photon clusters is 1.2 pads. The larger size of particle clusters allows for a very good spatial precision on the impact point of the particle on the radiator, which is of paramount importance for the tracking precision as well as for the pattern reconstruction. The precision on the photon centroid position is less demanding for as long as it is lower than errors due to chromatic aberation and geometrical effects (proximity gap and radiator thickness).

Considerable experience with such a type of detector already exists:

- the construction details of a 50×50 cm^2 MWPC connected to a liquid-Freon radiator of the same size has been successfully solved and tested in a prototype using TMAE vapour and the existing AMPLEX chip under the conditions of nucleus–nucleus collisions with densities of $\approx 25/\mathrm{m}^2$ [60].

- the first results obtained on a 10×10 cm^2 prototype with a solid photocathode [61] demonstrated the technical feasibility of the proposed detector. Specifically, the problems of evaporation of CsI layers onto pads have been successfully solved without the use of expensive and time-consuming masking techniques. A 30×30 cm^2 prototype has been successfully tested, and a station allowing evaporation of CsI on areas 50×80 cm^2 has been built.

- a first-generation RICH detector has been tested in nucleus–nucleus collisions in the NA35 experiment, and the first results indicate the identification power of the method even in a high-density environment [62] to be satisfactory.

- the first prototype of the CsI RICH achieved a $3\,\sigma\ \pi$ / K separation at 2 GeV/c, but the many technological improvements foreseen should improve this figure.

2.5.5 Detector Layout

The detector layout is governed by the need to optimize the performance in the azimuthal angle as well as in the angle of emission. The main constraints are the following: the best localization accuracy is achieved along the sense wire so that the wires have to be positioned perpendicular to the beam direction, and the best Cherenkov angle resolution is achieved for track incidence normal to the radiator, resulting in the need to tilt the planes as we move along the barrel. For construction reasons the size of the chamber module has been set to 220×110 cm^2. The tilting, to be decided subsequently with simulations, will require trapezoidal shapes not discussed here, but these considerations are not expected to influence significantly the cost or construction. The detector will consist of 100 modules of 2.3 m^2, with a total of 3 200 000 pads. The active area will then be $75-80\%$ of the total area covered by the detector.

2.5.6 Electronics

To read out the 16 000 pad channels per m^2 ($\approx 10\%$ pad occupancy), a highly multiplexed (MPX) analog scheme is proposed, based on a VLSI front-end part implemented on the back of the pad electrode. An analog scheme was chosen for two reasons. First,

the pulse-height information provides a way to distinguish single-electron (SE) from particle signals, an essential help in pattern recognition. Second, using pedestal measurements, threshold values can be set for each channel thus allowing optimal detection of SE signals at every pad, relaxing the specifications for the gain variations.

The main features of the front-end electronics are:

- The preamplifier integrating time is set to 400 ns, which is compatible with the expected readout time, thus allowing for optimum signal/noise ratio and setting a built-in delay for a trigger decision.
- A filtering stage, specific to the hyperbolic time dependence of the MWPC current signal is inserted to ensure correct baseline recovery performance.
- The MPX block and associated control signals should operate at rate of 5 MHz.

The readout is based on a serial/parallel multiplexing scheme. The serial depth will range between 350 and 500 channels, depending on the modularity and front-end implementation constraints. That implies about 100 μs of MPX time for full readout. The basic blocks of a readout element will consist of three parts, namely an 8-bit FADC, an arithmetic unit allowing for threshold comparison and pedestal subtraction, and a storage of useful data (PH and addresses to be transferred to the DAQ system). These readout modules are to be implemented as ASIC-VLSI chips on the chamber module.

Multiplexing the full detector will lead to $\approx$ 8000 readout elements. This number may be reduced by a factor of five, adopting a sparse data scan since the expected occupancy is 10%. Such a system requires every front-end chip to deliver a fast flag signal indicating that at least one channel was active on the chip. This flag can be generated in the first microseconds preceding the long MPX operation in order not to hinder the storage of the small analog signals. If the MPX time has to be reduced, a balance can be found between the number of readout elements and a smaller MPX depth. Additional local intelligence can be envisaged, such as cluster counting, providing fast information on particle multiplicity and density.

All the fast RICH tests referred to in the text were performed with an analog MPX scheme based on an existing front-end chip (AMPLEX) and non-integrated readout elements. Developments to adapt such a chip to MWPC operation (filter block), and to improve its signal to noise ratio and MPX rate are under way. Integrated readout elements, and sparse readout will necessitate new ASIC-VLSI development work. Efforts along these lines are underway at several institutions (e.g. RD26 [58], Lund [59], and RAL [63]).

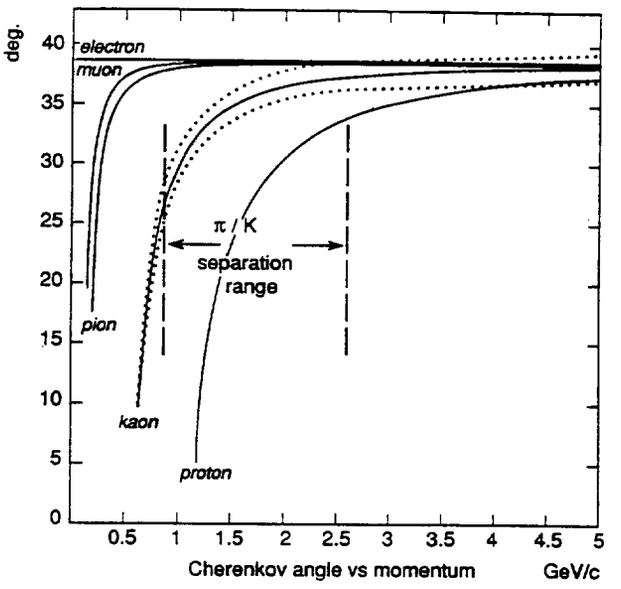

Figure 2.18: Variation of the Cherenkov angle with momentum for different types of particles(full lines). The dotted lines around the kaon curve show the 3 σ spread in the reconstruction.

2.5.7 Particle Identification in a High-Multiplicity Environment

The density of particles at the position of the RICH is estimated to be $\approx 50/\mathrm{m}^2$ with $\mathrm{d}N_{ch}/\mathrm{dy} = 8000$.

As a test of the efficiency of particle identification we have adopted the following procedure:

We have developed a simulation program that reproduces a realistic pad readout detector taking into account the pad size and the wire distances in the existing prototype. The results of the simulations were matched to the experimental results [57] allowing one to determine the precision of the centroids for the 'photon clusters', and for the impact of the charged particles. The results show that the centroid position for the ionizing particles may be determined with a precision of 600 μm along the anode wires and 1.2 mm in the direction perpendicular to the wire. For 'photon clusters' the precision on the centroid determination is approximately equal in both directions since the average number of pads hit per photon is only $\approx$ 1.2.

Using these parameters, pattern recognition and

particle identification was applied to spectra obtained from the GEANT simulation. The resulting 3 σ spread for the kaons as a function of momentum is shown in Fig. 2.18. The 3 σ limit of identification is $\approx$ 2.6 GeV/c at the actual particle density.

The number of identified particles is a function of pattern recognition criteria. One can improve the identification range at the expense of the detection efficiency by using only tracks with a number of photons larger than a given threshold (for instance, larger than the average number). In our analysis with no cuts applied to the number of photons the portion of pions wrongly identified as kaons is $\approx$ 0.5% in the region below 2 GeV/c.

2.6 The Photon Spectrometer (PHOS)

The measurement of prompt photons is a prime goal of heavy ion experimentation since it is one among very few signals which can provide direct information on the partonic, early phases of the interaction. Prompt photons are a small fraction of the meson decay photons, which must be accurately known before the former can be determined.

This section summarizes the principles which determine the geometry, structure, and the readout of the Photon Spectrometer. It builds on previous experience with WA80, WA83, WA93, and NA12, and on Monte Carlo simulations. The goal is to measure all photons over a solid angle large enough so that both π^0's and η's can be reconstructed (from 2γ decays) and their cross-section determined above some minimal p_t which depends on the size of the detector. The prompt photon cross-section is then obtained by subtraction of the decay photons from the measured γ spectrum.

This requires little overlap of photon showers, i.e. high granularity, and good energy and spatial resolution, since the background under the mass peaks is proportional to their width.

The reliable measurement of single photons requires cell sizes not exceeding one Molière radius R_M (one long cell of one R_M^2 section hit by a γ in its centre absorbs 80% of its energy); and a pixel occupancy not exceeding 3% (there should be no more than one photon or hadron every 33 cells). At this occupancy, the gamma reconstruction efficiency should be measurable to an accuracy of $\approx$ 4% [64].

2.6.1 The Detector

In the following, we discuss a detector made of 50000 elements of 22 mm width (front) and 20 X_0 length, located at 6 m vertically beneath the interaction region. It will be 6.5 m long ($0.5 < \eta < 0.5$) and 3.8 m wide ($\Delta\phi = 2\pi/10$) and cover a total surface of $\approx$ 25 m^2. The large distance and the small cell size are required to keep the occupancy below 3% (see 4.5). Regarding the detector material, we rely largely on recent detector developments [65]. In Table 2.9 (partly based on [3]), we list the new detector materials which are contemplated, with their radiation length, Molière radius, energy resolution parameters (the ones in parenthesis are estimated rather than measured), light output (for Si photodiode readout), and relative cost per unit solid angle.

PHOS	X_0 mm	R_M mm	a %	c %	PhEl MeV	Rel. cost
$PbWO_4$	9	22	<3	<1	100	1
BGO	11	27	1.6	.5	1000	5
CeF_3	17	26	(1)	(.5)	300	4
PbF_2	9	18	(4)	(1)	2	
W/Sc	18	25	7	1.5	5	.6

Table 2.9: Detector materials and their properties

The energy resolution parameters a (sampling and light output), b (readout noise; see following section), c (readout inhomogeneity and calibration error) are defined as follows (for E in GeV):

$$\sigma_E/E = (a/\sqrt{E} \oplus b/E \oplus c)\ \% \qquad (2.1)$$

$PbWO_4$ is a newcomer among the crystals for calorimetry, which has undergone two years of extensive R&D studies carried forth by the Collaboration, including the development of mass production technology. We consider it as a promising candidate for our detector because it is very dense, it scintillates and it is rather easy to grow, to machine and to handle. Its index of refraction is 2.2. The first crystals of calorimeter size (16 X_0) were made in 1992, and tested at the 70 GeV IHEP accelerator in February 1993. The measured energy resolution was σ_E / E = 1% for 25 GeV electrons in a single PHOS-type cell.

Within a year we expect to have gathered enough experience to be able to decide on its suitability for our calorimeter.

We have further listed BGO, since it is conceivable to reuse the L3 detector (5 m^2, 10000 cells) which covers 20% of the envisaged detector size and has the right properties and an unmatched resolution. It may have to be reconfigured to be used at 6 m distance.

As back-up solutions we consider PbF_2 and the much more expensive CeF_3, both with an ongoing R&D programme [66]. Finally, we quote the sand-

wich structure of tungsten and scintillator plates with thin sidewise WLS plates. The scintillator plates must be at least 1.5 mm thick to provide reasonable light output uniformity; the required Molière radius imposes tungsten plates of at least 0.5 mm. This leads to an energy resolution worse than for the crystals, and would clearly increase the error on prompt photon production (see 4.5). A possible alternative solution based on liquid kripton has been proposed [67].

A charged particle veto will be supplied by the particle identification system, or if needed, by a pad MWPC in front of the PHOS.

2.6.2 Readout

Since the detector is to be operated inside a magnetic field of 0.2 T, the best candidate readout photodetector is the photodiode with amplifier of the kind successfully used in L3 [68], where the readout noise is b = 1 MeV per BGO cell (see Eq. 1). With a similar large integration time, $PbWO_4$ light output and optimized photodiode, we expect a readout noise of b = 10 MeV.

Corresponding figures for backup solutions are 1 MeV for BGO and 5 MeV for CeF_3. The other alternatives would require a noise-free and more expensive readout.

2.6.3 Calibration and Monitoring

To keep the good intrinsic resolution of a crystal detector, accurate calibration and monitoring is required. However, for the energies of interest here (< 10 GeV), the needed absolute precision is less demanding. The whole calorimeter will be calibrated in a test beam prior to installation. A laser monitoring system will be implemented to preserve the absolute calibration when the detectors are moved form the test area to the experimental position. The same system will be used to monitor gain variations during the runs.

2.7 The Large-Rapidity Detectors

2.7.1 The Forward Multiplicity Counters

The forward multiplicity detectors will cover the rapidity interval outside the central acceptance to measure $dN_{ch}/d\eta$ over most of the phase space. Several options are possible, namely:

- Microchannel Plates (MCP) [69].
- Silicon Pad Detectors [70, 71].
- Microstrip Gas Counters (see 2.2.3).
- Multistep Avalanche Chambers [72].

Hereafter we consider a multiplicity detector based on MCPs: the design concept would be similar for other options. Since in the central region we foresee a large-diameter beam pipe for other reasons (see 4.1), the multiplicity array could be installed inside the beam pipe thus being very compact and avoiding secondary interactions in front. MCPs are well suited for this purpose, since they have to be installed in vacuum and allow for baking at up to 200–300 degrees. First discussions with the machine experts show that such an installation is feasible if the inner aperture of the MPC has a diameter of at least 5 cm . If needed, the MCP array could be placed in a secondary vacuum separated by a thin foil from the machine.

In this configuration, we do not plan to count individual particles. The multiplicity array could be segmented into rings, e.g. of $\Delta\eta = 0.1$ and $\Delta\phi = 30°$, containing of the order of 70 charged particles for central events. The multiplicity will be measured by summing the total charge accumulated by the segmented pad–anode located behind the MCP. This method has been used previously in heavy–ion experiments with silicon pad counters [71] and provides sufficient accuracy if the error introduced by analog summing is comparable or below the Poisson fluctuation in the number of particles. This error will depend on the r.m.s. of the single-particle response function, and we are testing at the moment if two– or three–stage MCPs are adequate for our purpose.

The region from 1.4 to 2 in pseudorapidity will be covered by a barrel close to the interaction point, the more forward regions will be covered by a serie of identical segmented disks. The distance from the interaction point will define the rapidity range up to $\eta = 4.8$. Further disks could be installed depending on the final design of the beam pipe. A possible arrangement is summarised in Table 2.10.

The timing properties of MCPs are very good, i.e. 1 ns signal duration and up to 25 ps timing resolution [73]. Thus the MCP-based detector can be used in the first-level trigger (see 3.1.2); in addition, it will locate the event vertex to ~1 cm and, by averaging over many channels, provide the T_0 time for the TOF counters (see 2.4).

The background of QED electrons (see 5.2) close to the beam has been estimated and its impact on the performance is being studied.

The long-term stability of the MCP depends on the total accumulated charge at the output of the MCP assembly [73]. The output gain decreases typically by 50% for a charge of 1 Coulomb/cm^2 [74]. For a two–stage MCP with a total gain of 10^6 this corresponds to 10^{13} incident particles/cm^2. The gain decrease

Name	Rapidity coverage	Location z (cm)	R_i (cm)	R_o (cm)
Barrel–1	1.4–2	11.3–21.8	6	-
Disk–2	2–2.9	22.9	2.5	6.3
Disk–3	2.9–3.8	57.6	2.5	6.3
Disk–4	3.8–4.8	145	2.5	6.3

Table 2.10: Geometrical parameters of the MCP-based multiplicity detectors

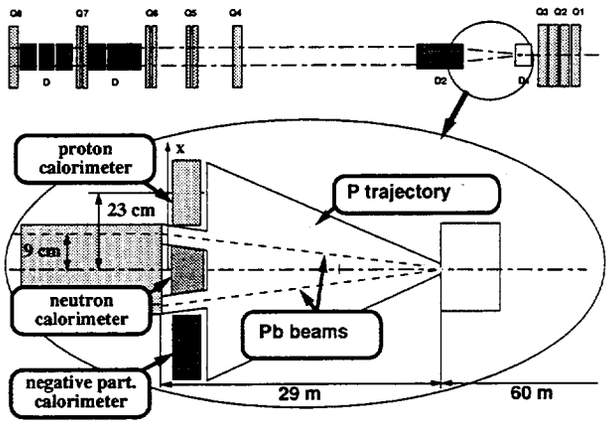

Figure 2.19: ZDC detectors layout

can be compensated to some extent by increasing the voltage [73, 74], thus guaranteeing a few years of operation even for the most exposed elements. MCPs are expected to survive very high radiation doses in passive mode, i.e. with High Voltage off. They can therefore be left in place also during high-luminosity proton operation of the machine.

2.7.2 The Zero-Degree Calorimeters

The impact parameter of the collision can be determined by measuring the total energy of non-interacting nucleons and/or nuclear fragments with Zero-Degree Calorimeters.

Owing to their different Z/A values, it is possible to separate in space the neutron and proton spectators and the beam particles (Z/A $\simeq$ 0.4) by means of the LHC dipole D1 (Fig. 2.19). Therefore, we intned to detect the neutron and proton spectators in two distinct calorimeters.

A third calorimeter will be added to detect negative particles. The difference in yield between positive and negative particles would help to select the spectator protons.

Two identical sets of such calorimeters will be placed on both sides of the interaction point to improve the resolution on the impact parameter and to better determine the collision geometry. The neutron and the proton calorimeters are located about 29 m downstream of the magnet D1. Here the spectator neutrons are 9 cm away from each of the circulating beams and 23 cm from the spectator protons. These distances are sufficient to allow the detection without perturbing the circulating beams. On the other hand nuclear fragments, having a charge-to-mass ratio close to the one of the beam will remain inside the beam pipe.

Detector description and performance

The proposed calorimeters are of the 'spaghetti' type with quartz fibres as active material instead of the conventional scintillating fibres. The use of quartz fibres is imposed by their radiation hardness ($\geq 10^7$ Gy), since the calorimeters will have to work in a high radiation environment. A first estimation, based on a GEANT simulation, shows that the maximum dose deposited in the neutron calorimeter is of the order of 10^4 Gy/running day.

The size is determined by the arrangement of the beam pipes at D2 (see Fig.2.19). The small horizontal size of the neutron calorimeters imposes the choice of tungsten as showering material in order to minimize the shower loss. A GEANT simulation shows that a size of 13 x 13 x 100 cm^3 for the neutron calorimeter provides a 90% shower containment for 3.15-TeV incident nucleons (the longitudinal dimension corresponds to about 10 interaction length). A better containment can be obtained by increasing the vertical dimensions of the calorimeters. Since the geometrical constraints are less severe for proton and negative-particle calorimeters a size of 22 x 22 x 100 cm^3, can be envisaged. This allows a 98% shower containment if the showering material is tungsten. The possibility of using lead, which would reduce the cost, is under study. With these dimensions the neutron and proton calorimeter cover the pseudorapidity regions $\eta \geq 7.9$ and $\eta \geq 7.4$ respectively.

The calorimeters consist of four identical blocks. Each one is 25 cm thick and is filled with about 6000 quartz fibres of 1 mm diameter, arranged in planes forming an angle of 45° with the calorimeter axis in order to optimize the Cherenkov light collection (see Fig. 2.20).

In each block four photomultipliers are connected to the quartz fibres in such a way that each photomultiplier collects the light from 1500 fibres equally spaced in the tungsten volume, as shown in Fig. 2.20. The connection between the photomultipliers and the

quartz fibres is made through a plastic fibre, to allow larger flexibility. In this way, considering respectively one, two, three or four PMs per block, different quartz/tungsten volume ratios can be obtained, ranging from 1/20 to 1/5. The simulation predicts the resolution of the neutron calorimeter to be about 10% for 3.15-TeV incident particles, almost independent on the quartz/tungsten volumes ratio. Therefore a possible breakdown of up to two photomultipliers in each block during a long period of data taking should not overly affect the detector performance and its operation. This fault tolerance is important since the detectors are placed in the tunnel and will not be easily accessible.

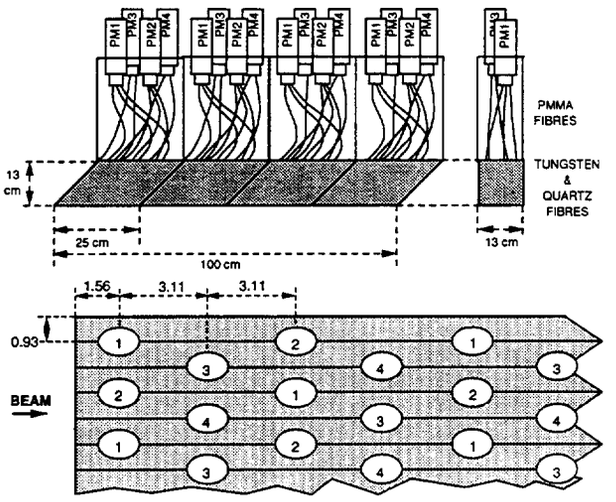

Figure 2.20: a) neutron calorimeter structure and b) horizontal cut of a piece of a block, showing the equally spaced quartz fibers; the number in each fibers refers to the PM to which the fiber itself is connected

This kind of calorimeter will be used in the NA50 experiment. We have recently built a prototype [75] with lead as showering material, having the quartz-to-lead volume ratio ranging from 1/10 to 1/40. Its resolution for 200 GeV/A sulphur incident ions has been in good agreement with simulation results.

We are considering to add a depth segmentation to measure separately electromagnetic and hadronic energy in order to separate photons, in particular at 0 degree in front of the neutron calorimeter (see 4.6.1).

2.8 Detectors under Study

In addition to the baseline design described above, we are evaluating a number of additional detector elements. Our study is based on the availability of the L3 magnet and cave. Their physics goals, performance and construction will be described in detail in an addendum, if and when the collaboration feels confident about their feasibility. We outline here briefly the current status.

2.8.1 The Barrel Calorimeter (BARC)

We are considering a barrel electromagnetic calorimeter, surrounding the high-resolution photon spectrometer (PHOS), with rapidity range $|\eta| < 0.9$ and complete azimuthal coverage.

The BARC would be used for measuring the local density of neutral transverse energy and its correlation to the charged particles emitted in the same solid angle. This calorimeter could be also used in conjunction with an elaborate trigger system for rare events, e.g. high-mass di-electrons and high-p_t π^0's.

Finally, the performance specifications would be fully adequate to study $\gamma\gamma$ collisions (see 1.1.8).

The hardware solution under evaluation is a sandwich structure made of alternating layers of 1 mm of Pb and 4 mm of scintillator, the latter read out by thin (0.4 mm) wavelength shifter side plates. The length is 20 X_0 (56 cm), the cell size is 10×10 cm^2 (R_M = 35 mm) and the total surface is ≈ 400 m^2. The energy resolution could be as good as $\sigma_E/E \approx 5\%/\sqrt{E}$.

2.8.2 The End-cap Calorimeters

The electromagnetic calorimeters covering the end-cap regions would measure the photon multiplicity in pre-shower segment and the total electromagnetic energy with moderate resolution ($10\%/\sqrt{E}$). The granularity in the pre–shower region should be adequate for photon multiplicity measurement and, at larger depths, should be of the order of a Molière radius to deduce the mean electromagnetic E_t per particle.

The hardware solutions under study is a sampling calorimeter based on liquid argon with the following design goals:

- Two layers of high granularity with good efficiency on photon counting and good hadron rejection.
- Moderate resolution ($\approx$ $10\%/\sqrt{E}$) obtainable with $\approx$ 25 depth samplings of 1 X_0 each.

We consider two calorimeters with full azimuth coverage on each side of the interaction region:

- the Near End Cap calorimeter (NEC) placed inside the magnet at 5.5 m from the interaction point covering η from 1 to 2.5
- the Far End Cap calorimeter (FEC) placed outside the magnet at a suitable distance(18 m to 30 m) covering η from 2.5 to 4.5.

A modular structure is envisaged since hermeticity is not required. The cryostat design has to minimize the total thickness in front of the first sampling layer ($< 1\,X_0$). For the complete calorimeter with both left and right arms of NEC and FEC the total cryostat volume will be ≈ 120 m^3.

The read out will be done in a non–projective geometry using pads of dimensions ≈ 1 cm^2 in the pre–shower region and ≈ 30 cm^2 at larger depth. The total number of readout channels is expected to be around 3 million.

Pad readout with VLSI electronics and chip-on-board technology is being investigated. A very cheap chip-on-board technology has already been developed for WA98 experiment [59]. We aim to place the electronics in LAr but intensive R&D is required before the design is finalized.

References

[1] H.J. Specht, Large Hadron Collider Workshop, Aachen, October 1990, ECFA 90-133, CERN 90-10, p.1236.

[2] Expression of Interest presented by J. Schukraft to the General Meeting on LHC Physics and Detectors, Evian-les-Bains, March 1992.

[3] T. Aziz et al., L3P Letter of Intent, CERN LHCC/92-5 and LHCC/92-14.

[4] M. Chen, L3H - CERN/LHCC 93-15.

[5] W. Flegel, Internal Note ALICE/MAG-93/13.

[6] A. Dudragne et al., Nucl. Instr. and Meth. A324 (1993) 93.

[7] STAR Conceptual Design Report, LBL-PUB-5347, 1992.

[8] G. Batignani et al., IEEE Trans. Nucl. Science, 36 (1989) 40.

[9] F. Angelini et al, Internal Report of Università degli Studi di Pisa, INFN PI/AE 92/01.

[10] M. Campbell et al., Nucl. Instr. and Meth. A290 (1990) 149.

[11] W. Beusch et al., CERN/DRDC 90-81 P22, RD-19.

[12] P. Delpierre et al., Nucl. Instr. and Meth. in Phys. Res., A315(1992)133-138.

[13] G. Catanesi et al., presented at the 3rd Int. Conf. on Advanced Technology and Particle Physics, Como, Italy, 1992, to be published in Nucl. Phys. B (Proc.Suppl.).

[14] F. Anghinolfi et al., CERN/ECP 91-26.

[15] F. Anghinolfi et al., CERN/ECP 92-6.

[16] E. Gatti and P. Rehak, Proc. of the DPF Workshop on Collider Detectors, LBL-15973 UC-37, Conf. 830224 (1983).

[17] P. Rehak et al., Nucl. Instr. Meth. A248 (1986) 367.

[18] W. Chen et. al., IEEE Trans. Nucl. Sci. 39 (1992) 619.

[19] M. Clemen et al., Nucl. Instr. and Meth. A316 (1992) 283.

[20] E. Gatti et al., Nucl. Instr. and Meth. A274 (1989) 469.

[21] A. Vacchi et al., Nucl. Instr. and Meth. A306 (1991) 187.

[22] S. Kleinfelder, IEEE Trans. Nucl. Sci. 37 (1990) 1230.

[23] G. Batignani et al., Nucl. Phys. B23 (1991) 291 and references therein.

[24] B.S. Avset et al., CERN EP/90-11 and references therein.

[25] A.S. Schwarz, Internal Note ALEPH 92-97 and references therein.

[26] P. Giubellino, Internal Note ALICE/SIL-92-3.

[27] SDC technical Design Report, SSC 92-201.

[28] W. Dabrowski et al., Internal Note ALICE/SIL-92/1.

[29] W.Dabrowski et al., Nucl. Instr. Meth. A314 (1992) 199.

[30] T.M.V. Bootsma et al., to be published in Nucl. Instr. and Meth.

[31] A. Oed, Nucl. Instr. and Meth. A263 (1988) 351; A. Oed et al., Nucl. Instr. and Meth. A284 (1989) 223.

[32] CERN-RD28 Collaboration, "Development of gas microstrip chambers for high radiation-rate detection and tracking".

[33] V.M. Dobulevitch et al., Internal Note ALICE/SIL-92/4.

[34] Metrologia 24 (1987) 187.

[35] RD-20 Status Report, CERN/DRDC 92-28.

[36] H. Wieman et al., CERN/DRDC 92–32, RD-32.

[37] J.W. Harris et al. Nucl. Instr. and Meth. A315 (1992) 33.

[38] A. Aqachmar et al., LAPP (Annecy, France), Internal Note.

[39] I. Lehraus et al., IEEE Trans. Nucl. Sci. 30 (1983) 50.

[40] Program developed by G. Rai at LBL.

[41] V.V. Parkhomchuck et al., Nucl. Instr. and Meth. 93 (1971) 269.

[42] W.B. Atwood et al., Nucl. Instr. and Meth. 206 (1983) 99.

[43] Yu.N. Pestov, Nucl. Instr. and Meth. 196 (1982) 45.

[44] Yu.N. Pestov, Nucl. Instr. and Meth. A265 (1988) 150.

[45] A.R. Frolov et al., Nucl. Instr. and Meth. A307 (1991) 497.

[46] H.R. Schmidt, Internal Note ALICE/TOF-93/11.

[47] Y. Galaktionov et al., Nucl. Instr. and Meth. A317 (1992) 116.

[48] G. Daskalakis et al., AU/NPPS-5-1992 (submitted to Nucl. Instr. and Meth.) and Internal Note ALICE/TOF 92-14.

[49] V. Agoritsas et al., CERN DRDC/P-25, RD-17.

[50] J. Engelage et al., Proceedings of the XXII International Conference on Cosmic Rays, Dublin, Aug. 1991.

[51] S. Albergo et al., Nucl. Instr. and Meth. A311 (1992) 280.

[52] M. Kuhlen et al., Nucl. Instr. and Meth. A301 (1991) 223.

[53] T.K. Nayak et al., Nucl. Instr. and Meth. A249 (1986) 354.

[54] S. Albergo et al., Internal Note ALICE/TOF-92/13.

[55] R .Albrecht and R Schulze, private communication.

[56] J.F. Genat, Proc. of the 1st Annual Conference on Electronics for Future Colliders, LeCroy Corp., 1991, p. 231.

[57] F. Piuz et al., Experimental Apparatus for High Energy Physics and Astronomy, Eds. P. Giusti et al., World Scientific, 1991, p.121.

[58] E. Nappi et al., CERN/DRDC 92-3 and DRDC 92-16, RD-26.

[59] H.-A. Gustafsson, Internal Note ALICE/ELEC-93/8.

[60] F. Piuz et al., presented at the 3rd Int. Conf. on Advanced Technology and Particle Physics, Como, Italy, 1992, to be published in Nucl. Phys. B.

[61] F. Piuz et al., CERN/PPE 92-200.

[62] G. Vasileiadis, Ph.D. thesis in preparation.

[63] M. French et al., CERN/ECP 92-2.

[64] WA98 Proposal, CERN/SPSLC 91-17, May 1991.

[65] V. Kachanov's communication to the Conference "Crystal 2000", Chamonix (1992).

[66] Status Report CERN/DRDC 92-2/RD18

[67] M. Chen, L3H - CERN/LHCC 93-15 and private communication.

[68] B. Adeva et al., Nucl. Instr. and Meth. A289 (1990) 35.

[69] G. Feofilov et al., Internal Note ALICE/MCP-92/9 and 92/10.

[70] R. Brockmann, Proc. on the Conf. of physics and astrophysics of quark-gluon plasma, World Sci., Singapore 1988, p. 617–623; see also P. Giubellino et al., Nucl. Instr. and Meth. A279 (1989) 259.

[71] T.F. Günzel et al., "A Silicon Pad Counter for First Level Triggering in Ultrarelativistic Proton–Nucleus and Nucleus–Nucleus Collisions", preprint HD–PY–91/6, 20 Nov. 1991.

[72] M. Izycki et al., University of Geneva, preprint DPNC 90–10–144 (1990).

[73] "MCP Assembly", Hamamatsu Technical Information, Sept. 1991.

[74] W.B. Feller, "Development of Microchannel Plates in Advanced Wind Tunnel Instrumentation", NASA Contractor Report 181947, Galileo Electro-Optics Corp., Sturbridge, Mass., Feb. 1990.

[75] C. Baglin et al., presented at the IEEE Nucl. Science Symposium, October 1992, Orlando, FL (USA).

3 Trigger and Data Acquisition

3.1 Trigger

3.1.1 Event Rates

The maximum initial luminosity for Pb–Pb collisions is limited by beam–beam interactions (QED processes) to $L \approx 1.8 \times 10^{27}\ cm^{-2}\ s^{-1}$ for a single interaction region and to half this value for two experiments (one dedicated and one pp detector) running in parallel [1]. With a luminosity half-life of $\approx$ 10 h and an inelastic cross-section of 5.5 b, the average minimum-bias interaction rate will be between 2000 events/s and 4000 events/s (for two or one experiment running, respectively). A few per cent of all interactions will be central collisions with maximum particle production. More than 90% of the projectile nucleons will interact in collisions with impact parameters b $<$ 2 fm corresponding to 2% of the cross-section or 40–80 events/s. Depending on luminosity, the centrality criterion could be relaxed up to $\approx$ 7% of the cross-section (b $<$ 3.5 fm, 75% of nucleons interacting). For lighter ion species (A $\approx$ 100), the luminosity could be about one order of magnitude higher, increasing further towards lower masses if not limited elsewhere in the injection chain.

3.1.2 Trigger Detectors

Because the interaction rate will be orders of magnitude lower than the LHC bunch-crossing frequency, the timing requirements for read-out electronics and trigger detectors are not very stringent and pipelining will not be required. All detectors will sample and hold the last event, either by their intrinsic delay (e.g. the TPC) or in the front-end electronics until receiving a clear or read-out signal. A pile-up rejection will ensure that only one single event has been seen by all detectors. The trigger and read-out architecture will therefore resemble the schemes used in fixed-target or DC accelerators.

Minimum-Bias Trigger

The interaction trigger will require a minimum charged particle multiplicity in $1 < |\eta| < 5$. It is formed by summing up the signal of the fast charged-particle multiplicity array (see 2.7.1). The same hardware should be operational for pp ($dN_{ch}/dy \approx 6$) as well as heavy-ion collisions.

If the time-of-flight method is chosen for the particle identification in the central region, the interaction time (time–zero) could be defined with the required precision of less than 50 ps by multiple measurements in e.g. the MCPs, which are under investigation for the multiplicity array. The time difference between the left and right arrays will locate the event vertex on the trigger level to $<$ 1–2 cm and provide effective rejection to beam–gas interactions or other sources of background. The quartz Cherenkov fibres in the zero-degree calorimeter may also provide excellent timing information (see 2.7.2).

Collision Geometry Trigger

Further triggering on centrality or impact parameter can be done both by requiring more particles in the multiplicity array (higher dN_{ch}/dy) and, more directly, by using the forward calorimeters. The number of participating nucleons can be determined by measuring the energy of the non-interacting nucleons of the beam nuclei (spectators) in the Zero-Degree Hadron Calorimeter (ZDC, see 2.7.2) located on both sides of the vertex at a distance of 90 m. Ideally, the energy resolution of $\approx$ 10% for a 3.1 TeV particle would be sufficient to measure, for central events, the number of participants to better than one participant. The influence of background generated in upstream interactions is being studied; however, because of the large energies involved and the small solid angle, the performance of the ZDC is not expected to deteriorate significantly. For peripheral reactions the correlation between number of spectators and zero-degree energy will be weaker because the nuclei could break up partially into fragments with different mass-to-charge ratios (see 2.7.2 and 4.6).

Other Trigger Options

An energy trigger in the photon spectrometer is envisaged to enrich statistics in the high-p_t region during pp running and for peripheral events. A trigger on unusual event topologies (fluctuations etc.) could be easily implemented into the multiplicity array. The additional electromagnetic calorimeters, which are under study for the forward region (see 2.8), could measure and potentially trigger on electromagnetic energy flow and especially the transverse energy per photon. This together with the charged-particle multiplicity would allow the selection of events with CENTAURO-like structure. A similar trigger could be implemented in the central region in the area covered by the photon spectrometer.

3.1.3 Data Volume

The total event size is completely dominated by the TPC, with 520k pads of 1000 time slices each, corresponding to a total data volume of 0.5 Gbyte. Simple zero suppression will reduce this number to 45 Mbyte per event. This estimate is based on 12 000 particles

each giving a signal on 5 pads in 75 rings with 8 time buckets plus 2 bytes of address; it corresponds to an average occupancy of 10%. It can be further reduced by centroid finding and wave-form analysis e.g. by a numeric filter (see 2.3). The limit is around 8 Mbyte/event assuming complete on-line hit reconstruction in both coordinates; realistically we hope to achieve about twice that value. Table 3.1 summarizes the event sizes from all detectors; the total size will be $\approx$ 50 Mbyte without and $\approx$ 20 Mbytes with cluster finding. Together with the requirement of $\approx$ 50 Hz data-taking rate, the data flow to the storage medium will be about 1.5 Gbyte/s.

Detector	Minimum event size (Mbyte)	Maximum event size (Mbyte)
Inner tracker	1.90	1.90
PID	TOF 0.20	RICH 1.60
TPC	with cluster fit 16.00	45.00
EM-CAL	0.50	0.50
Others	$\approx$1.	$\approx$1.
Total	$\approx$20.	$\approx$50.

Table 3.1: Event sizes of the subdetectors

3.2 Data Acquisition

The above requirements are about 2–3 orders of magnitude higher than today's performance of high-energy physics experiments. Compared with LHC pp experiments our event rate is much lower, but the event size is much bigger, the overall throughput being comparable. Therefore we can envisage a similar data-transport medium. We will coordinate our efforts with the ongoing R&D of the pp experiments, with the relevant CERN DRDC projects, and rely wherever possible on industry standards. However, unlike in pp physics we do not foresee to analyse or filter most of the events in real time. Because of the mode foreseen for heavy-ion running (few weeks/year), this is also not required and allows a more unbiased offline analysis of the complex events. The whole data stream will therefore be written on a permanent storage medium.

A single medium will not be able to accept a data throughput of several Gbyte/s and therefore the classic tree-structured data acquisition system has to be abandoned. We propose to multiply the event builder and storage devices on top of the tree and connect to the parallel front-end read-out system through a switch matrix. In this way we can scale the performance to our needs with available technology simply by adding devices.

The bandwidth of the point-to-point interlink media such as used in B-ISDN can be expected to reach 100 to 200 Mbyte/s. Allowing for a reserve in bandwidth (in order to de-randomize the event arrival) we will need about 16 links from the front-end data concentrators to the switch matrix.

We assume that most digitizing electronics (ADCs, TDCs, discriminators etc.) will be mounted directly on the detector or very close to it. They will be connected to the data acquisition system via highly multiplexed digital busses or fibre optical links. In this way we not only save cabling but also reduce noise problems as no analogue signals will travel on long cables.

The digital busses between the counting room and the detectors are, by their nature, detector specific. However, the crate-based bus system receiving these data can easily be standardized. The VME standard with a multitude of commercial modules available almost fulfils our requirements with respect to bus bandwidth ($\sim$ 80 Mbyte/s for D64 block transfers). However, we can expect that well before the construction of the experiment this will also be true for Futurebus+ with a bandwidth of about 200 Mbyte/s. We propose this or another commercial standard to avoid developing general-purpose modules such as processors, memories and bus and link interfaces. As each detector bus interface can handle many physical channels (10^4 to 10^5), the number of such crates will be small compared with LEP standards, maybe a few dozen in total.

For reasons of bandwidth we abandon the bus approach for the inter-crate connections in most cases (at most 10 Mbyte/s on long busses). They will be replaced by dedicated point-to-point optical links. Several such links are presently under development (SCI, HIPPIE). They will also be interfaced directly to the data-driven switch matrices. Even if new network protocols on this media should allow multi-master operation, we prefer the dedicated point-to-point links in order to avoid collision handling and to obtain a deterministic and short event latency and therefore reduce our total buffer memory needs. The latter will in any case amount to tens of gigabytes.

Only the monitoring and control of the apparatus will need a significant amount of processing power, with the possible exception of cluster finding in the TPC. We are confident that by the time of the experiment enough cheap computing power will be available. Our requirements in this respect are relatively

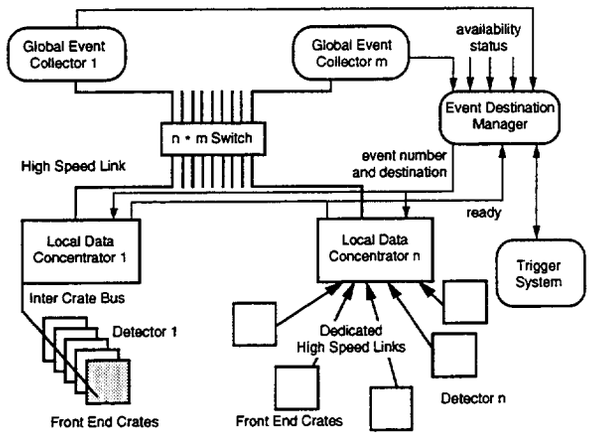

Figure 3.1: Layout of the data acquisition system

modest and the use of existing technology could already provide a reasonable solution.

The proposed data acquisition system resembles the classical hierarchical approach with the exception that the event builder and data recorder are multiplied for reasons of bandwidth and writing speed. This becomes possible through the technology of switch matrices. Part of the event building is delayed until the off-line analysis, adding some minimal overhead. This is necessary since the switching algorithm will not be completely deterministic and the event contiguity cannot be assured without intermediate buffering, and hence consequences on throughput and latency. The event building will be provided implicitly by the Event Destination Manager which, however, does not copy data but only labels them with destination and event number (Fig. 3.1).

The Event Destination Manager

This is the central part of the system and has to be interfaced to almost all other components. It receives a hardware trigger from the separate trigger system. The signals of the trigger system have to be distributed directly to the front-end digitizing electronics. The EDM distributes this signal together with a unique event number to the Local Data Concentrators (LDCs). At the same time it provides a destination address corresponding to one of the logging stations.

In order to optimize throughput, the EDM has to keep track of the status of the logging stations. It also receives the ready messages from the LDCs and returns them to the trigger system. We foresee several kinds of triggers to allow the read-out of different parts of the apparatus in order to accommodate special physics interests or a mismatch in detector and acquisition speeds of different subdetectors.

The failure or temporary non-availability due to the change of medium of one or a few recorders causes the EDM not to use them as destinations and still provides a full or only slightly reduced system performance. A general purpose-processor with interfaces to the trigger (Fast Digital IO), the local data concentrators and the data recorders (independent low-bandwidth fibre link with broadcast capability) can implement this functionality.

The Local Data Concentrators

Their task is to receive the trigger signal together with destination and event number and distribute it further to the read-out crate controllers, and to report the end of the digitization back to the EDM. Asynchronously to the above activity it collects events from the data reduction pipelines of each read-out crate and transmits the data to the recorder across the switch matrix.

The LDC has to maintain a local event buffer several events deep (typically as many as the number of data recorders). This is necessary as only one LDC can write at any given time to a particular data recorder. However, transfers of various LDCs to different data recorders can go on in parallel exploiting the full bandwidth of the switch and not just of one link.

The LDC has to add a unique event number to the data stream. It also has to provide a subsample of the data to local monitoring software. The LDC will be housed in a Futurebus+ or other standardized crate together with the detector interfaces. If the level of electronics integration in one crate does not allow the use of the full bandwidth of the backplane bus it will be interfaced by point-to-point links to slave crates containing only detector interface cards. About one LDC per every two Mbytes of data will be needed, or at least one per subdetector.

The Front-end Read-out Controllers

Each read-out crate contains a controller collecting the events from the detector bus interfaces. Before transmitting them to the LDC it passes them through a processor pipeline reducing the data to the available bandwidth. At least twenty 50 MIPS processors/crate are needed to handle a flow of 30 Mbyte/sec in one crate (120 instructions/32 bit datum). We prefer a distributed reduction scheme in order to limit the data flow at the source.

The Switch Matrix

At the moment we foresee 16 inputs and 16 outputs to this matrix and rely on the commercial availability

of these devices that are currently still under development. These devices receive packages at their inputs and route them to the output node whose address is contained in the data packages. Commercial switch matrices developed for telecommunication may well meet our needs despite some differences in the application. Our data packages are usually quite long and we would like to avoid switching before one such package has crossed the matrix in order to ensure at least the contiguity of one subevent.

The Data Recorder

We can hope for cheap storage devices capable of writing 50 Mbyte/s with the advent of High Definition Television (HDTV) recorders. Present technology already allows a writing speed of 32 Mbyte/s. For our application we would need 50 such devices including a certain overcapacity for the sake of fault tolerance.

With HDTV we expect 200 Gbyte of media capacity leading to a change of media every two minutes in total and every two hours per drive. We will have to use a robotic mounting and archiving system.

The above approach is by its nature a scaleable one and the technology of switch matrices allows the overall throughput to be reached with the bandwidth available on a given single transport and storage medium. The actual performance of these devices will determine which degree of multiplication and parallelism has to be finally applied.

As a consequence of the used buffer dispatch mechanism one run will be distributed over several storage media. It cannot be guaranteed that events will be contiguous on one medium, but all parts of the same event will be on the same medium. Therefore a single portable medium belonging to one run can be analysed independently.

Software Platform

Having chosen an open hardware platform we will take the same approach for software. Currently a standardized real-time version of UNIX (POSIX) seems the most adequate choice.

3.3 Off-line Computing

The reconstruction of a few 10^7 events per year, corresponding to a few hundred Tbyte of data, will require massive computing power for off-line analysis. The most time-consuming task is likely to be pattern recognition and track fitting in the TPC and the inner tracking system.

We base our estimates on current heavy-ion experiments. Both NA36 and NA35/49 employ TPCs as their main tracking device to reconstruct several hundred tracks/event at track densities of $0.1\text{–}1/\text{cm}^{-2}$ which are comparable with or even exceed the one at the LHC. The full analysis chain in both cases amounts to $\approx$ 1.5 Mflops/track, or 15 Gflops for a single high-multiplicity LHC event. Adding 50% for Monte Carlo simulations, we would need a steady-state computing power of $\approx$ 35 Gflops to process 5×10^7 events in one year.

A very similar number has been estimated for the combined needs of the two largest RHIC collaborations [2]. We expect that by the end of this century such computing power will be available at reasonable cost, e.g. in the form of a cluster of workstations.

References

[1] Design Study of the LHC, CERN 91–03 (1991).

[2] Off-line Computing for RHIC Experiments, RHIC/DET 8 (1992).

4 Physics Performance

In this section we summarize the expected performance of the ALICE detector. Instead of comparing with any of the specific models, which often vary in their predictions for a particular signal by large factors, we prefer to show our *sensitivity* to a number of *observables* directly related to experimentally measured quantities. The topics discussed are:

- track finding and momentum resolution
- hyperon detection
- particle identification
- particle interferometry
- lepton pairs
- prompt photons
- global-event characteristics

Existing event generators differ widely in their predictions concerning the global-event characteristics of heavy ion collisions at the LHC. The predicted particle densities at midrapidity range between $dN_{ch}/dy \approx 2000$ to ≈ 6000 and in extreme cases up to 8000 [1, 2]. Our detector simulations were done with $dN_{ch}/dy = 8000$, a conservative choice which should include some safety margin. For many of our studies we used a simple event generator SHAKER [3], because the available Monte Carlo generators often do not include some of the particles of interest to us (e.g. $\eta, \phi, J/\Psi$, etc.). In the phase-space generator SHAKER, particles are generated with a constant rapidity density. The transverse-momentum distributions are simulated using data from the Tevatron [4, 5] for pions, kaons and protons; and m_t scaling [6, 7], for most other particles. Particle ratios are taken from isospin symmetry ($\pi^0/\pi^+ = 1$, $K^0/K^+ = 1$), Tevatron data (K^+/π^+, p/π^+) [5], or ISR measurements (η/π^0, vector mesons).

4.1 The Tracking System

The track finding capability of our tracking system has been evaluated by using the GEANT simulation package [8] with the performance parameters of silicon drift (innermost four planes), silicon strips (5th plane) and TPC quoted in sections 2.2 and 2.3. Average materials for supports, electronics, cabling and cooling have been included in the simulation studies [9]. Hits closer than the corresponding double-track resolutions were merged and then smeared according to the expected spatial resolutions. Space points obtained this way were later used as an input for the track-finding and reconstruction procedures.

4.1.1 Optimization of Layout

The performance of the tracking system was studied for various radii of the beam pipe and different configurations of the inner tracking layers (ITS). The number of layers and their position were optimized for good efficiency in track finding and momentum resolution. Because of multiple scattering in the inner wall of the TPC, the matching efficiency between TPC and ITS depends crucially on the gap between the two; the chosen radius of 50 cm for the outer superlayer represents a compromise between performance and cost. The exact configuration and a number of hardware options for the ITS are still under evaluation (see 2.2).

We have opted for a beam pipe of 13 cm diameter in the central region, which is as close as possible to the innermost tracking plane. A smaller (and correspondingly thinner) pipe would improve only slightly the momentum resolution (we use the vertex as constraint), at the expense of angular resolution, which is found to be more important in our case (see e.g. 4.3.1). The impact parameter resolution is sufficient for hyperon decays ($c\tau$ of order cm), and the vacuum inside the pipe provides a decay zone of the right dimensions.

4.1.2 Track Finding

The track finding is performed in several steps:

- finding tracks in the TPC alone;
- connecting tracks found in the TPC to hits registered in the Inner Tracking System;
- finding tracks with very low transverse momenta in the Inner Tracking System only.

The track finding in the TPC starts from the outermost pad rows, where points are less affected by the limited two-track resolution. In Fig. 4.1 the distribution of tracks as a function of the fraction of resolved (i.e. non-merged) hits per track is shown for the 20 outermost (a) and the 20 innermost (b) pad rows.

The large number of 'good' (i.e. non-merged) hits per track on the last twenty pad rows (93% on average) and the high density of points along the track (pad length = 2 cm) allow us to apply the track-following method [10] as the first step of the track-finding algorithm. Tracks are followed from one pad layer to another using locally a parabolic model in the bending projection and a linear one in the non-bending plane. We allow up to two subsequent pad rows without matching hits. Whenever 15 or more hits are found for one track candidate, we fit the track by a helix, which is then used to build up the track

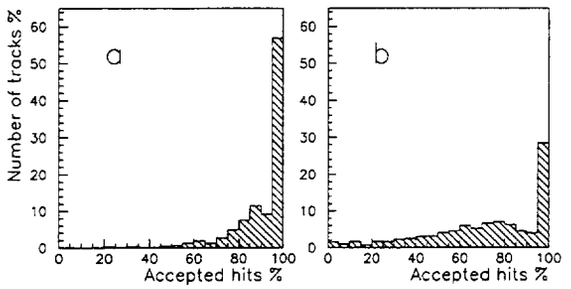

Figure 4.1: The distribution of tracks as a function of relative number of accepted hits in the 20 outermost (a) and the 20 innermost (b) pad rows.

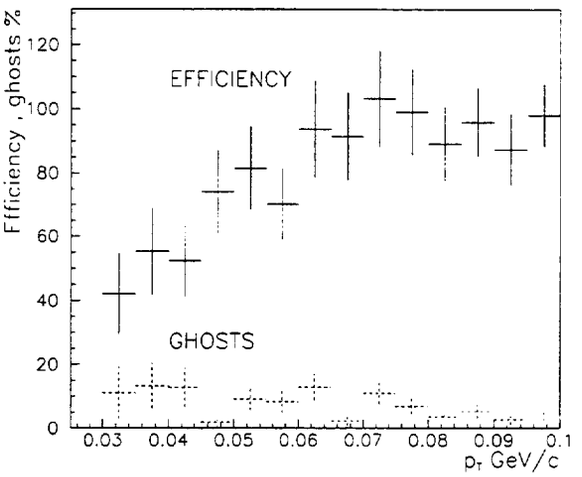

Figure 4.3: The efficiency of the track finding and the relative ghosts yield as a function of p_t in the low momentum range.

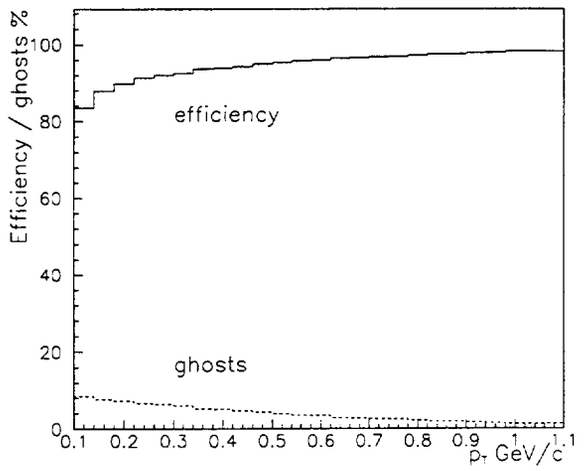

Figure 4.2: The efficiency of the connection and the probability of incorrect matching between TPC and inner tracking system as a function of p_t.

road for the collection of other hits from the inner part of the TPC. The track parameters are continuously updated and the accepted hits are removed from the pool. For the highest particle density considered we find a reconstruction efficiency of $\approx$ 93%, practically independent from p_t down to 100 MeV/c.

The number of ghost tracks produced by this algorithm is negligible, because of the large hit density along the track (75 pad rows, 83% of good hits on average).

The next step of the track finding is the connection of tracks found in the TPC to the Inner Tracking System. Using the track parameters from the TPC, we search for hits matching both in position and in angle in the outermost two layers of the ITS. The resulting matching efficiency is shown in Fig. 4.2. At lower momenta (p_t < 200 MeV/c) the efficiency of matching (obtained for pions) drops below 90%. We expect further improvement by including the inner layers in the search strategy.

Finally, we try to find tracks with very low momenta using only the inner tracking system. The main reason is the rejection of asymmetric Dalitz pairs; therefore we concentrate in the following on electrons, which have a smaller multiple scattering ($\beta \approx 1$). At this stage we use a simple simulation in which multiple scattering in the beam pipe and in five layers of the detector is taken into account. The hits of tracks reconstructed earlier are removed from the ITS. To find leftover tracks we apply roads along the track model, both in bending ($r-\phi$) and non-bending ($r-z$) projections. We assume that the vertex position is known with a precision of 12.5 μm (which is the bunch size [11]) in the transverse plane, and of 50 μm along the beam direction. This precision is obtained from the high-momentum tracks found earlier. We repeat the search in several passes, enlarging the roads for tracks with lower momenta. At the moment, we require the tracks to have hits in all five planes, but we plan to relax this requirement in the future. If less than four hits are correctly found, the track is considered a 'ghost'. The efficiency and relative number of ghost tracks obtained with this algorithm are calculated with respect to the number of tracks with hits on all planes (77% for a single plane efficiency of 95%). They are shown in Fig. 4.3 as a function of p_t.

The track-finding algorithms for the TPC and the ITS are under continuous evolution. Other methods such as Hough transform [12] and neural networks [13] are also considered.

4.1.3 Precision of Reconstruction

In the momentum range of interest the precision of track reconstruction is mainly determined by multiple scattering. In order to estimate the influence of the detector resolution and multiple scattering, we compared the results obtained by the maximum-likelihood method with those obtained analytically using the inverse of the Fisher information matrix, which can be considered a theoretical limit (see chapters 5 and 7 in ref. [14]). The covariance matrices obtained with both methods almost coincide. This allows us to use the analytical method, which is more convenient in terms of computing time.

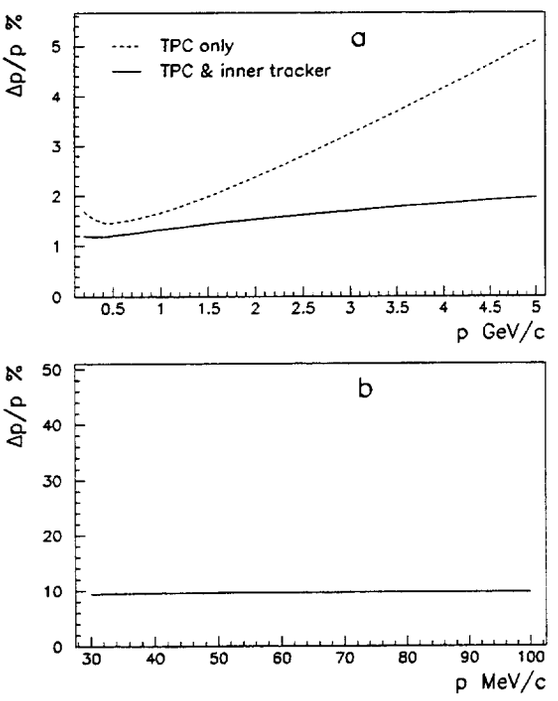

Figure 4.4: The momentum resolution as a function of momentum obtained by the TPC alone and by the TPC with the Inner Tracking System (a) and, for low momenta electrons, using only the Inner Tracking System (b).

For the track fitting we calculate the radius using triplets of subsequent measurements along the track. It can be shown that, if the detector resolution is dominated by multiple scattering, such estimates of the track radius are uncorrelated and hence we can obtain an unbiased estimate by a weighted mean. This simple method has been found to give the same results as the more time consuming maximum-likelihood method.

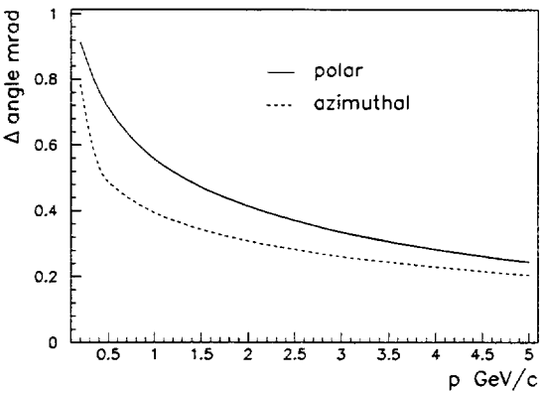

Figure 4.5: Errors of polar and azimuthal angles as a function of particle momentum.

Energy loss has not been included in this study of reconstruction precision. However, when this effect is taken into account by using a mass-dependent fit. we expect that the resolutions should not deteriorate significantly at higher momenta.

The momentum cutoff by energy loss is $\approx$ 80 MeV/c for pions and $\approx$ 200 MeV/c for kaons.

In Fig. 4.4a the momentum resolution for pions is shown as a function of momentum, obtained with the TPC alone and with the complete tracking system. The TPC measurements are taken starting at a radius of 120 cm only (see 2.3). The dependence of $\Delta\ p/p$ can be approximated by :

$$\Delta p/p = (1.2 \oplus 0.3 \times p) \quad (\%) \qquad (4.1)$$

except for very low momenta, where the $1/\beta$ term in multiple scattering dominates. Figure 4.4b shows the momentum resolution as a function of momentum for very low momenta electrons, obtained with the Inner Tracking System only.

The angular resolution for both polar and azimuthal angles (using the complete tracking system) is presented in Fig. 4.5. The inaccuracy of measurements, except for very low momenta, is well below 1 mrad.

The effective mass resolution of a particle decaying into an e^+e^- pair is shown in Fig. 4.6. The mass resolution is $\Delta m/m \approx 1\%$, i.e. 8 MeV/c^2 for ρ and ω, 10 MeV/c^2 for ϕ, 30 MeV/c^2 for J/ψ, and 150 MeV/c^2 in the Υ region.

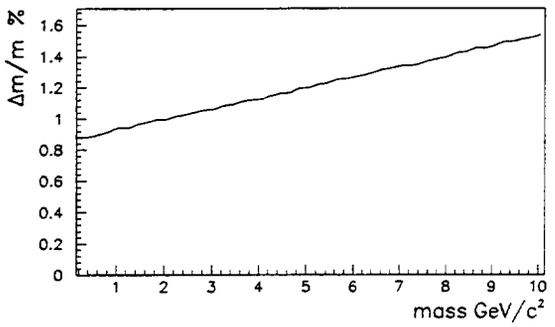

Figure 4.6: The effective mass resolution as a function of mass for the decay of a particle into a e^+e^- pair.

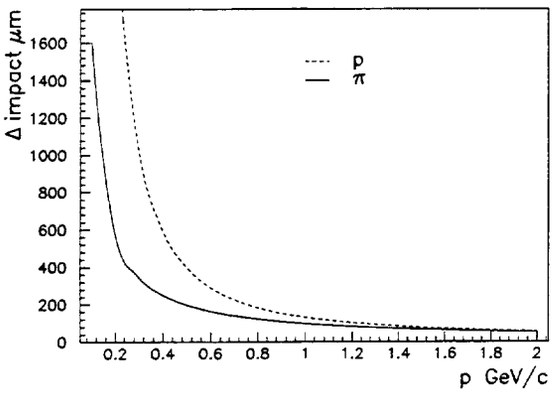

Figure 4.7: The impact parameter precision as a function of particle momentum.

4.1.4 Detection of Strange-Particle Decays

To identify secondary vertices from strange-particle decays with typical decay paths of a few cm, we need an accuracy of a few mm for the determination of impact-parameters with respect to the primary vertex. The impact parameter precision using the TPC only is $\approx$ 1 cm for 0.5 GeV/c pions and therefore is not sufficient. The result including the ITS are shown for pions and protons in Fig. 4.7. Secondary vertices will be resolved starting a few mm away from the interaction point. In the following, we conservatively define 1 cm and 6 cm as the lower and upper limits for the reconstructable decay zone, respectively. The geometrical acceptance for $\Lambda \rightarrow \pi^-$p, $\Xi^- \rightarrow \pi^-\Lambda \rightarrow \pi^-\pi^-$p and $\Omega^- \rightarrow$ K$^-\Lambda \rightarrow$ K$^-\pi^-p$ decaying within this zone has been calculated. The result for Λ, including the branching ratio, is shown in Fig. 4.8 as a function of rapidity and transverse momentum. For the geometrical acceptance, integrated over p_t and rapidity, we obtained 10% for Λ and 2.7% for Ξ^-.

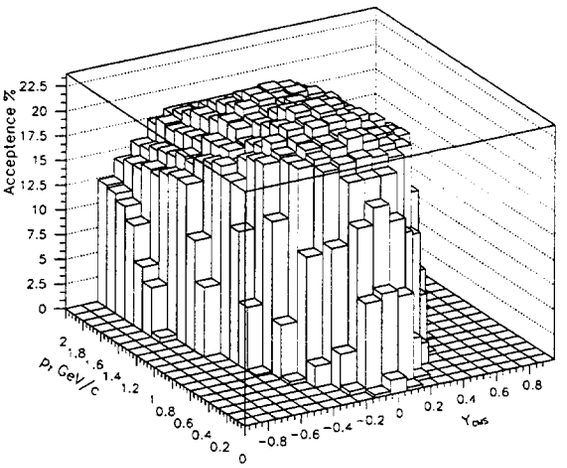

Figure 4.8: The Λ acceptance in rapidity and transverse momentum.

For the estimation of the reconstruction efficiency of Λ's we used SHAKER with a Λ/π ratio of 2%. After the standard track-finding procedure we search for pions not pointing to the main vertex and combine them with identified protons in the momentum range 0.5–2 GeV/c. Whenever the combination gives an acceptable secondary vertex within the decay zone, we verify the pointing of the total momentum vector of the Λ candidate to the main vertex. With this method we can reconstruct 50 $\pm$ 10% of the Λ's with decay vertices inside the decay zone and $p_t > 600$ MeV/c. The number of fake combinations is very small, so Λ's are detected with little background.

With the above geometrical and reconstruction efficiencies, we estimate the yield of reconstructed Λ's and Ξ's in central Pb-Pb collisions to be 13 and 0.15 per event, respectively. A similar investigation for Ω and K^0 is under way.

4.2 Particle Identification

Particle identification is achieved with a combination of TOF or RICH and dE/dx measurements in the tracking system (ITS and TPC). The requirements for separation of hadrons are modest for $p_t > 1$ GeV because of similar relative abundances (π/K $\approx$ 0.2–0.3, K/p $\approx$ 0.5–1 at the Tevatron). For single tracks, a separation of more than 3σ will be sufficient to have $< 10\%$ contamination of misidentified particles; inclusive particle ratios can be measured as long as the

separation is better than 2σ.

4.2.1 Particle Identification in Silicon

The measurement of energy loss in thin silicon detectors can be used for particle identification in the nonrelativistic ($1/\beta^2$) region.

Together with tracking and momentum reconstruction, the analog pulse-height measurement in 3–4 layers makes the ITS an independent particle spectrometer for low-momentum tracks which do not reach the outer detectors because of decay, energy loss, or curling. The most probable energy loss in 300 μm Si is shown in Fig. 4.9, calculated according to [15, 16] including density effects.

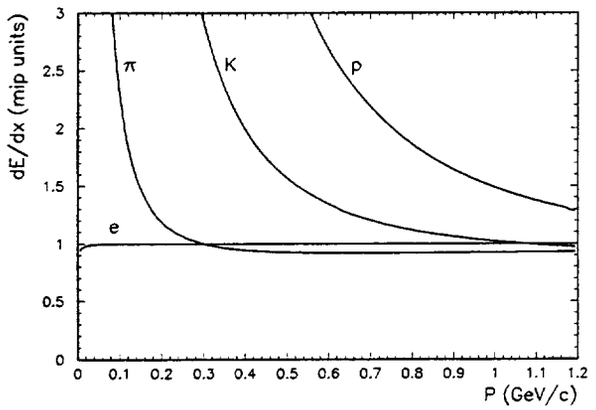

Figure 4.9: Most probable energy loss in 300 μm Silicon for e, π, K, p as a function of momentum, normalized to 1 at high p_t.

The expected dE/dx resolution has been simulated using as single detector response (Fig. 4.10a) a modified Landau distribution [17] which accurately describes the observed pulse-height distribution in 300 μm silicon detectors [18, 19]. The truncated mean using the two lowest out of four measurements is shown in Fig. 4.10d; it is almost Gaussian with a σ of 10% (full line). The r.m.s. of the full distribution is $\approx$ 12%.

The results for tracks with only three measurements ($\approx$ 20% at 95% single detector efficiency in four planes) are only slightly worse with a σ of 12% and an r.m.s. of 14% (Fig. 4.10c). The percentage of measurements above and below a certain threshold is shown as a function of this threshold in Fig. 4.11. The achievable rejection (at 95% efficiency) between two particles exceeds a factor of 100 if their energy loss differs by more than 50%. Therefore the dE/dx measurement in the ITS will be able to provide sufficient separation in the regions $p < 140$ MeV/c (e/π), $p < 520$ MeV/c (π/K), and $p < 1$ GeV/c (K/p) (see Fig. 4.9).

4.2.2 Particle Identification by the TPC

In our experiment, particle identification based on dE/dx in the TPC will mainly be used to identify electrons below 3 GeV/c. The particle separation has been estimated with a parametrization of energy loss as measured in the ALEPH TPC [20] assuming a 7% energy resolution for non-isolated tracks (see 2.3). The calculated separation is shown in Fig. 4.12 for pions, kaons, protons, and electrons as a function of momentum. This resolution, while not sufficient by itself for hadron identification in the relativistic rise, still adds to the π/K separation of a TOF or RICH detector in the momentum range between 2 and 4 GeV/c (see below).

4.2.3 Particle Identification by TOF/RICH

In addition to dE/dx, a second particle identification system is needed for hadrons and to resolve ambiguities in the cross-over regions of the energy loss for electrons (Fig. 4.12)

Pending the final experimental solution adopted, the PID wall will be placed between 3 and 4.5 metres from the beam. The smaller distance, adequate for a TOF with σ = 100 ps, would allow a lower momentum cutoff of $\approx$ 130 MeV/c for electrons, and therefore continuous electron identification in silicon ($p_t < 140$ MeV/c), TOF (130 MeV/$c < p_t <$ 500 MeV/c), and TPC ($p_t >$ 200 MeV/c). A second, small-area TOF array will be located in front of the e.m. calorimeter at $r \approx 6$ m. It will improve the particle identification for inclusive ratios at high p_t and act at the same time as charged-particle veto for the calorimeter. The particle separation is shown for both distances in Fig. 4.13 assuming a resolution of σ = 100 ps. The performance of the alternative technology, the RICH detector, is comparable and even slightly better at high momenta (see 2.5).

4.2.4 Combined Particle Identification

The combined separation power of TPC and TOF is shown in Fig. 4.14 for the large-acceptance TOF at r = 3 m (solid lines) and the small solid angle covered with TOF at r = 6 m (dashed lines). For hadrons, we have more than 3 σ separation for pion and kaon identification below 2 GeV/c and for protons below 3 GeV/c, which is sufficient for event-by-event particle ratios, HBT analysis, and decay reconstruction because it includes the majority of all

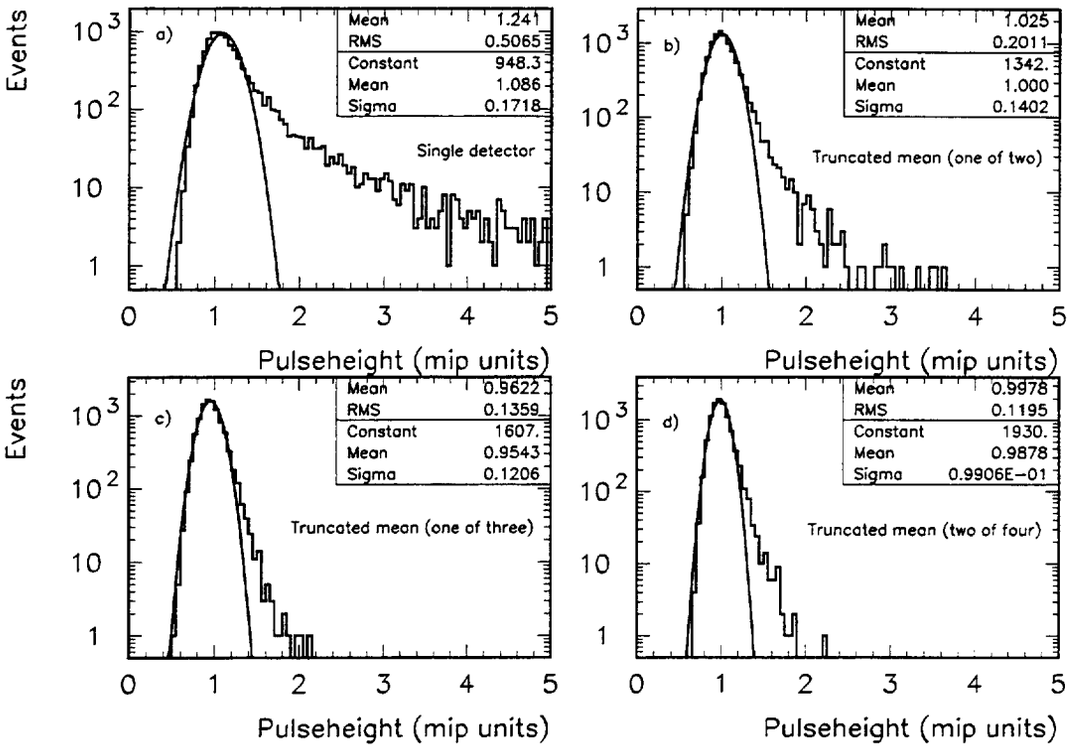

Figure 4.10: Simulated pulse-height distributions in silicon detectors, normalized to 1 at the most probable value. The parameters of a Gaussian fit (full lines) around the most probable value are shown in the plots. a) Single detector response to minimum ionizing particles. b-d) Truncated mean using the m lowest of n measurements (b: one of two, c: one of three, d: two of four).

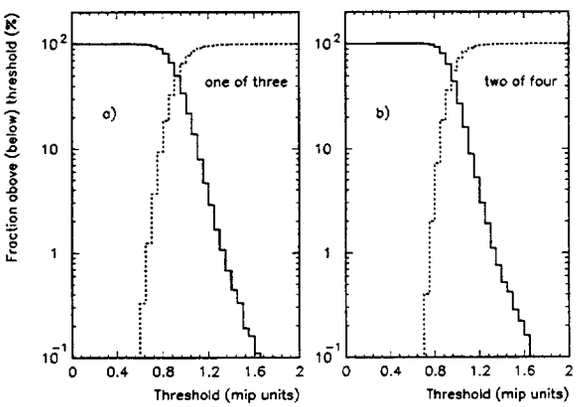

Figure 4.11: Percentage of hits above (full line) and below (dashed line) a given pulse-height as a function of this pulse-height. a) Truncated mean using one out of three and b) two out of four measurements.

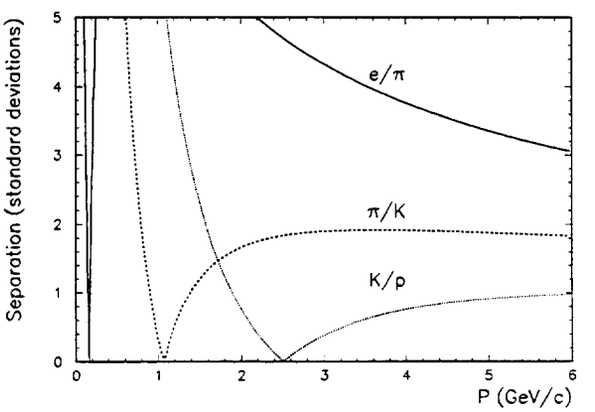

Figure 4.12: Particle separation in the TPC with dE/dx resolution σ = 7%.

produced hadrons. Inclusive ratios can be measured up to $\approx$ 4 GeV/c ($\approx$ 6 GeV/c for r = 6 m), i.e. well into the minijet region.

Pions will be identified in the silicon detectors at small distance (r < 50 cm) for p < 140 MeV/c, kaons for p < 520 MeV. This reduces the decay losses, which are substantial at low p_t because of the large flight path towards the particle identification detectors. The total survival probability, integrated over momentum (and neglecting energy loss) will be 80% for pions and 54% for kaons.

As an example for the performance of the combined tracking and particle identification, Fig. 4.15 shows the transverse momentum spectrum of a single event generated with SHAKER at dN_{ch}/dy = 8000. Including tracking efficiency and particle decays, we would reconstruct $\approx$8000 pions (full line) and $\approx$1200 kaons (circles) inside the acceptance. Our π/K separation of better than 3 σ for p < 2 GeV/c and better than 2 σ up to 4 GeV/c is adequate for measuring the shape of the momentum spectra and the particle ratios in a single event.

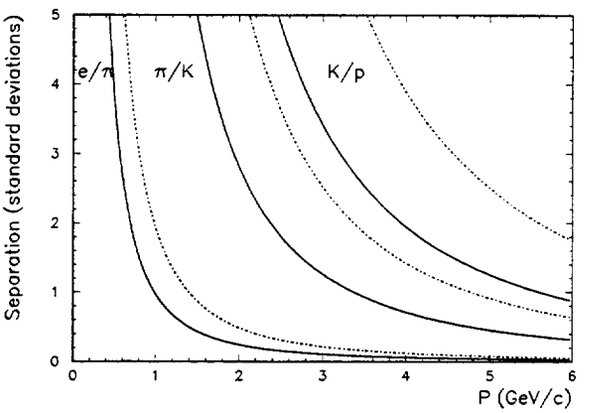

Figure 4.13: Particle separation with TOF (resolution σ = 100 ps) at 3 m (full lines) and at 6 m (dashed lines) from the vertex.

4.3 Boson Interferometry

The main application of boson interferometry in heavy-ion physics is the estimate of the parameters characterizing the space–time evolution of the system after the collision.

Its feasibility depends on a large set of experimental features. We shall briefly discuss the most important ones: two-track resolution, momentum resolution and acceptance. We shall use the decomposition of the two-particle momentum difference vector in the cylindrical system, defined in the following way:

- $Q_{T_{side}}$ is perpendicular both to the collision axis and to the total momentum vector of a particle pair,
- $Q_{T_{out}}$ is perpendicular to the collision axis, and parallel to the total momentum vector of a particle pair,
- Q_L is parallel to the collision axis.

More details may be found in ref [21].

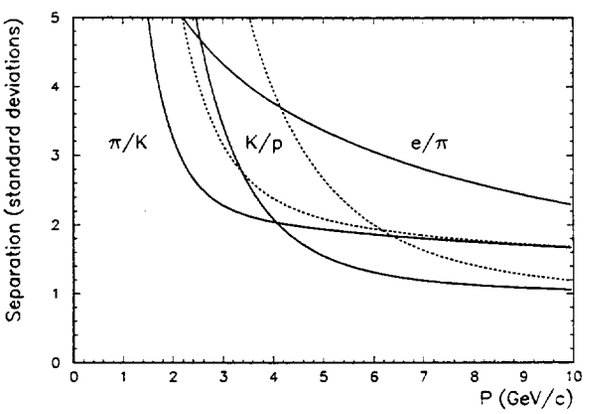

Figure 4.14: Combined particle separation with TPC (σ = 7%) and TOF (σ = 100 ps) at r = 3 m (solid lines) and r = 6 m (dashed lines).

4.3.1 Two-Track Resolution

The effect of the two-track resolution was simulated by rejection of track pairs whose impact points were closer than the two-track resolution, both at the entrance (r = 100 cm), and in the middle (r = 175 cm) of the TPC detector. The resulting fraction of resolved pairs is shown in Fig. 4.16, as a function of

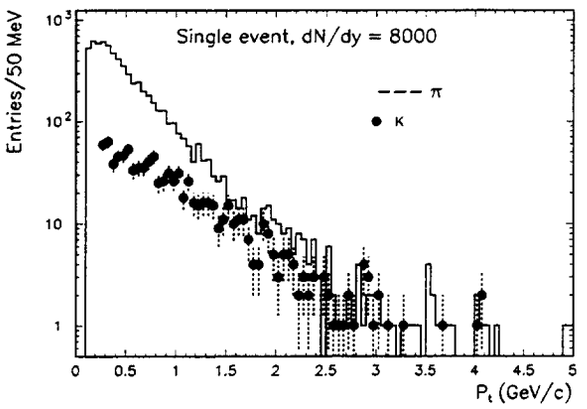

Figure 4.15: Transverse momentum distribution of pions (full line) and kaons (circles) of a single event generated with SHAKER, including particle decays and tracking efficiency.

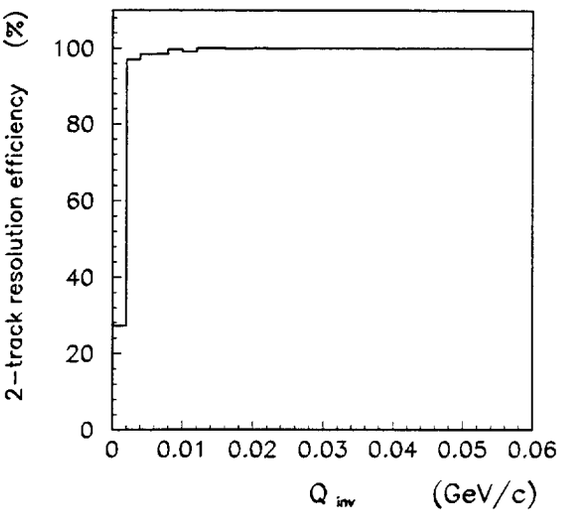

Figure 4.16: Two-track-resolution efficiency as a function of the invariant momentum difference.

the invariant momentum difference. The acceptance below 5 MeV/c would increase if the two-particle separation were improved by the unfolding method mentioned in section 2.3. The inner tracking system could also help in resolving tracks which are not well seperated in the inner part of the TPC.

4.3.2 Momentum Resolution

The single-particle momentum resolution was discussed in detail in section 4.1.3. Using the same method and assumptions, we estimated the resolution of the interferometric variables previously defined, $Q_{T_{side}}$, $Q_{T_{out}}$ and Q_L.

After smearing the single-particle momentum vectors according to the resolution, we calculate the two-particle momentum difference components $Q'_{T_{side}}$,$Q'_{T_{out}}$ and Q'_L. The resolution of the momentum difference was estimated by comparing the original and the smeared values. The extracted root mean square of the resolution function in each component is (for particle pairs with $Q_{T_{side}} < 50$ MeV/c, $Q_{T_{out}} < 50$ MeV/c and $Q_L < 50$ MeV/c):

r.m.s. $(Q_{T_{side}} - Q'_{T_{side}}) = 0.4$ MeV/c
r.m.s. $(Q_{T_{out}} - Q'_{T_{out}}) = 3.5$ MeV/c
r.m.s. $(Q_L - Q'_L) = 0.6$ MeV/c.

The resolution for the $Q_{T_{out}}$ component is mostly determined by the resolution of the track curvature, while the resolutions for the other two components, $Q_{T_{side}}$ and Q_L, are mostly determined by the angular resolution. Compared with 10 MeV, which is approximately equal to the r.m.s. of the correlation function corresponding to the maximal expected effective source size (20 fm), the resolution for the $Q_{T_{side}}$ and for the Q_L component is very good, and still sufficient for the $Q_{T_{out}}$ component. Therefore, in both the sideward and the longitudinal coordinate, we shell be able not only to determine the width of the widest component of the correlation function, but also to study in detail its shape. Unexpectedly large effective source sizes up to 40 fm may still be measureable.

In order to demonstrate the effect both of the momentum resolution and of the two-track resolution on the correlation function, we have generated events with simulated correlation, and then introduced both resolution effects. The correlation was introduced by addition of new particle pairs to the original uncorrelated sample. A Gaussian shape was simulated for the correlation function in all three components, with the intercept $\lambda = 0.5$, and with all three effective sizes equal to 20 fm. The analyzed sample consists of 40 events with $dN_{ch}/dy \simeq 8000$. The result is shown in Fig. 4.17, where the smeared correlation function is compared with the one with perfect resolution (shown by a full-line histogram). Projections of both correlation functions to the three momentum components are shown, as well as the correlation as a function of the invariant momentum difference. The region of momentum space which is projected on a given momentum component was chosen to be narrow in the other two components (< 10 MeV/c), in order not to dilute the correlation effect.

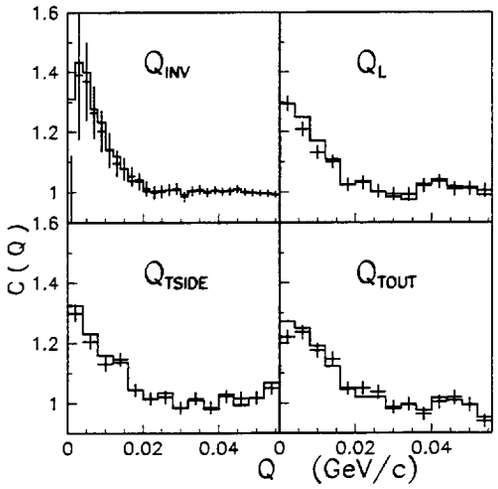

Figure 4.17: A comparison of the simulated correlation function, including two-track and momentum resolutions, with the unaffected correlation function (the latter is shown by a full line histogram). In the upper left quadrant of the figure, the correlations are shown as a function of the invariant momentum difference (Q_{inv}). In the other three quadrants, projections of the correlation functions to the individual momentum components ($Q_{T_{side}}$, $Q_{T_{out}}$ and Q_L) are shown.

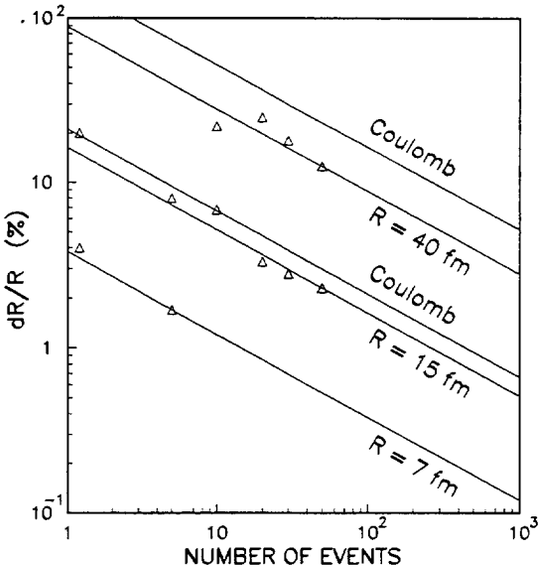

Figure 4.18: Measurement accuracy for the effective interferometric sizes: R=7 fm, 15 fm and 40 fm, as a function of the number of events. See text for details.

As can be seen in the figure, the correlation function is only weakly affected by resolution effects.

4.3.3 Acceptance

The longitudinal effective size is closely related to the decoupling proper time of the source, which in turn is directly related to dynamics. For the unbiased study of the longitudinal component of the correlation function it is necessary that the acceptance in rapidity be sufficiently wide. Otherwise the correlation function would have a cutoff at a certain Q_L, even before it reaches the plateau (note that the maximal Q_L depends on the available rapidity interval).

The feasibility of single-event interferometry depends on the statistics available in a given event. The error will be essentially proportional to the square root of the number of particles in the acceptance.

For the study of the Coulomb force in a multiparticle environment, which is related to the corrections for the Coulomb repulsion between like-sign particles, it is important to have good acceptance for particles of both charges.

Two units of rapidity are sufficent for all these requirements.

4.3.4 Single-Event Pion Interferometry

The statistical accuracy dR/R for the measured effective sizes ($R_{T_{side}}$, $R_{T_{out}}$ and R_L) depends on the following parameters:

- the number of events ($dR/R \propto (\sqrt{N_{events}})^{-1}$)
- the phase-space density ($dR/R \propto (dN/dY)^{-1}$)
- the acceptance ($dR/R \propto (\sqrt{\Delta Y \Delta \varphi})^{-1}$)
- the track reconstruction efficiency,
- the effective sizes and
- the correlation intensity.

The dependence of the accuracy on all listed parameters was studied by the special simulation procedure, described in 4.3.2. The shape of the simulated correlation function was taken gaussian in all three components, the correlation intensity was always set to $\lambda = 0.5$, the rapidity density of charged particles was 8000, the efficiency was assumed to be ideal, the three effective sizes were assumed to be equal ($R = R_{T_{side}} = R_{T_{out}} = R_L$), and two units

of rapidity were used. The influence of the Coulomb repulsion was also estimated by applying the Gamow suppression factor. The simulated correlation functions, for different effective sizes and for samples consisting of different numbers of events, were finally fitted in three-dimensional relative momentum space by gaussian functions.

The results for three effective sizes are shown in Fig. 4.18 as a function of the number of analysed events. Single-event pion interferometry, i.e. one analysed event, should be feasible with a relative error of ≈20% up to effective sizes of 15 fm for the assumed particle density. The results can be approximately rescaled to other experimental conditions (e.g. different dN/dy, acceptance, etc.). Since pions of both charges are available, two independent measurements of the effective interferometric sizes may be done for each event, thus reducing the statistical errors.

An example of a single-event correlation function for R = 15 fm ($R = R_{T_{side}} = R_{T_{out}} = R_L$) is shown in Fig. 4.19.

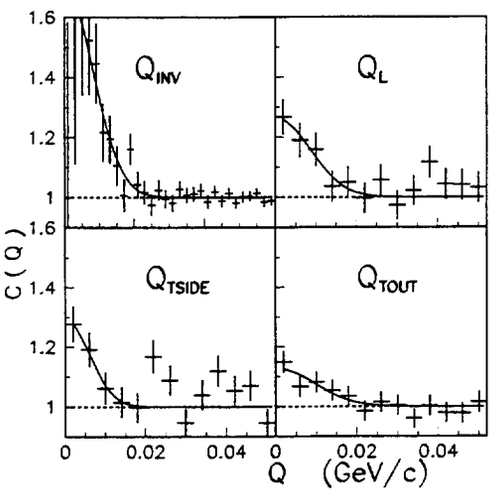

Figure 4.19: Correlation function for a single-event with dN_{ch}/dy = 8000. All three effective sizes were equal to 15 fm ($R = R_{T_{side}} = R_{T_{out}} = R_L$). The upper left quadrant shows the correlation as a function of the invariant momentum difference; the other three quadrants show the projections of the correlation function to the three interferometric momentum components.

4.4 Lepton Pairs

Leptonic final states are of particular interest in heavy-ion collisions, because they can relate information from the early and dense phase of the system owing to their weak final-state interactions. Unfortunately, they are also amongst the most difficult to observe because of combinatorial background from the large number of Dalitz decays in the electron channel or π/K decays in the muon channel. In the following we will discuss the expected performance of our detector in measuring di-electrons.

Dalitz decays (or external conversion pairs) can be recognized and removed owing to their low invariant mass (typically m < 100–300 MeV/c^2) and the low momenta of the individual electrons (three-body decay, average $p_t \approx$ 140 MeV/c). A detector needs to be very efficient in recognizing these low-p_t electrons, because the combinatorial background after the mass cut is essentially proportional to the square of the number of the remaining electrons, and therefore to the *square of the inefficiency* to find the partner of a Dalitz decay [22, 23]. At high multiplicities, a fundamental problem arises even for a perfect detector [23]: The probability for *any* electron to form a random combination of low invariant mass increases towards unity and therefore signal as well as background will be removed by the mass cut; the signal efficiency tends to zero.

Two strategies can be employed to detect-low p_t electrons with high efficiency: a field-free region close to the vertex equipped with electron identification devices [24, 25], where low-mass pairs are rejected by a simple opening angle cut; or a weak field together with good tracking and electron identification extending down to very low momenta (few 10 MeV/c). We have chosen the second strategy, which is in principle superior, because the knowledge of both invariant mass and opening angle allows the same background suppression to be achieved with higher signal efficiency.

4.4.1 Physics Generator

The simulations were performed using SHAKER [3, 26] which includes, besides charged pions, a large number of particles and decays with electrons in the final state. These are the Dalitz decays of π, η, η', ω, and ϕ as background and the leptonic two-body decays of ρ, ω, ϕ and J/Ψ as well as the Drell–Yan continuum as sources.

The particle ratios (with respect to pions) for the lighter mesons up to the ϕ were taken from ISR data. The Drell–Yan and J/Ψ cross-sections were extrapolated from lower energy results; we assumed

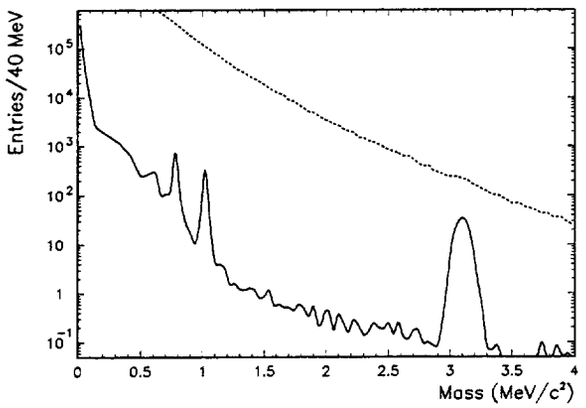

Figure 4.20: Invariant mass distribution for electrons before any cuts. The dashed line shows the mass spectrum of all combinations (i.e. essentially combinatorial background) at a multiplicity of dN_{ch}/dy = 8000, the full line shows the mass spectrum of physical particles (sources) as generated in the Monte Carlo.

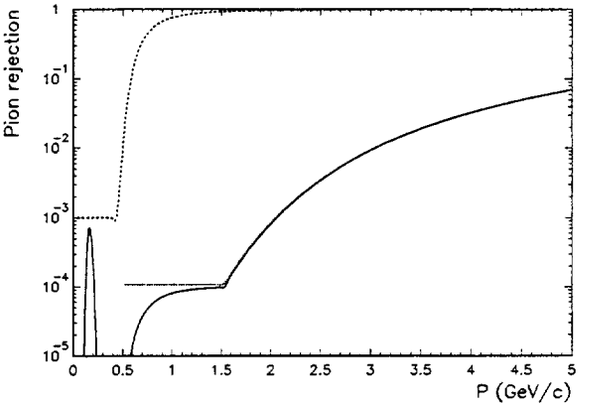

Figure 4.21: Pion rejection of TOF (100 ps, dotted line), dE/dx (7%, dashed line) and combined (full line) for a cut with 93% electron efficiency.

$1.8 \cdot 10^{-3}$ J/Ψ per central Pb-Pb event and unit of rapidity (including branching ratio to e^+e^-) and $5 \cdot 10^{-4}$ Drell–Yan pairs ($m > 1$ GeV/c^2 with $1/m^3$ mass distribution) [22].

External conversions have not been included so far. By requiring a hit in at least one of the first two tracking layers, photon conversions are restricted to the beam pipe (0.5% X_0) and the first tracking layer (0.6% X_0), which, after folding with the energy-dependent conversion cross-section, corresponds to $\approx$ 0.6% conversion probability. More than 80% of these can be recognized by reconstructing the secondary vertex (conversion point) — well separated from the primary one — or by a pulse-height cut in the silicon detectors (double dE/dx for close pairs which do not open up in the weak field). The remaining single electrons should be below the level of the remaining Dalitz decays.

The invariant-mass spectrum in the acceptance before any cuts is shown in Fig. 4.20 for a rapidity density of dN_{ch}/dy = 8000. The signal-to-background ratio will be inversely proportional to the multiplicity density, i.e. a factor of four better for the lowest multiplicity anticipated in central Pb-Pb collisions (dN_{ch}/dy = 2000).

4.4.2 Detector Simulation

The detector response is parametrized in terms of tracking efficiency and pion rejection (see 4.1, 4.2.) The tracking efficiency for electrons is set to 90% for $p_t > 100$ MeV/c, decreases linearly to 30% at $p_t = 20$ MeV/c, and is zero below.

The pion rejection using a TOF system with 100 ps resolution at 3 m distance and the TPC with 7% energy resolution is shown in Fig. 4.21, using a cut with 93% electron efficiency (we have assumed a maximum rejection of 10^{-4} for the TOF and 10^{-3} in the TPC). The pion rejection in the ITS at low p_t has been described in 4.2.

4.4.3 The Low-Mass Region (ω, ϕ)

In order to improve the signal-to-background ratio from the raw distributions shown in Fig. 4.20, we apply a number of successive cuts to the electrons tracked and identified in the detector (see e.g. [23]):

1. *All* electrons forming an unlike-sign pair with any other electron of $m_{ee} < 100$ MeV/c^2 are discarded if (and only if) the opening angle between the electrons is less than 26° ($cos(\theta) > 0.9$). This additional requirement is fulfilled by $\approx$ 94% of the true Dalitz pairs, but only by $\approx$ 30% of the random combinations with m < 100 MeV/c^2.

2. Among the remaining electrons, unlike–pairs are removed from the sample *in order of increasing mass* up to $m = 150$ MeV/c^2.

3. In the next step, we remove *single* electrons which are outside the fiducial area of 90±35° or have a p_t below 450 MeV/c. The fiducial cut reduces the number of Dalitz pairs where one partner is outside the experimental acceptance.

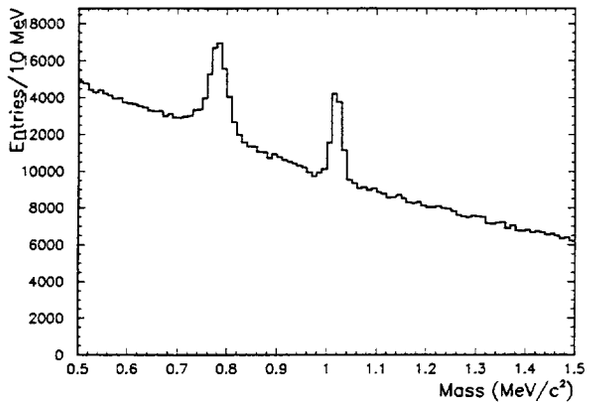

Figure 4.22: Invariant-mass distributions, after cuts, in the ω/ϕ region for $5{\cdot}10^7$ central events, including tracking efficiency and momentum resolution.

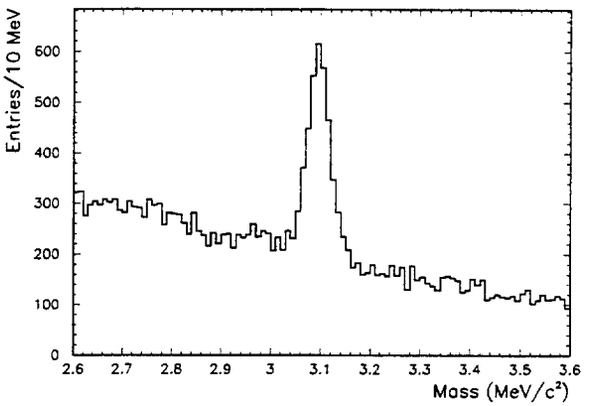

Figure 4.23: Invariant mass distributions, after cuts, in the J/Ψ region for $5{\cdot}10^7$ central events, including tracking efficiency and momentum resolution. The Ψ′ has not been included in our simulation; it will be difficult to observe with the statistic available to us.

4. Finally, we form the invariant mass of all pairs with $p_t^{pair} > 1$ GeV/c.

For the first two steps, we need a high efficiency to find electrons, whereas the pion rejection and track quality criteria can be loose; at this stage the electron-to-pion ratio is of the order of the π^0 Dalitz decay (1.2%). In the later stage, when we consider electrons above 450 MeV/c only, the pion rejection is more important because the e/π ratio at high p_t drops to a few times 10^{-4}.

This analysis program is still under development and the above selection procedure might not yet be optimal.

The invariant-mass spectrum of electrons passing all our cuts is shown in Fig. 4.22 in the mass region of the ω and ϕ mesons for 5×10^7 recorded events. The importance of excellent mass resolution ($\Delta m/m \approx$ 1%) is evident. It contains $\approx$ 20 000 ω mesons (and a similar number of ρ's, which are however not visible because of the large width of the ρ), and $\approx$ 13 000 ϕ's. Only a small fraction of the mesons recorded initially in the detector have survived, owing to our selection criteria and to the fundamental limitations at high multiplicity mentioned above.

4.4.4 The High-Mass Region (J/Ψ)

The selection procedure for high mass lepton pairs proceeds in a similar way. We use different values for the cuts because of the different decay kinematics of high-mass pairs and the better signal-to-background ratio (see Fig. 4.20).

The p_t cut in step 4 is not applied but we restrict the accepted momentum of single leptons to the range $1 < p < 2.5$ GeV/c. The upper momentum limit is needed in order to reduce the amount of misidentified pions (see Fig. 4.21). The resulting mass spectrum in the J/Ψ region is shown in Fig. 4.23. The accepted J/Ψ's are all at $p_t < 2$ GeV/c, where the primary production via gg fusion is favoured over J/Ψ's from bottom mesons, which decay long after freeze-out.

4.5 Prompt Photons

The measurement of prompt photons in a high multiplicity environment is a challenge met by the best available crystal detectors, high statistics, and complex analysis programs. The design of the proposed photon spectrometer is based on the work previously done by NA12 [27], WA80 [28], WA98 [29], and PHENIX [24].

Prompt photons are extracted from the measured inclusive spectrum by subtracting the decay background, which in turn is dominated by π^0 and η mesons decays. Therefore the cross section of these mesons has to be measured with high accuracy. In the following we describe the logical steps which lead to the determination of the measurement error on prompt photons production.

For the event simulation, we use SHAKER to generate particles with the desired multiplicity (dN_{ch}/dy = 8000) and uniformly distributed in rapidity. The η / π^0 ratio is taken to be 0.55 [7] for $p_t \geq 1$ GeV/c, and m_t scaling is assumed.

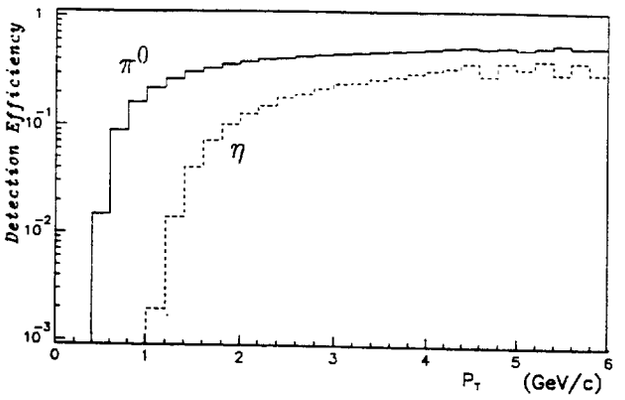

Figure 4.24: Detection efficiency vs. p_t for π^0's and η's in the PHOS calorimeter.

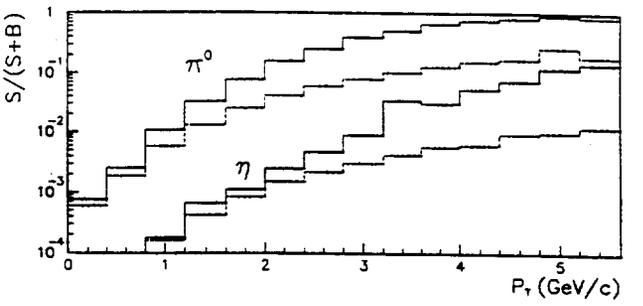

Figure 4.25: $S/(S+B)$ for π^0's and η's.

4.5.1 Photon and Meson Reconstruction

The geometrical acceptance ϵ_{geom} is defined as the fraction of mesons heading towards the detector for which both decay photons have an energy above threshold (see below) and are within the detector. We have chosen the size and shape of the detector such that η mesons are accepted down to $p_t = 1$ GeV/c (a rectangular detector has a lower threshold than a square detector of equal surface).

The γ reconstruction efficiency ϵ_{rec}, i.e. the probability to recognize and accurately measure a photon, depends mainly on the multiplicity. For high statistic measurements, the uncertainty on this efficiency will be the dominating systematic error in the cross section measurement inclusive photons. This systematic error is related to mismatch between generated and true shower profiles, shower fluctuations, cell calibration, and non controlled background (interacting hadrons, bremsstrahlung, etc.).

The electromagnetic calorimeter (PHOS, see 2.6) will detect about 800 γ's and 500 charged particles in a single central collision; i.e. the cell occupancy is <3%. At this occupancy the reconstruction efficiency has been found by simulation using shower profiles to be > 70% for $p_t > 250$ MeV/c. Once real data will be available, it will be calculated by superimposing individual showers of known parameters on complete recorded events. The systematic error on the reconstruction efficiency is difficult to estimate by Monte Carlo, therefore we have used $\Delta\epsilon_{rec}/\epsilon_{rec} \approx 4\%$ [28, 29], relying on existing experience from fixed target heavy-ion experiments, where similar occupancies are reached.

The meson detection efficiency is then given by the geometrical acceptance times the square of the γ reconstruction efficiency. It is shown for π^0's and η's in Figure 4.24.

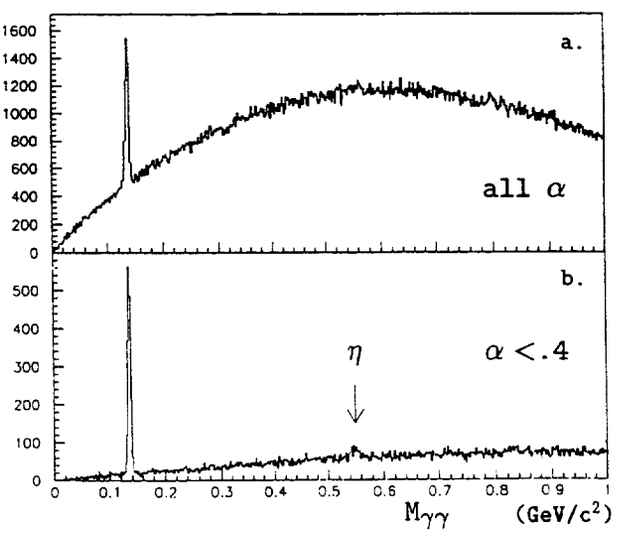

Figure 4.26: $\gamma\gamma$ mass spectra for $5 < p_t < 10$ GeV/c, before and after the $\alpha < 0.4$ cut

4.5.2 Combinatorial Background

The π^0 and η signals will be observed in a $\gamma\gamma$ invariant mass spectrum superimposed on a large combinatorial background. The signal to background ratio can be improved by excluding very asymmetric decays, i.e. by limiting the asymmetry $\alpha = |E_1 - E_2|/(E_1 + E_2)$, and by imposing a threshold condition $E_\gamma > E_{thr}$ (in the simulation studies, we used $E_{thr} = 50$ or 250 MeV, and $\alpha < 0.4$).

The statistical error of the detected π^0 or η signal S depends on the combinatorial background B under the peak, and reads

$$\frac{\sigma_S}{S} = \frac{1}{\sqrt{N_{ev}}} \cdot \frac{\sqrt{S+B}}{S} \qquad (4.2)$$

Here, the background spectrum is smoothed by forming all $\gamma\gamma$ pairs which can be made by mixing γ's from different events. The precision on B is then only limited by the overall normalization error and by systematic effects. The signal to background ratio is directly proportional to the mass resolution σ_M. Using a resolution of $\Delta E/E = 3\%/\sqrt{E} + 3\%/E + 1\%$ (E in GeV) the simulation gives $\sigma_M \simeq 7.5/\sqrt{p_t}$ for the π^0, and $\sigma_M \simeq 30/\sqrt{p_t}$ for η (σ_M in MeV/c^2, p_t in GeV/c). For a given number of events and given experimental resolution, the relative statistical precision on the signal S (π^0 or η production) turns out to be independent of multiplicity.

Figure 4.25 shows $S/(S+B)$ ratios without and with a cut on α, the latter giving a much better signal to background ratio, in particular at high p_t.

A typical high p_t invariant mass spectrum based on 40 000 simulated events is shown in Fig. 4.26, where the effect of the α cut on the background and on the observability of the η meson is clearly visible.

We have used real data from a recent and comparable experiment to estimate the accuracy that can be achieved in meson reconstruction. Figure 4.27a shows the $\gamma\gamma$ invariant mass spectrum in WA80 data from ^{32}S on ^{197}Au reactions at the SPS. Figure 4.27b shows the same data after subtraction of the smoothed combinatorial background. The number of π^0's (η's) has been extracted with a relative precision of 3% (25%) at $S/B = 2 \cdot 10^{-2}$ ($S/B = 2 \cdot 10^{-3}$). The precision of these results is still limited by statistical rather than systematic errors [30]. Therefore, we expect that with sufficient statistics the cross section for π^0's (η's) can be measured with 1% (10%) error at $S/B = 10^{-2}$ (10^{-3}).

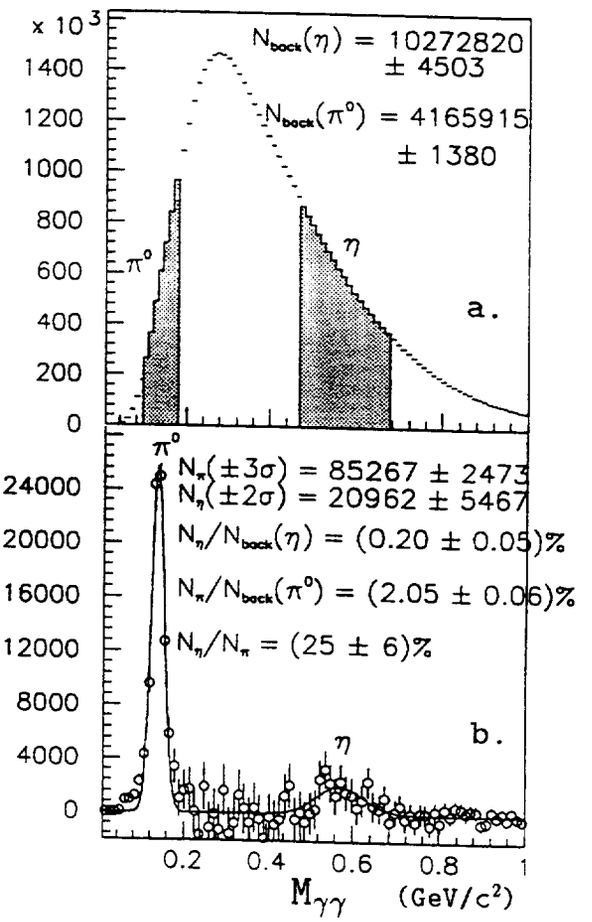

Figure 4.27: WA80 $\gamma\gamma$ mass spectrum a) before and b) after background subtraction

4.5.3 Results

Once the π^0 and η production cross sections are measured, their decay γ spectra can be subtracted

from the observed inclusive γ spectrum to extract the prompt photons. Because of the steeply falling spectra, prompt photon production at a given p_t and its error are dominated by meson production near the same p_t. The error in the γ/π^0 ratio results from the quadratic sum of the relative error of the π^0 signal, the error in the measured η/π^0 ratio, and the relative error in the γ reconstruction efficiency ϵ_{rec}. For 10^7 events, we find that the error on the π^0 cross section will be $< 1\%$ up to 5 GeV/c, while the error on the η/π^0 ratio will not exceed 2%, except near 1 GeV/c where it reaches 5%. At larger p_t, both errors increase and reach 5% at 10 GeV/c. Taking into account the error of 4% in the γ reconstruction efficiency, (and enlarging the bin size at large p_t), the overall r.m.s. error on γ/π^0 will be of the order of 5-7% between 1 and 10 GeV/c.

4.6 Global Event Characterisctics

Events can be characterized globally by:

- Collision geometry, i.e. impact parameter or number of participating nucleons, measured in the Zero-Degree Calorimeter.
- The number of produced neutral and charged particles and their rapidity density, measured by the ITS, the multiplicity detectors and possibly NEC and FEC.
- The emission pattern of particles as a function of rapidity e.g. global shape, sphericity, multiparticle-clustering or azimuthal anisotropy.
- The ratio of photons to charged particles, measured by the TPC and PHOS.
- The transverse energy per particle (TPC, PHOS, and possibly NEC and FEC). In the case of the photons, an event characterization and selection can be done on-line in the trigger.

In the following we will show some examples for the first two points mentioned above.

4.6.1 Zero-Degree Energy

The initial condition of the nuclear collision is controlled by the collision geometry, i.e. the number of participants. The Zero Degree Calorimeters (ZDC) will detect neutrons and protons at very large pseudorapidity (see 2.7.2). Spectator clusters with $Z/A \geq 0.5$ can be detected only if a Roman-Pot structure were employed. However, for central collisions at LHC energies the beam nuclei are expected to disintegrate fully into protons and neutrons. In this case

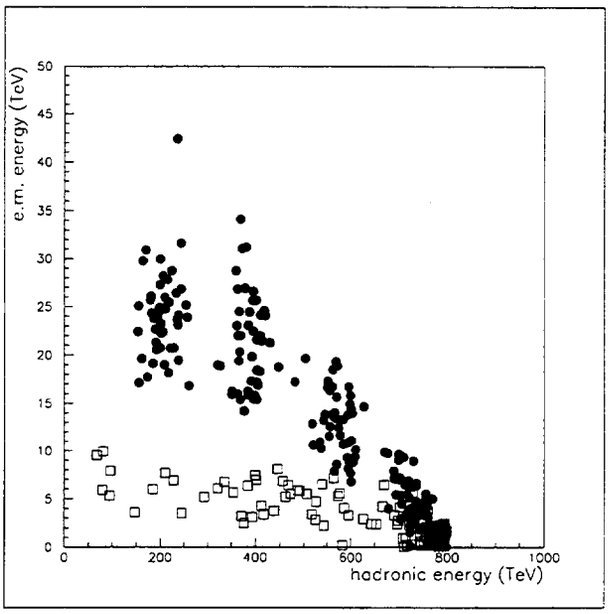

Figure 4.28: Zero-Degree electromagnetic vs. hadronic energy (only neutrons) as predicted by HIJING (solid circles) and VENUS (open squares)

the simulations, whatever generator is used, predict a correlation between the energy measured by the ZDC calorimeters and the number of spectators. Therefore the measurement of the energy released in the ZDC allows the total number of spectators (and of participants) to be determined. To achieve a better accuracy, this measurement will be done on both sides of the interaction point. The main background is represented by the reaction products which enter into the calorimeters; the event-by-event fluctuations of the energy carried by these particles account for the width of the correlation. This fluctuation is of the same order as the resolution of the calorimeters (see 2.7.2), which is therefore adequate for the measurement.

Further information on the degree of stopping will be provided by the e.m. section of the neutron calorimeter, which will detect the energy sum of photons from forward-decaying π^0's and from forward-bremsstrahlung photons [31]. Figure 4.28 shows decay photons from π^0 on a sample of events generated with the VENUS and HIJING [2] codes plotted as a function of the energy entering the neutron calorimeters (i.e. as a function of the centrality of the collision).

4.6.2 Rapidity Distributions

Once the reaction geometry has been determined, the entropy production per participant is related to the

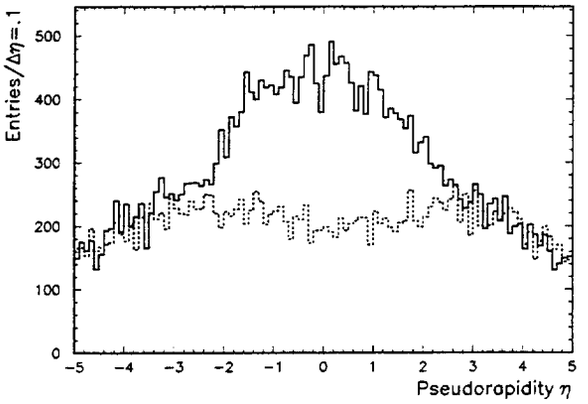

Figure 4.29: Rapidity distribution of charged particles for two central HIJING Pb-Pb collisions. The dashed line is without and the full line with the effect of 'jet quenching'.

particle multiplicity. This is measured by the silicon vertex detector and by the charged-particle multiplicity array at large rapidities up to $\eta = 5$. The predictions of the total number of produced particles at midrapidity differ by a factor of up to four, ranging from 2000 to 8000 charged particles in a central Pb-Pb collision. The rapidity distribution of particles reflects the dynamics in the nuclear collision. Flat rapidity distributions as forecast in the Bjorken picture are in disagreement with the hydrodynamical scenarios and the Landau model.

As an example of the performance of the multiplicity counters array we show in Fig. 4.29 the $dN_{ch}/d\eta$ distribution of two single events.

The histogram binning ($\Delta\eta = 0.1$) is identical to the granularity of the multiplicity array for $\eta > 1$, and we have assumed a resolution proportional to $1/\sqrt{N}$ in addition to the Poisson fluctuations of the true multiplicity. The events were generated with the HIJING event generator, the first one (full line) with 'standard' parameters, the second one switching off the parton energy loss. The striking difference in the central plateau height as well as the width is due to the 'jet-quenching' (see 1.1.2), by which the energy of a hard parton is redistributed to a large number of soft particles via collisions in the dense system.

References

[1] Large Hadron Collider Workshop, Aachen, 1990, ECFA 90–133, CERN 90–10.

[2] N.X. Wang et al. , Phys. Rev D 44 (1991) 3521 and Phys. Rev. Lett 68 (1992) 1480.

[3] F. Antinori, Internal Note ALICE/MC 93–9.

[4] F. Abe et al., ANL–HEP–PR 88–32 (1988).

[5] T. Alexopoulos et al., Phys. Rev. Lett. 64 (1990) 991.

[6] M. Bourquin and J. M. Gaillard, Nucl. Phys. B114 (1976) 334.

[7] V. Hedberg, LUNFD6 (NFFL–7073), 1987.

[8] R. Brun et al., GEANT 3, CERN DD/EE/84–1 (1986).

[9] N. van Eijndhoven, Internal Note ALICE/MC 93–5 and 93–6.

[10] M. Regler, R. Frühwirth, Proc. Advanced Study Institute on Techniques and Concepts in High Energy Phys., St. Croix, 1988.

[11] Design Study of the Large Hadron Collider, CERN 91–03 (1991).

[12] P.V.C. Hough, U. S. Patent 3069654, 1962;
R.O. Duda, P. E. Hart, Commun. ACM, 15(1) (1972) 11;
D.H. Ballard, Pattern Recognition 13(2) (1981) 111.

[13] B. Denby, Comput. Phys. Commun. 49 (1988) 429;
C. Peterson, Nucl. Instrum. Methods A 279 (1989) 537;
M. Gyulassy, M. Harlander, Comput. Phys. Commun. 66 (1991) 31.

[14] W.T. Eadie et al., Statistical Methods in Experimental Physics, North-Holland (1971, 1977, 1982).

[15] J.F. Bak et al., Nucl. Phys. B288 (1987) 681.

[16] R.M. Sternheimer et al., Phys. Rev. D26 (1982) 6067.

[17] S. Hancock et al., Phys. Rev. A28 (1983) 615.

[18] T. Akesson et al., Nucl. Phys. B333 (1990) 48.

[19] STAR Conceptual Design Report, LBL-PUB-5347, 1992.

[20] W.B. Atwood et al., Nucl. Instr. Meth. A 306 (1991) 446.

[21] D. Ferenc, Internal Note ALICE/MC 93–14.

[22] H.J, Specht, Large Hadron Collider Workshop, Aachen, FRG, 1990, CERN 90–10, Vol. III, p. 1236.

[23] P. Glassel, RHIC workshop, Brookhaven 1985, BNL 51921, p. 149.

[24] PHENIX experiment at RHIC, BNL, preliminary Conceptual Design Report (1992) unpublished.

[25] NA45 experiment at CERN-SPS, SPSC-88–25/P237, SPSC-88–40/P237 Add. 1.

[26] J. Bohm, Internal Note ALICE/MC 93–11.

[27] F. Binon et al., Nucl. Instr. Meth. A248 (1986) 86. See also D. Alde et al., "Data Reduction Procedures for Large Multicellular Electromagnetic Calorimeters", CERN-EP 87-28, unpublished.

[28] R. Albrecht et al., Z. Phys. C51 (1991) 1.

[29] WA98 Proposal, CERN/SPSLC 91–17, May 1991.

[30] S. Fokin et al., Internal Note ALICE/CAL 92-16.

[31] J.D. Bjorken and L. McLerran Phys. Rev. D31 (1985) 63 and A. Dumitru, University of Frankfurt, Frankfurt, Germany, private communication.

5 Implementation

5.1 Experimental Area

The proposed detector concept, based on the use of the L3 magnet and experimental area, permits the full physics programme outlined above and allows options and extensions which are currently under study. The large magnet and the large dimensions (diameter *and* length) of the cave are of great importance.

Work in the Control Room: The present control room needs to be modified to comply with radiation safety requirements at the LHC.

Work in the Tunnel: For the Zero-Degree Calorimeters (ZDCs), sections of the vacuum beam pipe with a larger inner radius need to be installed between D1 and D2. The ZDC probably needs some repositioning during high-intensity proton running in order to avoid radiation damage.

Work foreseen in the L3 cave: No major changes of the existing hall are foreseen, specifically no lifting of the magnet into the position of the LHC beam. The present infrastructure is sufficient for the installation of the ALICE detector because of its limited weight. Since no major changes are foreseen to the magnet nor to the cave, a rapid change-over from LEP operation into LHC operation should be possible.

In case the L3 cave and magnet were not available: The construction of a new magnet and its installation into another LEP cave would prolong the time needed for the ALICE setting-up. Any extension to study the larger rapidities would yield prohibitively large digging costs for enlarging the tunnel.

5.2 Radiation Environment

The radiation level in the experiment has been estimated using the FLUKA code [1]. Low-energy neutrons down to 100 keV were taken into account in the simulation.

The estimates were based on the assumption of a one-month running period per year with a luminosity of $10^{27}\ cm^{-2}s^{-1}$. These numbers have been multiplied by two to obtain the yearly dose, including the low-luminosity proton running.

The annual dose at $R = 30$ cm, i.e. in the region of the ITS is on the level of 10 Gy/year. The annual neutron fluence is $\sim 10^9$ cm^{-2}, about three orders of magnitude smaller than those foreseen for pp experiments.

QED Electrons

One potential area of concern for detectors close to the interaction vertex is low-mass lepton pairs created by the electromagnetic interaction of the colliding heavy-ion beams. Pair creation followed by electron capture is indeed one of the limiting factors for the luminosity at LHC [3].

We have calculated the expected flux of electrons [4, 5]. The total rate in the area of the silicon drift chambers is below one per 6 μs (the integration time of this device) and is negligible where the TPC is located. While the production rates for these pairs are large, their p_t is small and they are mainly produced in the forward direction.

5.3 Cost Estimates

The cost of the apparatus has been estimated taking into account (whenever appropriate) the different options which have been illustrated in the previous sections. The costs are summarized in Table 5.1.

The cheapest configuration for the Inner Tracking System (see 2.2) has Si-drift detectors for the three innermost layers and microstrip gas chambers for the two outermost layers. Conversely, the most expensive configuration is obtained with pixel detectors for the first layer, followed by three Si-drift layers and Si-microstrips for the outermost layer. The finals choices for the ITS will be based on track finding performance, which is still under study, and cost evaluation. The costs are given per module (see Table 2.2). The cost of the ITS will be in the range 10 500 to 25 500 kCHF.

The range shown in Table 5.1 for the particle identification system simply reflects the minimum and maximun cost estimate obtained for the different system considered in 2.4.

Concerning the large rapidity detectors the uncertainty is due only to the choice of the showering material adopted for the ZDC (see 2.7.2).

Finally, we have estimated the cost of the infrastructure based on LEP experience, assuming that half of the existing equipment can be re-used.

Under these conditions the total cost varies between **79.6** and **105.6** MCHF. We have not included any cost for reusing the (unchanged) L3 magnet, which has to be discussed with the L3 collaboration at the appropriate time. Should the L3 magnet not be available one would have to include a cost of $\approx$10 MCHF if we were to build a large solenoid (see 2.1.2).

Subsystem	Unit cost (CHF)	Partial cost (kCHF)	**TOTAL** (kCHF)
Inner Tracking System:			**10500 – 25500**
PIXEL	3300 / *module*		
Si-DRIFT	9000 / *module*		
Electronics	7000 / *module*		
Si-STRIP	4250 / *module*		
Electronics	1000 / *module*		
MSGC	700 / *module*		
Electronics	1300 / *module*		
Mechanics and Cooling		2500	
TPC:			**14900**
Detector		3900	
Mechanics and Cooling		600	
R/O electronics	20 / *channel*	10400	
Particle Identification:			**4400 – 12800**
TOF by Pestov Counters		**4400**	
Detector		700	
Electronics	10 / *channel*	1700	
Mechanics etc.	500 / *module*	2000	
TOF by Parallel Plate Chambers		**6200**	
Detector	15 / *cell*	1800	
Electroncis	10 / *channel*	1200	
Mechanics etc.		3200	
TOF by Scintillator Grid		**12800**	
Detector	1.23 / cm^3	1400	
Photomultipliers		10000	
Electronics	10 / *channel*	1400	
RICH		**11500**	
Radiator	45000/*module*	4500	
MWPC	10000/*module*	1000	
Electronics	60000/*module*	6000	
PHOS:			**24000**
Detector	320 / *cell*	16000	
Electronics	120 / *cell*	6000	
Mechanics		2000	
Large Rapidity Detectors:			**2300 – 2900**
MCP:		**400**	
Detector		300	
Electronics		100	
ZDC:		**1900 – 2500**	
Detector		1000 – 1600	
Electronics and PM		600	
Mechanics		300	
DAQ and COMPUTING:			**18500**
Central DAQ		3600	
Front-end crates		9900	
Off-line computing		5000	
INFRASTRUCTURE			**5000 to 7000**

Table 5.1:

5.4 Organization and Responsibilities

During the preparation of the present LoI, the ALICE Collaboration has adopted the following organization:

Spokesman: J. Schukraft, CERN.
Deputy: H. Gutbrod, Darmstadt GSI.

Executive Committee: F. Navach, Bari;
I. Otterlund, Lund;
E. Quercigh, CERN;
L. Riccati, Turin;
K. Šafařik, Collège de France;
H.J. Specht, Darmstadt GSI;
R. Stock, Frankfurt.

The management is then completed by the Institute Board (one representative from each Institute) and by the full Collaboration Board.

The work needed to complete this LoI has been carried out by the following Working Groups, each supervised by one or two Project Coordinators:

Magnet :	A. Vodopianov
Inner Tracking System :	P. Giubellino and F. Meddi
TPC :	R. Brockmann
TOF System :	R. Schmidt
RICH :	G. Paić
E.M. Calorimeters :	H.-A. Gustafsson and P. Sonderegger
ZDC :	M. Gallio
DAQ :	H. Beker and B. Kolb
Tracking Software :	K. Šafařik
HBT :	D. Ferenc
Simulation :	N. van Eijndhoven
Editing :	F. Navach

Table 5.2 gives a summary of the areas of interest of different collaborating Institutes.

Area of interest	Institutions
Inner Tracking System	Bari DEEP, Bari DFU, Birmingham, Heildelberg MPI, Rome, St Petersburg, Utrecht, Turin, Warsaw
TPC	Cracow, Darmstadt GSI, Frankfurt, Utrecht
TOF	Athens, Catania, Darmstadt GSI, Dubna, Marburg, Moscow ITEP, Novosibirsk
RICH	Bari DFU, CERN, Zagreb
Calorimeter	Calcutta, Dubna, Lund, Minsk, Moscow Kurchatov, Münster, Protvino
ZDC + MCP	Moscow INR, Řež, St Petersburg, Turin
Trigger and DAQ	Darmstadt, Rome
Off-line computing	Cracow INP, CERN, Frankfurt, Košice, Moscow ITEP, Paris, Prague, Utrecht

Table 5.2:

5.5 Staging

In case that staging becomes necessary, our strategy would be to reduce the acceptance coverage of the experiment rather than to leave out completely any of the baseline subdetectors. In this way we aim to retain our physics programme, albeit with reduced performance.

The support structure should be fully installed at the initial date in order to allow for a smooth completion of all subdetectors within the first two years of operation.

A staging scenario in which the central subdetectors are only partially equipped at the initial date could be the following:

- ITS: Acceptance coverage reduced to $(90 \pm 30)^\circ$ for the two outer tracking layers (reduction of other layers would result only in minor cost savings);
- TPC: Unchanged (staging is impossible);
- TOF/RICH: Acceptance coverage reduced to $(90 \pm 30)^\circ$;
- PHOS: Area reduced to 5 m^2.

The total cost of such a staged detector would be in the range 58 to 75 MCHF, depending on the options as explained in sec. 5.3.

As an example of the reduction in performance implied by such a scenario, we calculated that the acceptance for J/Ψ decays would decrease by a factor of 3–4 (depending on cuts), and the acceptance for Ξ^- decays by a factor of 3. The reduction in size of

the PHOS would exclude the measurement of π^0 and η decays in the relevant p_t region, thus increasing the systematic error for prompt photons from $\approx$ 5% to $\approx$ 15–20%.

References

[1] A. Fassò, A. Ferrari, J. Ranft, P.R. Sala, G.R. Stevenson and J.M. Zazula, 'FLUKA92', presented at the Workshop on Simulating Accelerator Radiation Environments, 11–15 January, 1993, Santa Fe, U.S.A.

[2] J. Schukraft, Proc. Gen. Meeting on LHC Physics & Detectors, Evian, France, March 1992, p. 479.

[3] Design Study of the LHC, CERN 91–03 (1991).

[4] A. Kholozvari, Internal Note ALICE 93–1.

[5] N. Baron and G. Baur, Phys. Rev. D46 (1992) 3693.